AN ABSTRACT OF THE THESIS OF

Sara E. Church for the degree of Doctor of Philosophy in Chemistry presented on April 23, 1987.

Title: Structural Effects of Intrinsic and Extrinsic Perturbations to Model Membranes

Abstract approved: Redacted for Privacy

The observed and calculated structural parameters of three systems of phosphatidylcholine bilayers in fully-hydrated multilamellar vesicles (MLVs) were determined using x-ray diffraction techniques. The analysis used the x-ray reflections from the low-, intermediate- and wide-angle regions of the diffraction patterns in the subgel, gel, rippled and fluid phases to determine the lamellar repeat distance, projected electron density profile, headgroup and sidechain area, sidechain tilt angle, width of the lipid bilayer, and hydration level based on the known molecular volume of the lipids in each phase.

The thermotropic phases of DPPC were reinvestigated to establish a model system and to determine the changes in packing modes through the transitions. Based on changes in the headgroup area and hydration level as the temperature is raised through the subgel phase and on the large discrepancy between the calculated lipid thickness and the peak-to-peak distance in the electron density profile, the reflections in the intermediate region of the diffraction pattern were reassigned to obtain a larger headgroup area. The headgroup area and hydration level were found to be larger in the subgel than in the gel phase, contrary to previous analyses. The subgel- and gel-phase sidechain packing modes coexist through the subgel to gel phase transition. No coexistence was observed in the transformation from the gel phase to the subgel phase on annealing at low temperatures. Reflections in the intermediate region of the diffraction patterns from the gel and fluid phases were identified and interpreted as reflections from headgroup packing.

To investigate the effects of intrinsic perturbations to the model system, the structural parameters of bilayers of two isobranched lipids

(17iPC and 20iPC) were determined. No rippled phase is observed in either lipid. Although the subgel, gel and fluid phases are analogous to those observed in DPPC, the presence of the single methyl group at the penultimate carbon of each side chain affects both the headgroup and sidechain packing and reduces the hydration levels in all phases.

To investigate the effects of extrinsic perturbations to the model system, the structural parameters of bilayers of DPPC in the presence of 10, 20 and 30mol% concentrations of bromoform were determined. The main effect of the presence of the solute is to stabilize the rippled phase, extending its range to lower temperatures. The changes induced in the structural parameters are non-monotonic as a function of solute concentration, but hydration levels are generally reduced. Up to 30mol%, the partial molar volume of bromoform in the bilayers is negligible.

©Copyright by Sara E. Church
April 23, 1987

All Rights Reserved

STRUCTURAL EFFECTS OF

INTRINSIC AND EXTRINSIC PERTURBATIONS

TO MODEL MEMBRANES

by

Sara E. Church

A THESIS

submitted to

Oregon State University

in partial fulfillment of

the requirements for the

degree of

Doctor of Philosophy

Completed April 23, 1987

Commencement June 1987

APPROVED:

Redacted for Privacy

Professor of Chemistry in Charge of Major

Redacted for Privacy

Head of Department of Chemistry

Redacted for Privacy

Dean of Graduate School

Date thesis is presented April 23, 1987

Prepared and presented by Sara E. Church

DEDICATION

to my husband

ACKNOWLEDGEMENTS

I wish to thank:

Hollis Wickman for doing everything an advisor does and much, much more

Dave Griffiths for acting as a second advisor and a friend and collaborator too

Ted LaPage for creating FILOP and all the other convenient little programs that made analysis possible

Cecilia and Margie and Socorro and Sarah and Tim and Cori for being here

Mom and Dad and Terry and Aaron and Tim and Deb and Ellie and Libby and Tom and Gina and Marsh and Ian and Becky and Farsh and Bijan and Todd and Laura and Pat and Pam and Dennis for being there

Nika and Tosca for being here and there

TABLE OF CONTENTS

LIST OF FIGURES

LIST OF FIGURES, continued

LIST OF TABLES

STRUCTURAL EFFECTS OF INTRINSIC AND EXTRINSIC PERTURBATIONS TO MODEL MEMBRANES

INTRODUCTION

By definition, an amphiphile is a molecule with both a hydrophilic (polar headgroup) and a hydrophobic (nonpolar hydrocarbon tail) portion (Figure 1). This duality of solubility gives amphiphilic molecules certain self-assembling properties in the presence of solvent. In an aqueous environment, the hydrophobic portions of the molecule will orient away from the amphiphile-water interface, creating a hydrocarbon core surrounded by a polar shell. The type of assembly formed is dictated by the shape of the molecule [1], as shown in Figure 1.

The critical biological significance of the spontaneous formation of these molecular assemblies is evident when the bilayer structure shown in Figure 1d is compared with the structure of a biological membrane, shown in Figure 2 (Singer-Nicholson fluid-mosaic model). In fact, the inherent bilayer structure of a biological membrane derives from the amphiphilic nature of its lipid, or water-insoluble, constituents. The lipid bilayer not only provides a support matrix for the membrane proteins, but also plays an active role in membrane function.

A native biological membrane is a complex assembly comprising a mixture of lipids which are heterogeneous with respect to structure, polarity, headgroup and sidechain constitution and degree of saturation. The membrane performs a broad range of functions essential to cell viability; the performance of these functions and the structure and composition of the membrane are highly interdependent. The importance of this interrelationship is underscored by the emergence of membrane science as a subfield of biological sciences [1-15].

To understand the functioning of complex biological membranes, much study has been devoted to simpler, related systems. Ideally, the simplest model membrane will comprise only two components: a pure lipid with a known structure and pure water. Such an ideal system has not always been attainable, however. For the early studies, the lipid

MOLECULAR ASSEMBLIES of AMPHIPHILES

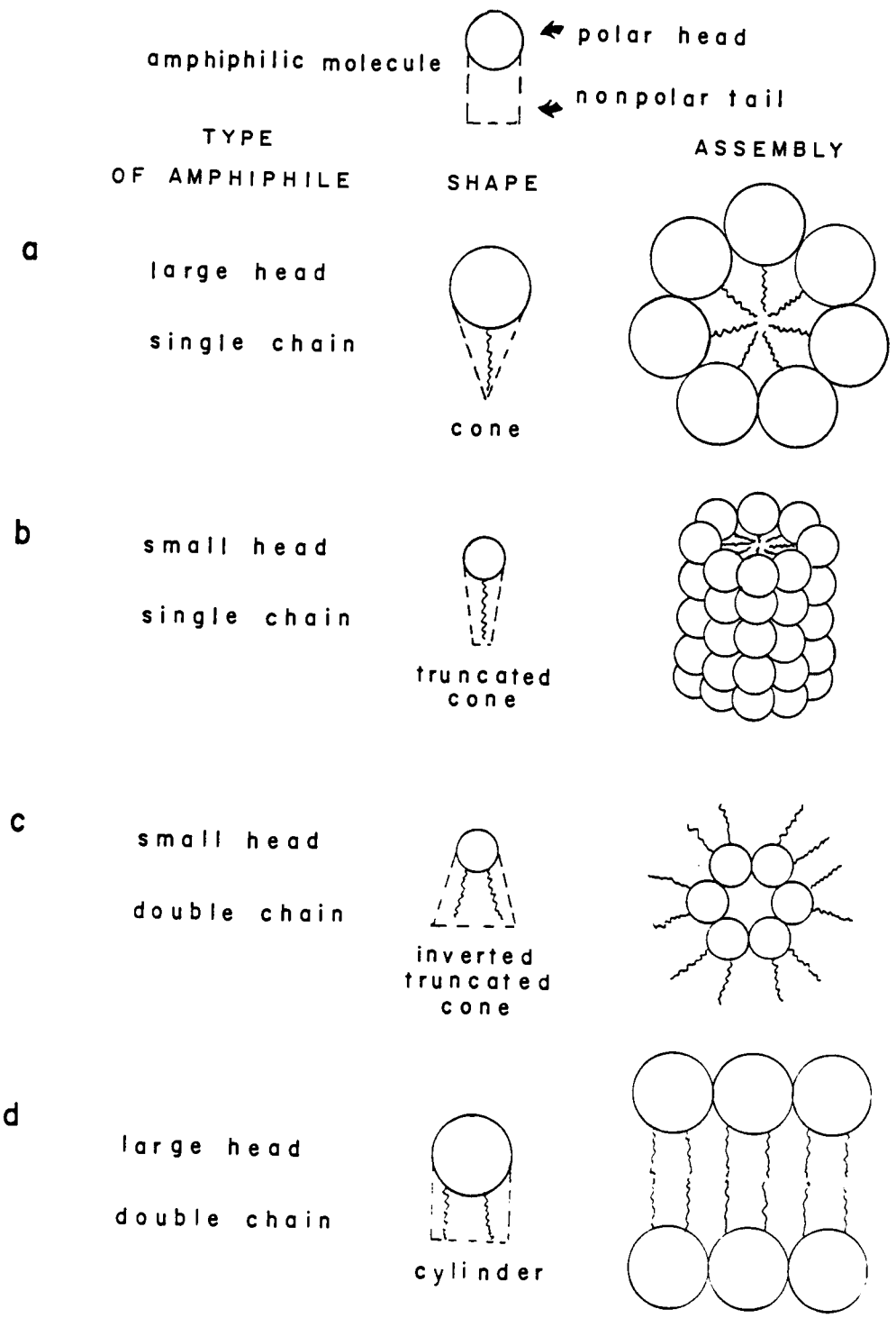

Figure 1: Amphiphilic molecules and molecular assemblies formed in aqueous solution: a) spherical micelles, b) cylindrical micelles, c) inverted micelles and d) bilayers

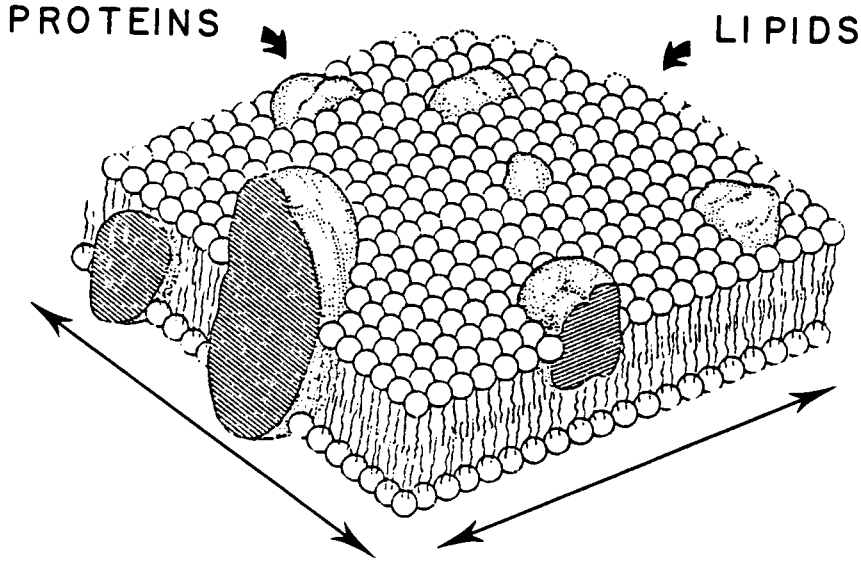

Figure 2: Singer-Nicholson fluid-mosaic model of a biological membrane. The membrane proteins are embedded in a bilayer support matrix of amphiphilic lipids.

components of the model membranes were obtained by extraction from biological membranes. This procedure yielded a mixture of lipids with a variety of headgroup structures. In addition to the technical difficulties in separation of a pure lipid species from the mixture, model studies were complicated by the inherent heterogeneity of sidechain structure within a species.

Over the last two decades, procedures have been developed and refined to synthesize high-purity lipids with known structures [16-29]. With these synthetic lipids, the model membrane composition is known precisely and can be controlled so that quantitave analysis of the effects of structural or compositional modifications can be made. Once the characteristics of such a model system are known, the effects of the presence of additional components, which may be of physiological, environmental or pharmacological interest, can be assessed.

The lipids most commonly used in model studies are the phospholipids, since they constitute the major lipid fraction of most membranes. Of particular interest are the phosphatidylcholines, in which a phosphatidylcholine head group and two fatty acids are attached by ester linkages to a glycerol backbone. Figure 3 shows the structures of the three synthetic phosphatidylcholines used for the studies in this thesis. These include DPPC, the most widely used phospholipid in studies of model membranes, and two isobranched analogs, 17iPC and 20iPC, in which one hydrogen on the penultimate carbon of each chain is substituted with a methyl group.

Membrane phases

Studies of pure-component model membranes indicate that the phase of the membrane, which is described by such parameters as bilayer width, hydration state and molecular conformation, is affected by its composition. The phase of the bilayer, particularly the state of the side chains, has a direct effect on membrane properties, such as permeability, compressibility and ability to partition solutes [2,9-11,14,30-31].

Membrane lipids exhibit the thermotropic and lyotropic characteristics of liquid crystals [32-33]. Therefore, the type of two-dimensional order observed in a bilayer is sensitive both to

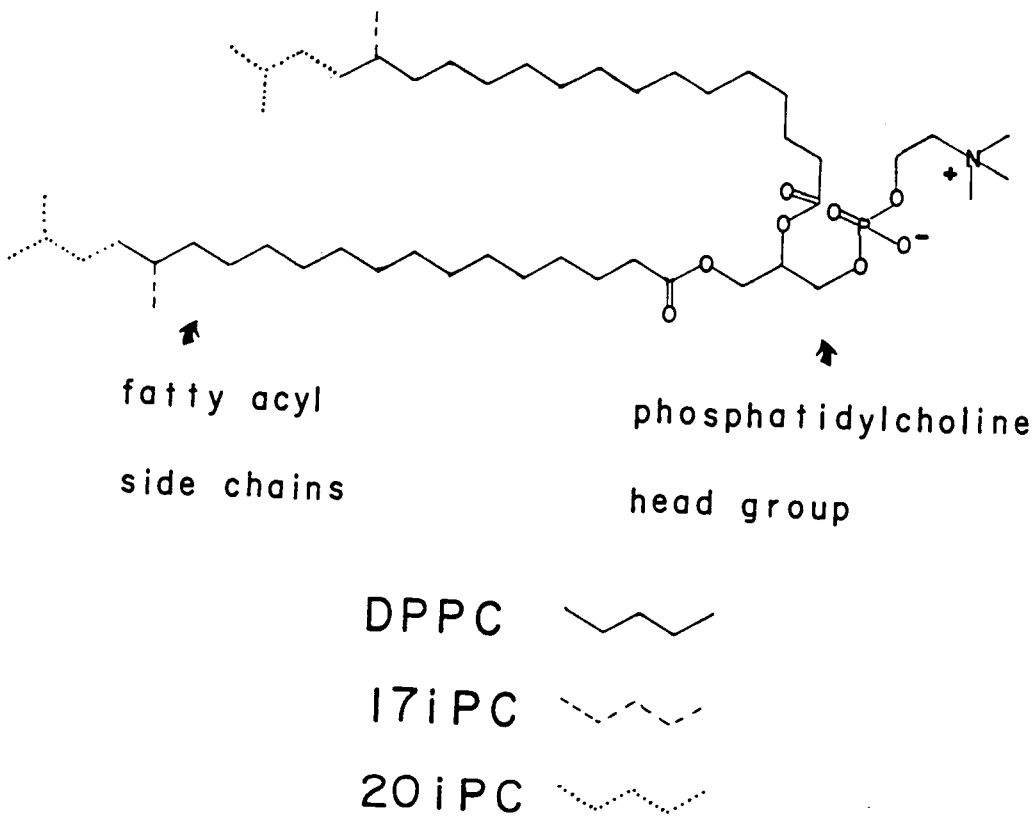

Figure 3: Three synthetic phosphatidylcholines

DPPC: 1,2-dihexadecanoyl-sn-glycero-3-phosphorylcholine (dipalmitoylphosphatidylcholine, dipalmitoyllecithin)
17iPC: 1,2-di(15-methyl)-hexadecanoyl-sn-glycero-3-phosphorylcholine
20iPC: 1,2-di(18-methyl)-nonadecanoyl-sn-glycero-3-phosphorylcholine

temperature and hydration level [8,33-35]. A wide variety of techniques have been employed to characterize model membranes. Surface pressure/area studies, voltammetry, differential scanning calorimetry (DSC), fluorescence and light scattering, dilatometry, x-ray diffraction, nuclear magnetic resonance (NMR), electron microscopy, electron paramagnetic resonance (EPR), infrared (IR) and Raman spectroscopy have all been applied to provide different types of information about the model systems. Of these techniques, x-ray diffraction provides the most comprehensive structural information, with other techniques providing complementary information.

Fully-hydrated bilayers of phosphatidylcholines with two identical, saturated, unbranched side chains (such as DPPC) exhibit four distinct phases, shown in Figure 4. The phases are classified according to molecular order and sidechain state. A capital Roman letter denotes the arrangement of the molecules in the bilayer and subscripts indicate the state of the side chains, with a prime (′) signifying that the chains are tilted with respect to the bilayer plane. The meanings of the symbols used are as follows:

L planar bilayer	smooth interface
P rippled bilayer	corrugated interface
$\alpha(\alpha')$ disordered or liquid crystalline	many kinks, gauche conformations rotational freedom of chains no correlation between orientation of adjacent side chains
$\beta(\beta')$ ordered or gel	nearly all trans conformations low correlation between orientations of adjacent side chains
c(c′) highly ordered crystal or subgel	all trans conformations high correlation between orientations of adjacent side chains

Figure 4 also shows the sequence of phases as the temperature is raised. The low-temperature subgel, or $L_c(_{c'})$, phase is metastable and only attained after prolonged annealing of the bilayers at low temperatures.

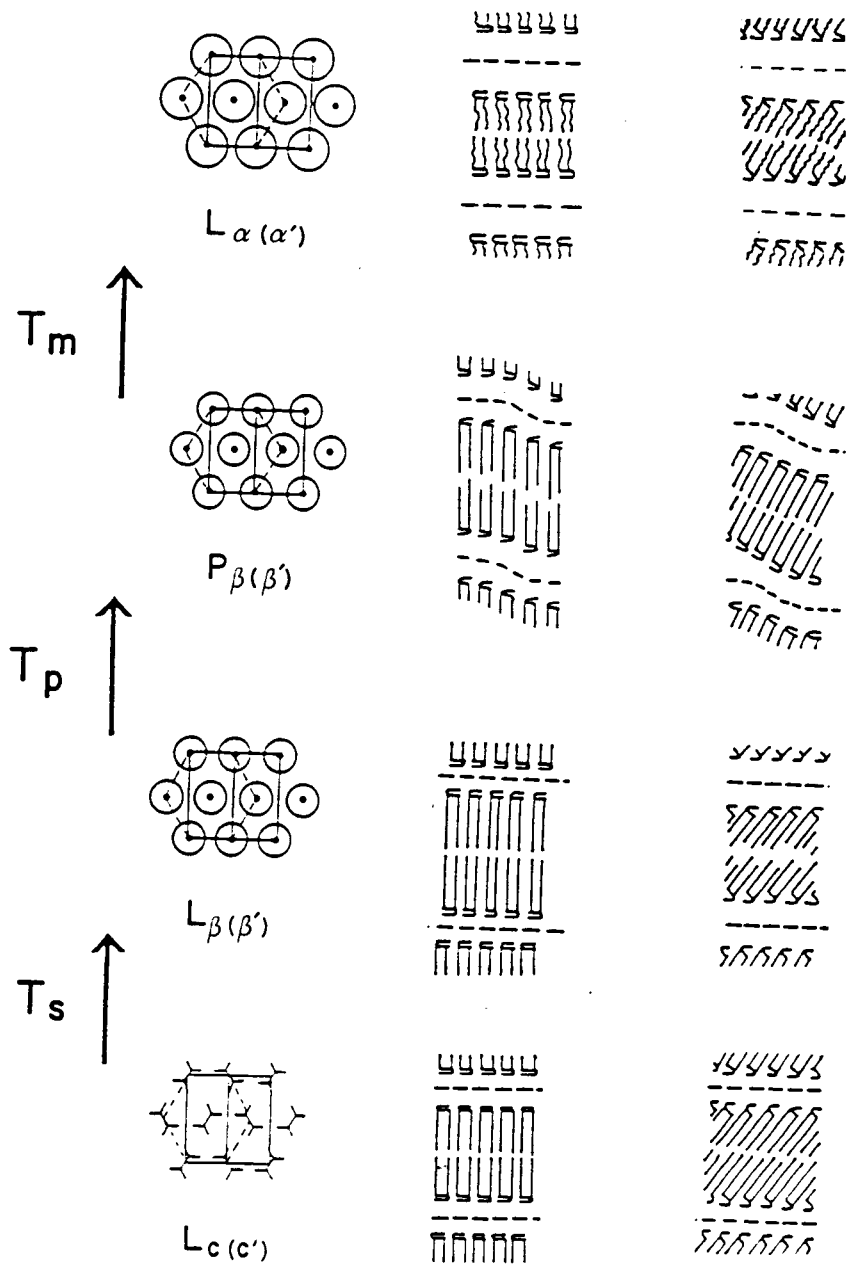

Figure 4: The smectic phases of phosphatidylcholines
a) subgel $L_{c(c')}$, b) gel $L_{\beta(\beta')}$, c) rippled $P_{\beta(\beta')}$, and d) liquid crystalline L_{α} phases

Motivation for thesis research

Although it has long been appreciated that the phase of a membrane is affected by membrane composition and constituent structure, the underlying physical reasons for the effects are incompletely understood [35-45] and many fundamental questions remain unanswered:

How does water diffuse through the bilayer [46]?

Is the rippled phase in phosphatidylcholines sinusoidal or saw-tooth? [34,47-48]?

Are the side chains tilted or untilted in the rippled phase [49-50]?

What is the conformation of the headgroup in each phase [1,8,51]?

How do hydration level, headgroup conformation and side chain packing interact to stabilize each phase [1,52-54]?

How do the structures of the two low-temperature phases in phosphatidylcholines differ [55]?

The purpose of this thesis is to address such questions as these. Explicity, the goals were:

1) to modify an existing x-ray diffraction apparatus to improve the efficiency of data collection and to enable simultaneous collection of low-, intermediate- and wide-angle powder patterns;

2) to develop an analysis scheme to obtain comprehensive structural parameters based on the data from the x-ray diffraction patterns of lipid bilayers in multilamellar dispersions (MLVs);

3) to reexamine the structural parameters of the phases of fully hydrated bilayers of DPPC in multilamellar vesicles (the model system) by applying the analysis scheme and to address or resolve current ambiguities in interpretation of the structures;

4) to apply a similar analysis two systems of multilamellar vesicles of pure isobranched lipids;

5) to characterize structurally the model system in the presence of several concentrations of bromoform.

The thesis is presented in five parts. In the first, the x-ray apparatus used to obtain the diffraction data is described. In the second, diffraction theory and the general procedure for data analysis are developed. In the third part, a detailed diffraction analysis of the phase behavior of multilamellar vesicles of DPPC in excess water as

a function of temperature over the range 0-50°C is presented. In the fourth part, the phase behavior of two types of lipids in which the molecular structure of the model molecule has been slightly modified (17iPC and 20iPC) are compared to that of the model system. In the final part, the interaction of bromoform with pure DPPC/water multilamellar vesicles is investigated. Results from each of the analyses led to reconsideration of the currently accepted models describing the phase behavior of lipid bilayers.

X-RAY DIFFRACTION APPARATUS

An existing x-ray apparatus [56] was improved in two respects. First, design of the position-sensitive detector (PSD) was modified to improve efficiency and significantly reduce data-collection time. This enabled monitoring of the structure of the bilayers as the phase transformations progressed. Second, an additional PSD was added to the system so that lamellar and interchain structure could be monitored simultaneously. This capability is crucial for determining the state of the bilayer in the low-temperature phases, which exhibit rich structure in the wide-angle region.

The basic apparatus, shown in Figure 5, comprises 1) a sealed-tube x-ray generator (Phillips Electronic Instruments) which produces a beam of nickel-filtered CuKα radiation, 2) a home-built variable-temperature sample stage, 3) two home-built position-sensitive detectors and 4) associated electronics and two multichannel analyzers (MCAs) (Nuclear Data, Inc. ND62).

X-ray generator and sample stage

The x-ray generator produces a beam of nickel-filtered CuK$\bar{a}$ radiation which is pin-hole collimated before impinging on the sample. The sample stage is enclosed with aluminum-coated mylar windows and is aligned by micrometer drives. During measurements, helium gas is flowed through the sample stage, collimator and beam path to reduce air scatter and condensation.

Two complimentary temperature control systems are used to regulate the sample temperature in an overall range of -10 to 100°C. From -10 to 50°C, a Lauda K-2/R circulating temperature bath maintains a constant temperature to ±0.05°C. Above 50°C, a Scientific Instruments 3610 Cryogenic Temperature Controller (with four 8Ω resistors in series for heating and a platinum resistor for temperature sensing) maintains the set temperature to ±0.5°C.

Detection system

The detection system currently in use employs two RC-encoded

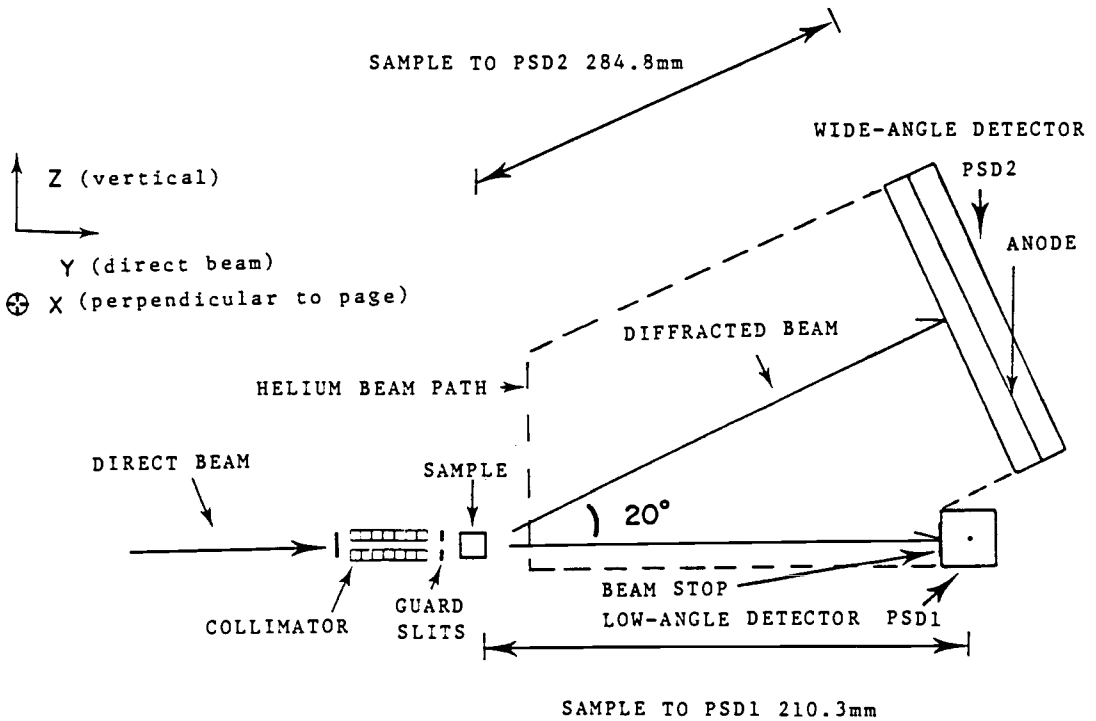

Figure 5: X-ray diffraction apparatus with low- and wide-angle detectors

position-sensitive detectors (PSDs). The design of these PSDs is based on that of a detector previously developed by Lytz in this laboratory [56]. This model will be referred to as the Lytz model. Design improvements which increase both the efficiency and scope of data collection are described below.

General Principles

The Lytz model was based on the design of the detector developed by Borkowski and Kopp [57] in 1968. This type of detector, like that developed by Rutherford and Geiger in 1908, registers and amplifies ionization events resulting from the photoelectric interaction of incident radiation and an ionizable fill gas. The Borkowski and Kopp method, in addition to recording the number of such events, also provides the position of the event along the length of the detector. Figure 6 shows a schematic diagram of a standard Borkowski-Kopp position-sensitive detector and the shape-analysis scheme. This technique uses an anode wire of high resistance (8kΩ) and the inherent detector capacitance ($\sim 10^{-11}$F/m), to produce a distributed RC line. When an ionization event occurs at a particular position in the detector, gas multiplication of charge deposition on the anode wire is induced at a corresponding point. The shapes of the induced pulses are modulated to a degree determined by the RC properties of the detector and by the distances they travel along the anode wire. Timing analysis (cross-over or constant fraction) of the two resultant output pulses of the detector yield the position information. This feature enables instantaneous acquisition of diffraction spectra, which reduces the duration of an experiment from days to hours or minutes with a conventional x-ray source. Many types of position-sensitive detectors, including two-dimensional grid [58,59], multiwire [60] and curved [61] models, are now commonly used for a wide variety of applications [62-65]. Current developments and applications of position-sensitive detectors are summarized in a recent definitive review by Arndt [66].

Specific Design

In the final model of the Lytz detector, which was a flow proportional counter, a carbon-coated quartz fiber of 20μm diameter and

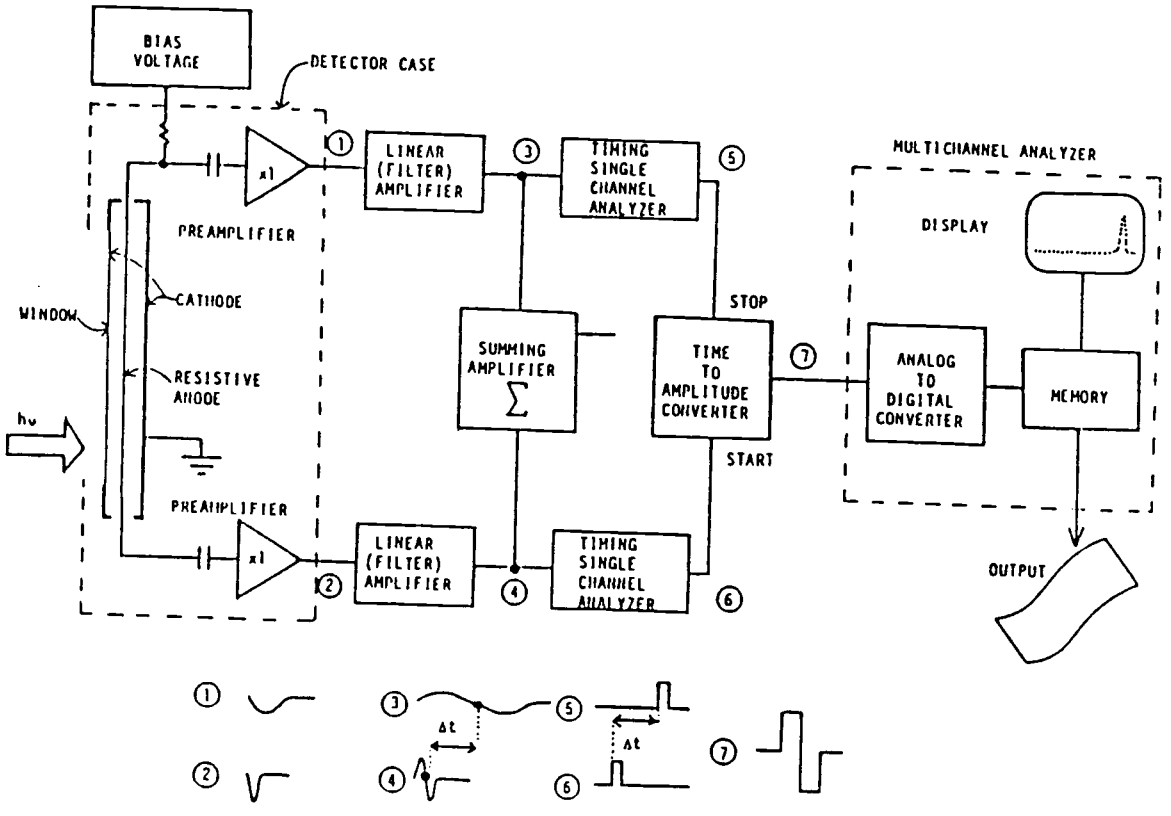

Figure 6: Position sensitive detector and shape analysis scheme, from the thesis of Lytz (56).

an active length of 95mm, served as the high-resistance (~1MΩ) anode. The cathode body was of machined aluminum with a chamber of rectangular cross section (4x4mm). The aluminized-mylar windows (.01mm thick) were o-ring sealed with 1.85 mm-thick aluminum pressure plates attached with ten screws and nuts. The flow gas used was 90% argon-10% methane (P10) at pressures up to 430kPa. At this pressure, counting efficiency was 10%.

Improved Efficiency

The efficiency of the Lytz model was limited by the pressures that could be attained before significant leakage of the flow gas occurred. The quantum counting efficiency ϵ is defined as

$$\epsilon = f_T f_A,$$

in which f_T is the fraction of radiation transmitted through the window and f_A is the fraction absorbed by the flow gas [67,68]. Since this fraction is exponentially dependent on the mass absorption coefficient of the flow gas, which in turn is dependent on the wavelength of incident radiation and the mass density, the efficiency of the detector is greatly influenced by the flow-gas pressure.

Lytz determined the absolute efficiency of his model by comparing the count rate of the detector at a given pressure to the count rate determined by use of a NaI-Tl scintillation detector, assumed to be 100% efficient. At 430 kPa, the highest pressure which could be attained without serious leakage, the efficiency was measured to be 10%.

For the present work, greater efficiency was desired, so the problem of attaining a pressure-tight seal was addressed. First, the points and extent of leakage were determined empirically by immersing the pressurized detector in a reservoir of water and observing the location and rate of bubble formation. To reduce leakage under pressure, the pressure plates were made thicker and longer and the number of pressure points increased and redistributed. Changes in materials for inlet connectors, o-ring lubricant and fiber-mount epoxy decreased leakage further. With the modified design, pressures up to 680 kPa are attained without significant leakage over extended time periods. Table 1 summarizes the physical characteristics of the Lytz-

TABLE 1

Comparison of characteristics of Lytz- and new-model PSDs

	Lytz	new
Usable length	95 mm	95 mm
Window width	4.0 mm	4.0 mm
Chamber depth	4.0 mm	4.0 mm
Anode diameter	20 μm	7 μm
Anode resistance	8 MΩ/m	20 MΩ/m
Pressure	380 kPa	680 kPa
Bias	2200 V	2600 V
Quantum efficiency	0.09	0.95
Number of detectors	1	2
Accessible range	(1/150) to (1/6)Å^{-1}	(1/150) to (1/2.5)Å^{-1}

and new-model detectors.

The absolute efficiency of the new detectors was measured using the method employed by Lytz and found to be 95%. The increased count-rate reflected in the higher efficiency significantly decreases the time necessary to achieve well-resolved diffraction patterns. This is particularly important in the wide-angle region where peaks are generally broader and less well-resolved and peak intensities are relatively low compared with those in the low-angle region.

Increased Range

A second limitation of the Lytz setup arose from its single-detector configuration, with the detector fixed horizontally perpendicular to the beam. This limited the portion of the diffraction pattern which was simultaneously accessible to that corresponding to the lamellar order {(1/150) to (1/6)$Å^{-1}$}, or low angle diffraction.

The simultaneous monitoring of the low- and wide-angle patterns is important for reasons other than convenience. The phase transformations of lipid/water samples are highly sensitive to sample history, including hydration levels, annealing times and heating cycles. This makes simultaneous monitoring of the low and wide-angle regions highly preferable to alternate monitoring.

To record the entire diffraction range simultaneously, a second, identical detector (PSD2) was mounted vertically at an angle 20° from parallel to the beam and ~285 mm from the sample stage, as shown in Figure 5. This configuration extends the accessible range of diffraction to (1/2.5)$Å^{-1}$.

Calibrations

Both detectors were routinely calibrated each time the cylinder of flow gas was changed. Both the low- and wide-angle detectors were calibrated for position linearity and counting efficiency. As explained below, the wide-angle detector was also calibrated for position relative to the beam using diffraction from stearic acid and calcium carbonate.

These routine calibrations were necessary for two reasons. First, the actual percentage of methane in each cylinder of analyzed P10 gas

varies from 9.5 to 10.5%. Since the response of the detector is pressure-dependent, the optimal settings for the decoding electronics will also vary from cylinder to cylinder. Second, although the flow gas is desiccated and particle- and oxygen-filtered before entering the detector chambers, the quality of the quartz collector fibers is found to degrade with use, decreasing linearity and efficiency. The apparent cause of degradation is the buildup of a deposit of unknown origin, especially along the portions of the fiber where diffraction is most intense. This buildup causes localized distortions in the resistivity of the anode, reducing the counting efficiency in the corresponding channels of the MCA. Routine calibration served both to monitor and correct these effects, which occur in all proportional counters and represent a fundamental limit to the useful lifetime of a given anode wire. Replacement of the anode wire was necessary aproximately every six months.

Position Linearity Determined by Point Calibrations

The non-linearity of channel number as a function of fiber position is quantified by a point calibration. A series of apparent peak positions are determined as a function of actual distance along the fiber, giving rise to the comb-like spectrum shown in Figure 7. A curve-fitting routine then generates channel-to-distance conversion coefficients, which in turn are used to obtain the reciprocal-space values for a given detector-sample configuration. Figure 7 shows a typical plot of uncorrected and corrected channel-to-distance data.

Counting Efficiency Determined by Continuous Calibration

The responsiveness of the detector to a given intensity of radiation also will vary as a function of channel number. The continuous calibration is obtained by translating the detector in front of the collimated beam so that the length of the fiber is exposed to a constant intensity. The number of counts per channel are then normalized to the maximum value to generate a correction factor for each channel. Figure 8 shows a typical continuous calibration curve and the same curve corrected for intensity response. The inverted peaks in the uncorrected curve are due to the buildup discussed above.

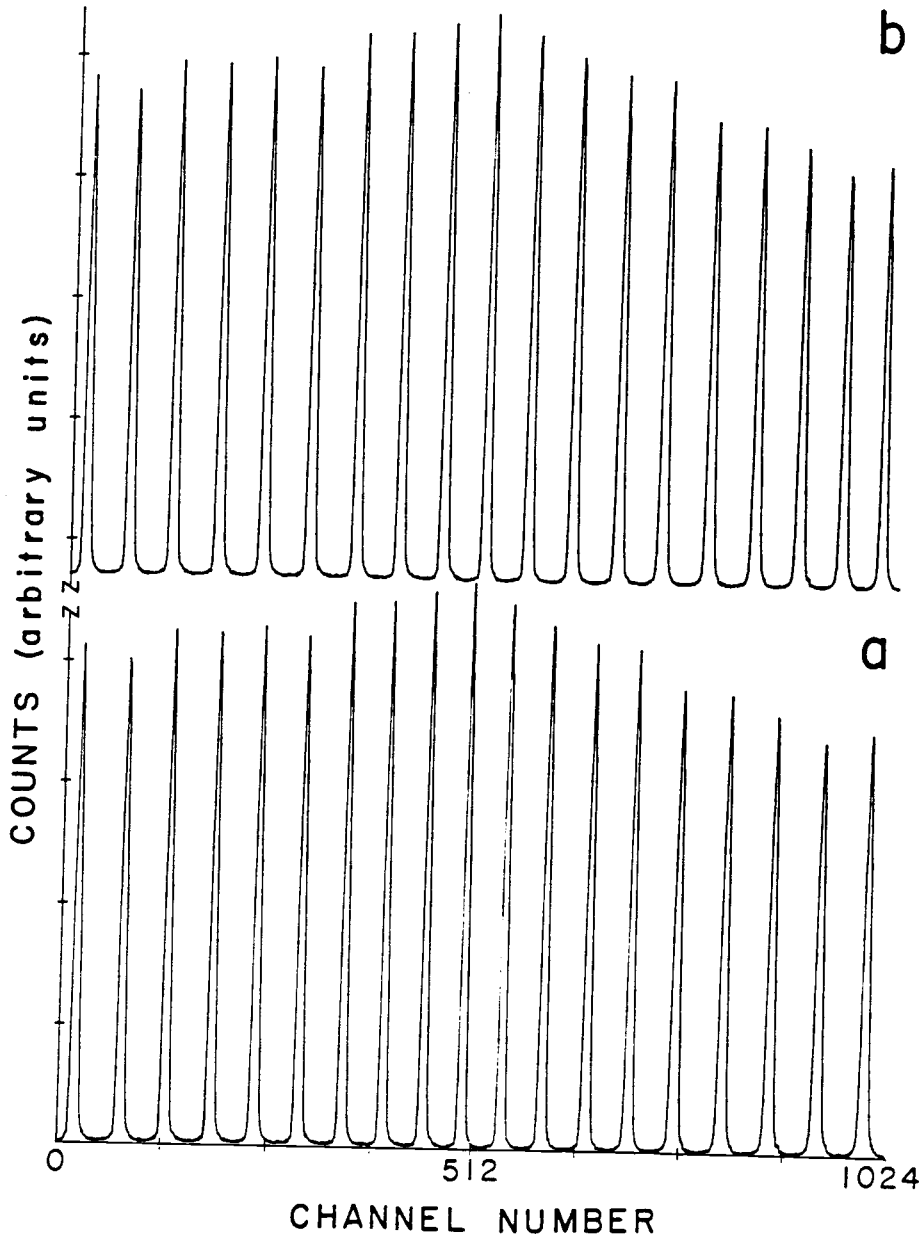

Figure 7: Point calibration of PSD and effect of correction
a) uncorrected, b) corrected

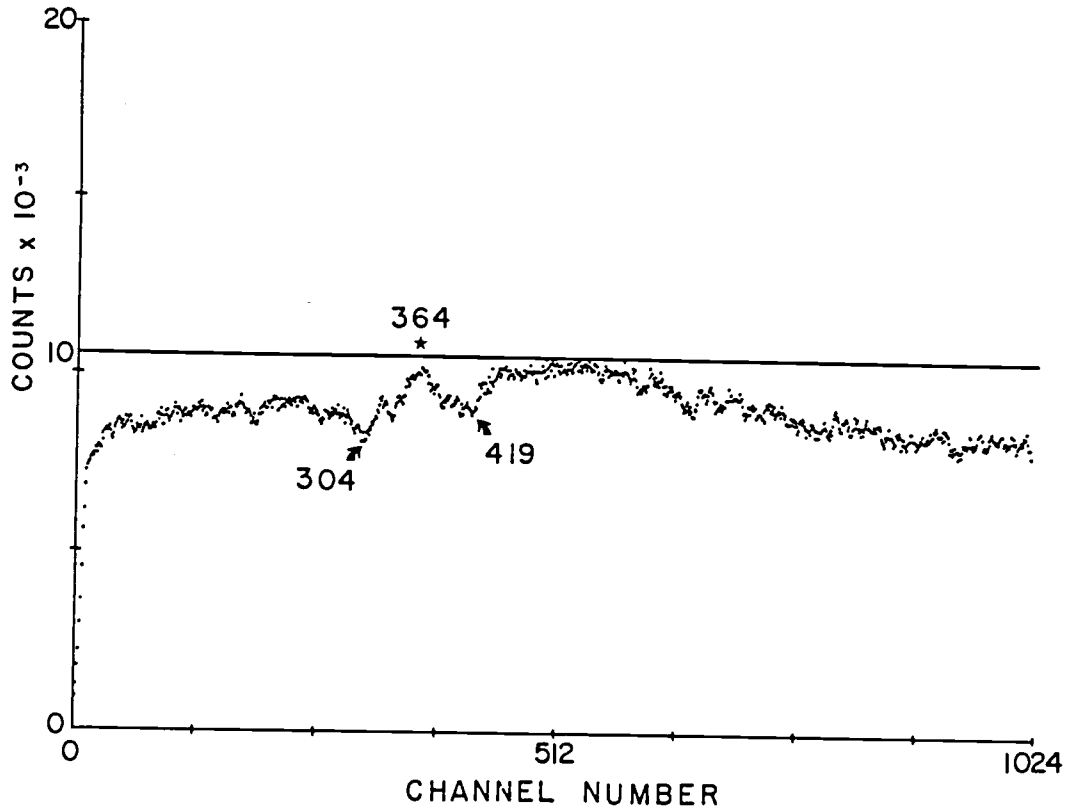

Figure 8: Continuous calibration of PSD and effect of correction: uncorrected ....., corrected _____. The inverted peaks at the arrow positions, which correspond to the positions of first-order reflections from typical samples investigated in this laboratory, represent regions of the anode which have been degraded by extensive exposure. The position which corresponds to the center of the beam stop is indicated with a ✱. Corresponding channel numbers are also indicated.

Calcium Carbonate/Stearic Acid Wide-Angle Calibration

The addition of the second detector to record wide-angle data introduced an additional calibration problem. To assign values in reciprocal space to each channel number corresponding to a position along the detector, three sets of values must be known: 1) the channel-to-distance conversion coefficients, 2) the number of the channel at which the incidence of the diffracted beam is perpendicular to the detector and 3) the angle at which the perpendicular incidence occurs. With this information, distance in millimeters along the detector can be converted directly to distance in Ångstroms.

For both the low- and wide-angle detectors, the conversion coefficients are obtained from the point calibration, as described above. For the low angle detector, obtaining the other two values is straight-forward. The central channel at which the beam incidence is perpendicular to the detector corresponds to the center of the beam stop, so the angle of incidence is 0°.

For the wide-angle detector, the central channel and angle of incidence must be determined empirically. This is normally accomplished by correlating the diffraction pattern of a compound with known peak values of characteristic intensity in the wide-angle region. Calcite ($CaCO_3$) shows two strong reflections in this region, one at $(1/3.04)Å^{-1}$ (211) and one at $(1/3.85)Å^{-1}$ (110) [69] and is commonly used for this purpose. However, since 3.04Å is outside the range of interest, only one reference point in the critical region of the wide-angle spectrum is provided. Therefore, another compound was sought which exhibits intense peaks in the $(1/3.5)Å^{-1}$ to $(1/4.5)Å^{-1}$. Since fatty acids are components of the lipids of interest, they seemed likely candidates.

Stearic acid (C18) is a readily available, inexpensive fatty acid which forms stable crystals. Although two crystal forms of stearic acid, the B form and the C form, are known to be stable at room temperature, they are readily distinguishable by their low-angle diffraction. At 46°C, the B form, which is characterized by a long spacing repeat of 43.85Å [70], undergoes an irreversible transition to the C form, which is characterized by first order peaks at 39.85Å [71]. The C form exhibits two intense peaks in the wide-angle region, at

3.68Å (200) and at 4.11Å (110); this was the form used for the calibration.

The calibration is effected using the following procedure. A 50:50 wt/wt mixture of Baker Analyzed Reagent grade $CaCO_3$ and Applied Science Laboratories stearic acid is ground to a fine homogeneous powder, which is transferred to a sample capillary and the capillary flame-sealed. Both the low- and wide-angle spectra are collected until the channel numbers of the wide-angle peaks positions (at 3.04, 3.68, 3.85 and 4.11Å) can be identified unambiguously (Figure 9). The low-angle spectra are collected merely to confirm presence of the C form and no data is presented here.

To utilize the information from the $CaCO_3$/stearic acid calibration, a BASIC-language computer program was developed in this laboratory by D. J. Griffiths. This program, using estimated values for the central channel and the angle of incidence, the measured sample-to-detector distance and the channel-to-distance coefficients determined in the point calibration, calculates Ångstrom values for the channel numbers corresponding to the observed peak positions. The calculated Ångstrom values are then compared to the known values and the error determined for each peak. This calculation is repeated using different values for the central channel and angle of incidence until the relative errors between the calculated and known peak values are minimized. Calculation of the value in Ångstroms of the prominent peak in the $P\beta'$ phase of DPPC provides an independent check for accuracy. Typical final relative errors between the calculated and known values are less than 1.0%.

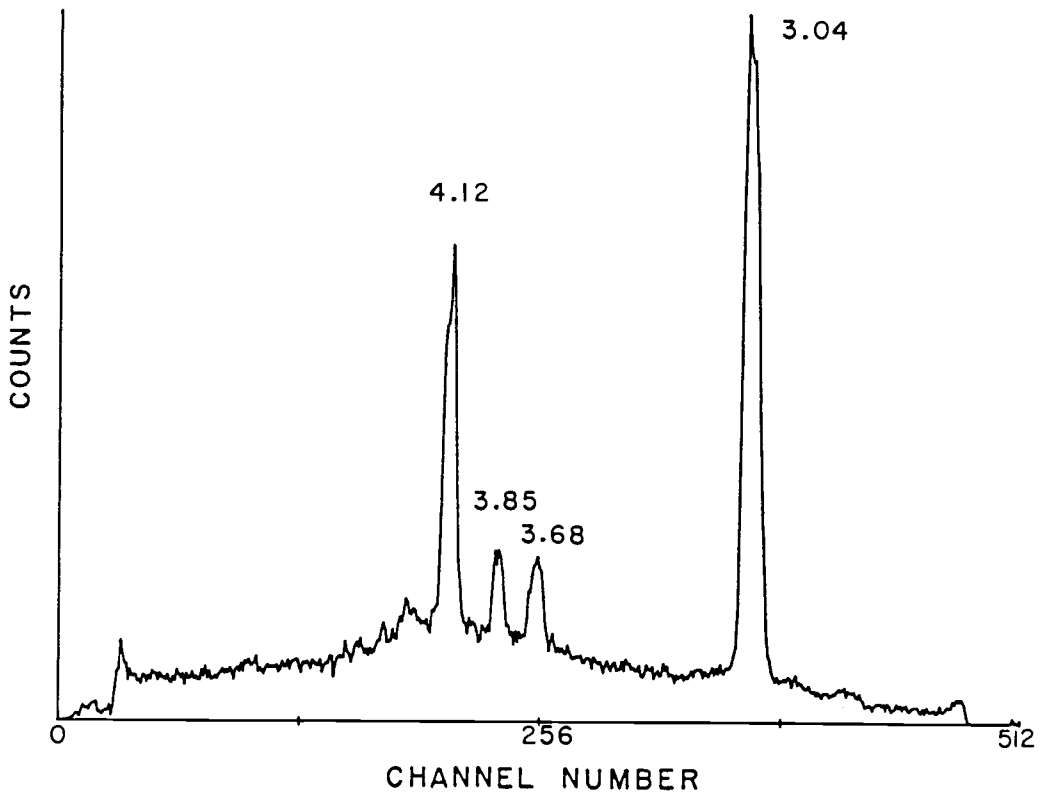

Figure 9: Stearic acid/$CaCO_3$ wide-angle diffraction pattern. Peak positions in real space (Å) are indicated.

DIFFRACTION THEORY

X-Ray Scattering

In diffraction experiments the primary interaction of x-rays with matter is Thomson scattering, in which the incident and scattered radiation have the same wavelength and frequency [72-76]. If the incident wave is not polarized, then the intensity I will vary as a function of the angle φ between the incident and scattered waves (Figure 10a) such that:

$$I = I_0(1/R^2)(e^4/m^2c^4)(1 + \cos^2\varphi)/2 \qquad (1)$$

in which I_0 is the intensity of the incident radiation, R is the distance of the observation point from the reference point, e is the charge of the particle, m is its mass and c is the speed of light. Because of the inverse dependence of the intensity on mass, scattering from an electron is more than $3x10^6$ times greater than from a proton, so x-ray diffraction techniques are sensitive to the presence of the electrons in a sample and the positions of the nuclei must be inferred.

An x-ray diffraction experiment measures only the intensities of points at which constructive interference from the scattered radiation of the sample occurs. To obtain molecular information from this data, the relationship between the interference patterns and molecular packing must be analyzed or assumed.

The interaction of a wave and scatterer is depicted in Figure 10a, which shows a scattering body exposed to a parallel beam of monochromatic x-rays with a wavelength λ and a direction specified by the unit wave vector $\underline{S}_o$ with some of the scattered radiation, represented by unit vector $\underline{S}$, directed at an angle φ relative to the direction of the incident beam. For a single electron at P, the scattering amplitude would be the square root of Equation (1):

$$A = A_o(1/R)(e^2/mc^2)p^{1/2}, \qquad (2)$$

in which $p = (1 + \cos^2\varphi)/2$, the polarization factor.

The distribution of electrons in the scatterer can be represented by an electron density function $\rho(\mathbf{r})$, in which $\mathbf{r}$ is a vector ranging over the volume of the scatterer. The number of electrons per volume

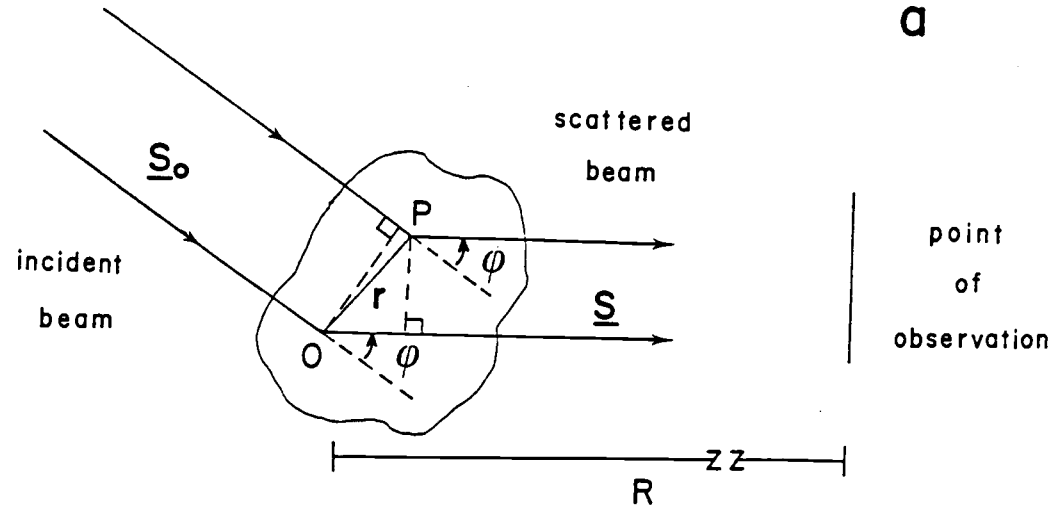

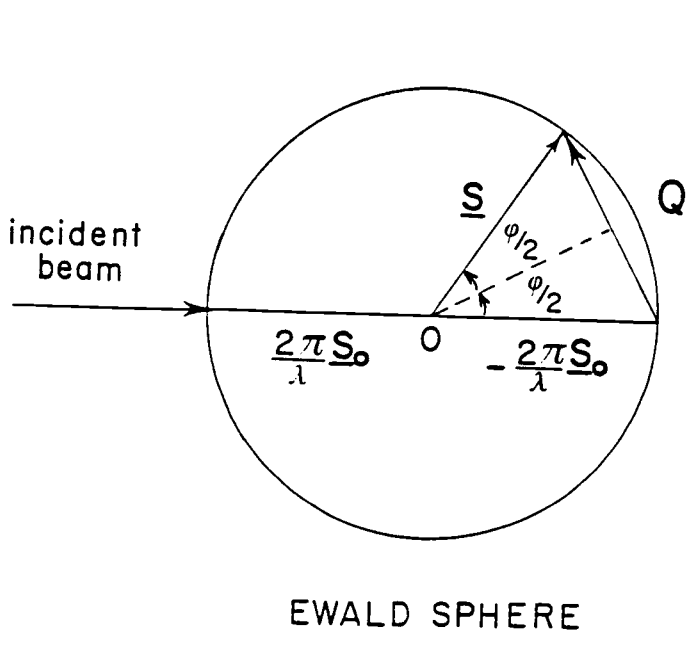

Figure 10: a) Interaction of x-rays with scattering body and
b) relation of Q to $\underline{S}$ and $\underline{S_o}$

element at r is $\rho(r)\delta r$.

Interference occurs because of the phase differences which arise from differences in path length between radiation scattered from different points in the scatterer. To evaluate the phase difference between scattered radiation from the two points O and P, the path difference can be expressed

$$r\cdot\underline{S} - r\cdot\underline{S_o} \qquad (3)$$

so the phase difference is

$$(2\pi/\lambda)r\cdot[\underline{S} - \underline{S_o}]. \qquad (4)$$

If a vector Q is defined as

$$Q = [\underline{S} - \underline{S_o}] \qquad (5)$$

the expression for the phase difference simplifies to

$$(2\pi/\lambda)r\cdot Q. \qquad (6)$$

From Figure 10b, which shows the relationship of Q to $\underline{S}$ and $\underline{S_o}$, the modulus of Q is seen to be

$$Q = |Q| = (2\pi/\lambda)\sin(\varphi/2). \qquad (7)$$

Allowing $\underline{S}$ to range in all directions, with $\underline{Q}$ always originating a O′, defines the Ewald sphere.

To describe the scattering from the whole scattering body, the expression on the right in Equation (2) must be multiplied by $\rho(r)\delta r$. The expression for the wave at an angle φ from the incident beam scattered from the entire body is then

$$A_o(1/R)(e^2/mc^2)p^{\frac{1}{2}}\int\rho(r)\exp\{ir\cdot Q\}\delta r. \qquad (8)$$

Omitting the factors before the integral, which are applied as correction factors or cancel out when relative intensities are considered, the remaining expression is clearly related to the Fourier transform of $\rho(r)$:

$$F(Q) = \int\rho(r)\exp\{ir\cdot Q\}\delta r, \qquad (9)$$

with the integration performed over all space. If the assumption is made that the body described by $\rho(r)$ includes all the electron density in accessible space, integration over the dimensions of the body is equivalent to integration over all space and Equation (9) can be applied to the scattered wave. The intensity I(Q) of the scattered

wave at φ is then

$$I(\mathbf{Q}) = F(\mathbf{Q})F^*(\mathbf{Q}), \qquad (10)$$

with the complex conjugate $F^*(\mathbf{Q}) = \int \rho(\mathbf{r})\exp\{-i\mathbf{r}\cdot\mathbf{Q}\}\delta\mathbf{r}$.

Since the modulus of Q, as defined in Equation (7), is inversely proportional to the wavelength of the x-rays, the units of the diffracted intensity are those of reciprocal length. Because of this reciprocal relationship, the effect of diffraction is to define the dimensions of the scatterer in what is termed reciprocal space. In fact, for convenience, crystallographers generally define reciprocal space in terms of the vector $\mathbf{s} = \mathbf{Q}/2\pi$, so that distances in reciprocal space can be converted directly to real space. This convention will be used in the next section to analyze the wide-angle diffraction patterns from the lipid dispersions.

The electron density function of a known system can be described mathematically in more detail. For simplicity, consider a one-dimensional crystal, as shown in Figure 11, in which a pattern is repeated at regular intervals of **c** along an axis designated the c-axis. The Fourier transform of this system can be expressed as the transform of a single layer F(Q) multiplied by the transform of the lattice T(Q). For N layers in the lattice,

$$T(\mathbf{Q}) = \sum_{j=1}^{N} \exp\{i\mathbf{r}_j\cdot\mathbf{Q}\}, \qquad (11)$$

in which j indicates a point in the lattice relative to an arbitrary reference point. When the summation in Equation (11) is carried out, it can be shown that

$$T(\mathbf{Q}) = \exp\{i(N-1)\mathbf{c}\cdot\mathbf{Q}/2\}\frac{\sin(N\mathbf{c}\cdot\mathbf{Q}/2)}{\sin(\mathbf{c}\cdot\mathbf{Q}/2)}, \qquad (12)$$

which reduces to the interference function for a one-dimensional crystal S(Q) when multiplied by its complex conjugate:

$$S(\mathbf{Q}) = T(\mathbf{Q})T^*(\mathbf{Q}) = \sin^2(N\mathbf{c}\cdot\mathbf{Q}/2)/\sin^2(\mathbf{c}\cdot\mathbf{Q}/2). \qquad (13)$$

The intensity of the scattered radiation is

$$I(\mathbf{Q}) = S(\mathbf{Q})F(\mathbf{Q})F^*(\mathbf{Q}). \qquad (14)$$

For infinitely large N, S(Q) is zero except when $\mathbf{c}\cdot\mathbf{Q} = 2\pi l$, with l an integer. The larger N is, the sharper the peaks, which are separated by the distance $2\pi/c$. If Q parallel to **c** is considered, so that $Q = 2\pi l/c$, then

$$Q = (4\pi/\lambda)\sin\theta = 2\pi l/c \qquad (15)$$

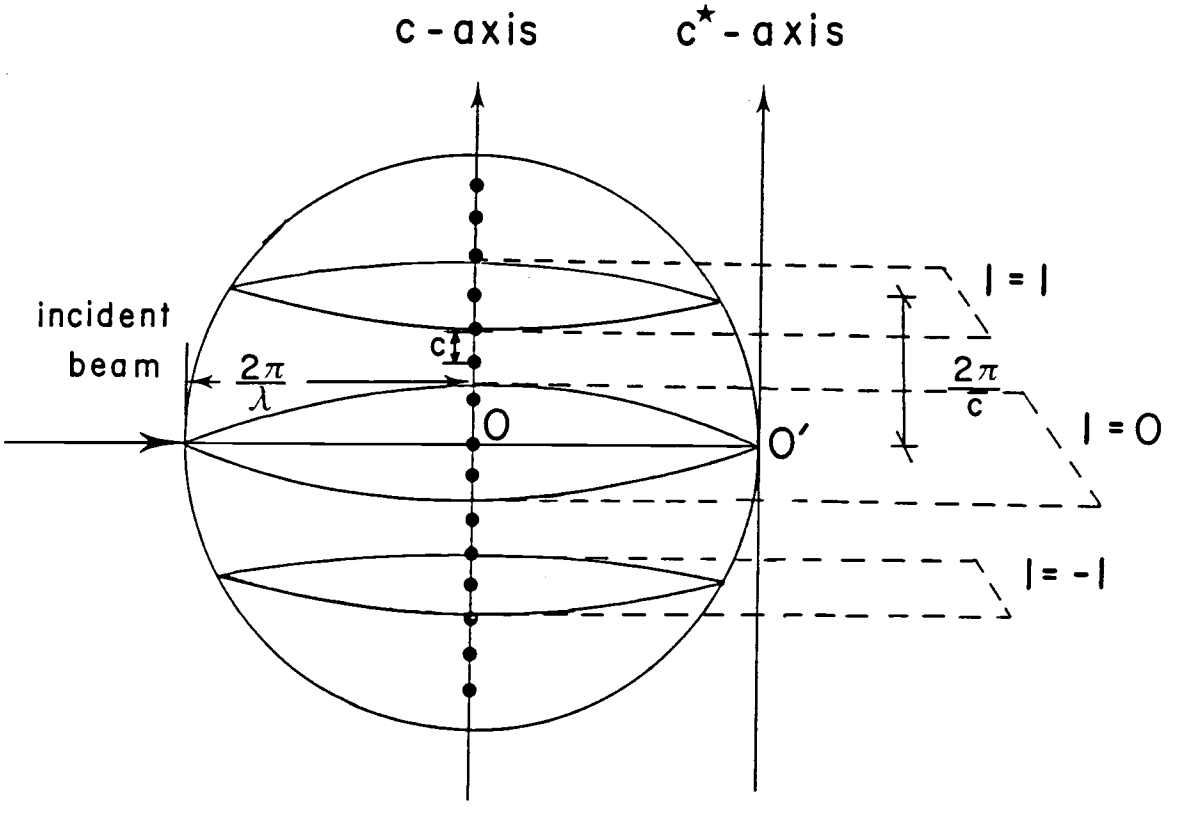

Figure 11: Diffraction of x-rays by a one-dimensional crystal. The scattering points are separated by a distance c along the c-axis in real space and by $2\pi/c$ along the c*-axis in reciprocal space.

if θ is identified as $\varphi/2$ of Figure 10a. Rearrangement of Equation (15) leads to the expression

$$2c\sin\theta = l\lambda, \qquad (16)$$

which is Bragg's law and can be extended to three dimensions.

Bragg's law is conceptually useful because it implies that that the process of diffraction is equivalent to the process of reflection of the incident radiation from lattice planes, as shown in Figure 12.

Electron density profiles

The electron density profile of a one-dimensional crystal can be deduced from the intensities of the c-axis reflections and the inverse Fourier transform of the expression in Equation (9). In this case, the inverse transform can be expressed as follows:

$$\rho(x) = \sum_{l} F(l)\exp\{-2\pi i l x\}, \qquad (17)$$

in which x is the fractional translation along the c-axis and a summation replaces the integral because the diffraction pattern is an array of discrete points, rather than a continuous distribution. A diffraction experiment yields values of the intensity I(l), which is the square of F(l), so the contributions of the real and imaginary parts to F(l), and therefore the phase, are not known. The problem of retrieving this information is simplified in a centrosymmetric system because the phase factors are +1 or -1.

The expression for the inverse transform is then:

$$\rho(x) = F(0) + \sum_{l\neq 0} F(l)\cos(2\pi l x) \qquad (18)$$

The structure factors F(l) are obtained from the relative intensities I(l):

$$I(l) \propto |F(l)|^2 \qquad (19)$$

Although the intensity at $l = 0$ cannot be determined since it corresponds to the position of the direct beam, this term does not affect the shape of the profile function, but acts as an offset. The measured intensities at $l \neq 0$ must be corrected for the effects of diffraction geometry and partial beam polarization, such that

$$F(l) \propto \frac{1 + \cos^2 2\theta}{\sin^2\theta\cos\theta} I(l)^{1/2} \qquad (20)$$

for powder patterns. At low angles, the correction term in Equation

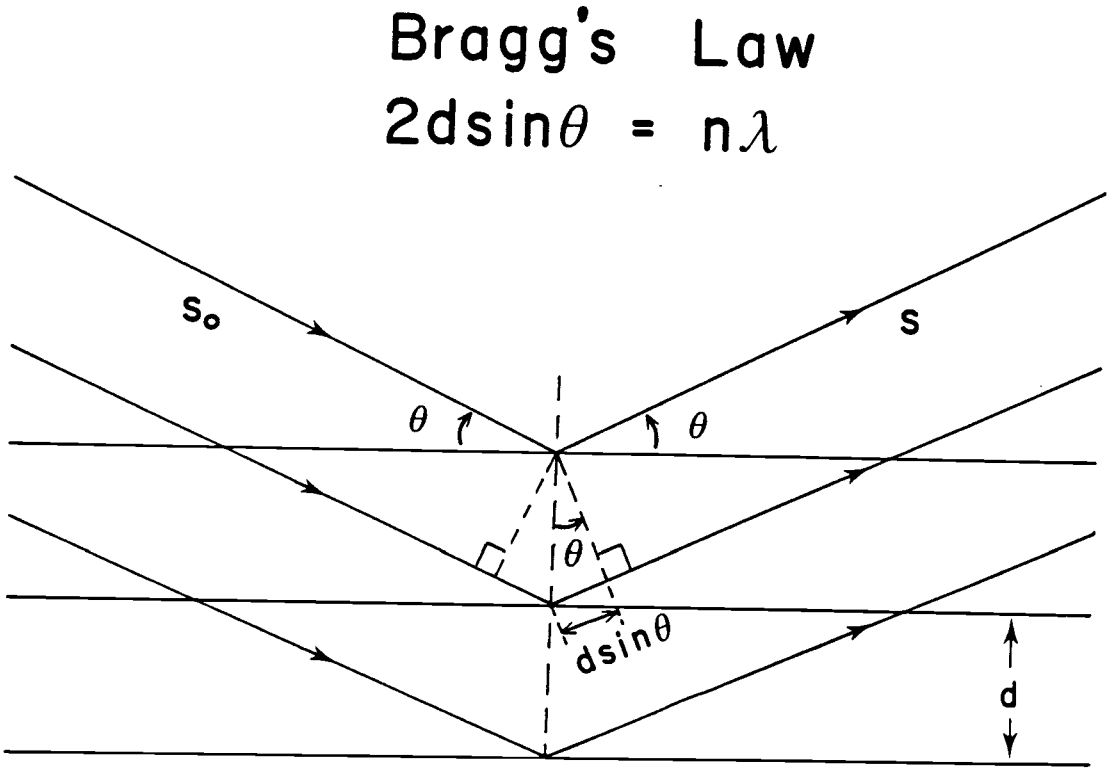

Figure 12: Bragg's law: reflection from lattice planes

{20} is equal to 1^2.

The only remaining ambiguity is in the sign of each structure factor. For model membranes, these are determined by trial and error and comparison with the resulting electron density profiles with the known physical properties of bilayers. A more detailed treatment of low-angle x-ray diffraction from membranes is given by Franks and Lieb [77].

Analysis of 'powder' patterns from multilamellar vesicles

The types of samples investigated here are unoriented multilamellar vesicles, which give diffraction patterns analogous to those from polycrystalline samples in conventional diffraction work. As shown in Figure 13, irradiation of such samples produces cones of diffraction from crystallites for which the Bragg conditions ($n\lambda = 2d\sin\theta$) are met. Unless otherwise specified, diffraction patterns of this type are discussed.

For a linear or planar detector, this leads to the relationship

$$d = n\lambda/2\sin[\tfrac{1}{2}\tan^{-1}(y/D)], \qquad \{21\}$$

in which d is the repeat distance, λ is the wavelength of the incident radiation, n is an integer, y is the distance of the diffracted intensity from the position of normal beam incidence along the detector and D is the distance between the sample and the detector.

The major feature of diffraction patterns from multilamellar vesicles is the presence of evenly spaced peaks in the low angle region from $\sim(1/150)\text{Å}^{-1}$ to $\sim(1/10)\text{Å}^{-1}$. These peaks are reflections from the interlamellar order. From them, the repeat distance d of a bilayer can be calculated directly using the diffraction geometry and Equation {21}.

Molecules which form membranes have two chemically and structurally different components, the bulky, polar head groups and the cylindrical, hydrocarbon side chains. Flexibility in both the head groups and the sidechains allows the two portions of the molecules to order along different axes [78-80]. A cross-section through the headgroup region will exhibit a different lattice net than one through the bilayer interior, as shown in Figure 14. Reflections from both subcells are evident in the wide-angle region of the x-ray diffraction

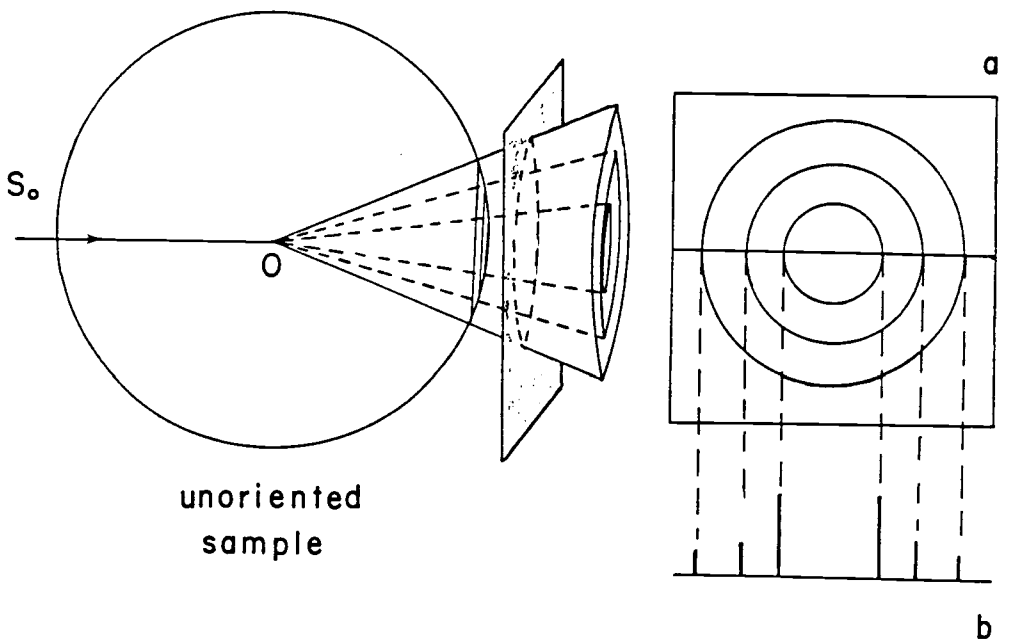

Figure 13: Diffraction from unoriented samples. The resultant patterns observed for a) two- (film) and b) one-dimensional (anode wire) detectors are also shown.

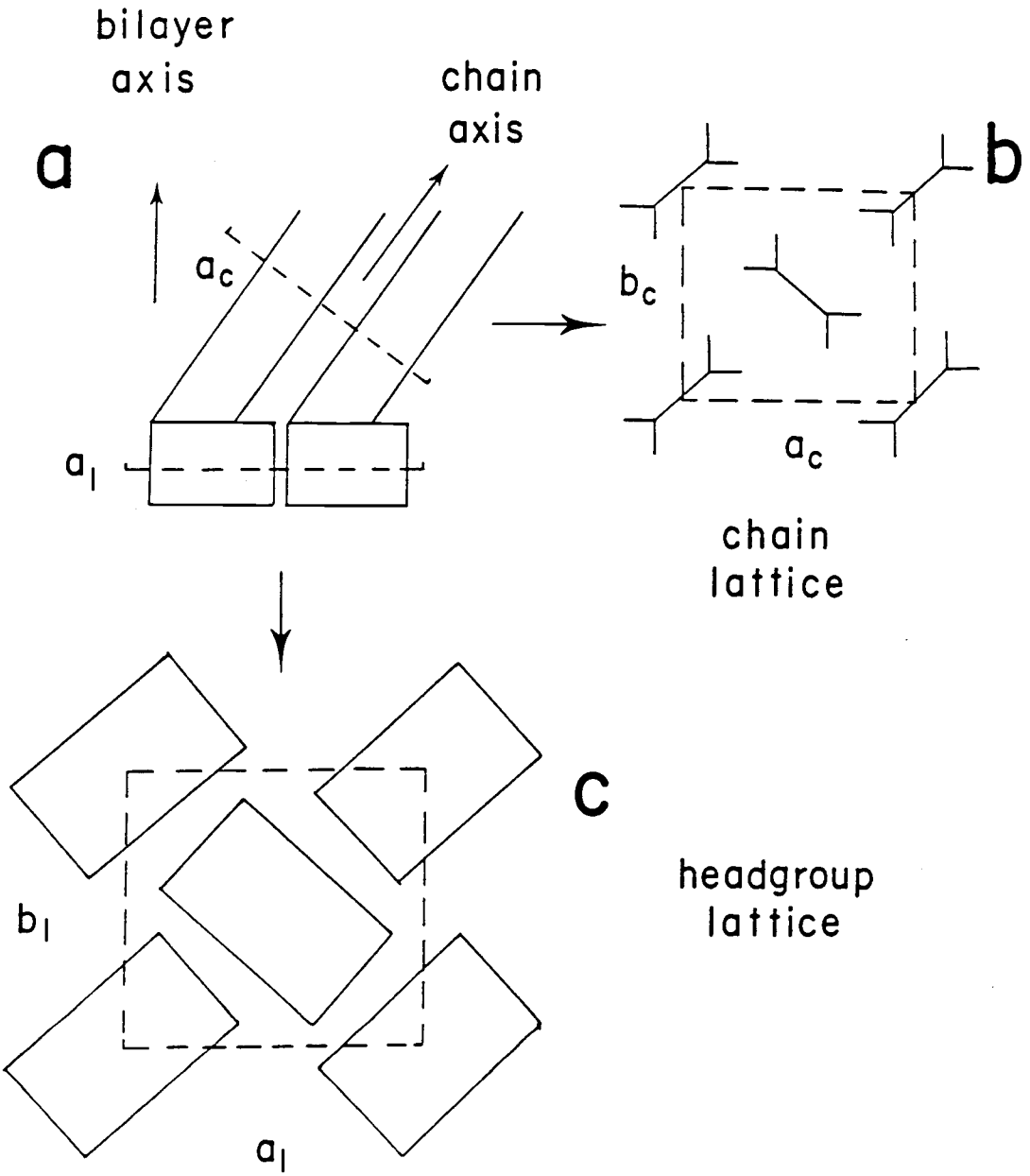

Figure 14: Headgroup and sidechain lattice net planes. a) side view of a pair of adjacent lipid molecules, b) cross-sectional view in the hydrocarbon region of the bilayer perpendicular to the sidechain axes and c) cross-sectional view in the headgroup region of the bilayer in a plane parallel to the bilayer plane

patterns of lipids. The major peaks from the headgroup order occur in the $(1/10)Å^{-1}$ to $(1/6.5)Å^{-1}$ region, while those from the sidechain packing are in the $(1/4.5)Å^{-1}$ to $(1/2.5Å)^{-1}$ region of the spectrum. If these reflections are correctly assigned, the structure of the bilayer can be obtained directly.

The way in which the side chains and head groups pack within the bilayer are strongly interdependent. Independent analysis of the reflections from each part of the bilayer provides clues to the sidechain configuration, although unambiguous interpretations based on results from fully hydrated, unoriented samples are difficult to make [74,81,82]. The subcell parameters can be obtained most directly by viewing the observed diffraction peaks as reflections from lattice planes. The interplane distances in reciprocal space can then be converted directly to real space and the remaining lattice parameters calculated geometrically.

Plane lattices

Figure 15 shows the relationship of the observed reflections to the plane lattice dimensions. If the two-dimensional lattice is hexagonal, only one peak is observed in the wide-angle region, since all the distances between neighboring atoms are the same. If the packing is primitive rectangular, two peaks which correspond directly to the reciprocal cell axes are exhibited. If the arrangement of atoms in the plane is centered rectangular (also referred to as distorted hexagonal), two peaks indicate the presence of two intermolecular distances. Three peaks in the wide-angle region indicates that the plane lattice is a parallelogram.

The distances between atoms, chains or molecules in a centered rectangular lattice can be calculated using the relationship

$$\alpha = \cos^{-1}(s_2^{-1}/2s_1^{-1}), \qquad (22)$$

in which s_i is the position of the ith wide-angle peak in units of reciprocal Ångstroms, $I(s_2^{-1}) < I(s_1^{-1})$ and α is the angle shown in the diagram of Figure 15. Then

$$a = 2(s_1^{-1}), \qquad (23)$$

$$b = (s_2^{-1})/\sin\alpha. \qquad (24)$$

Each atom is surrounded by two atoms at a distance b and four molecules

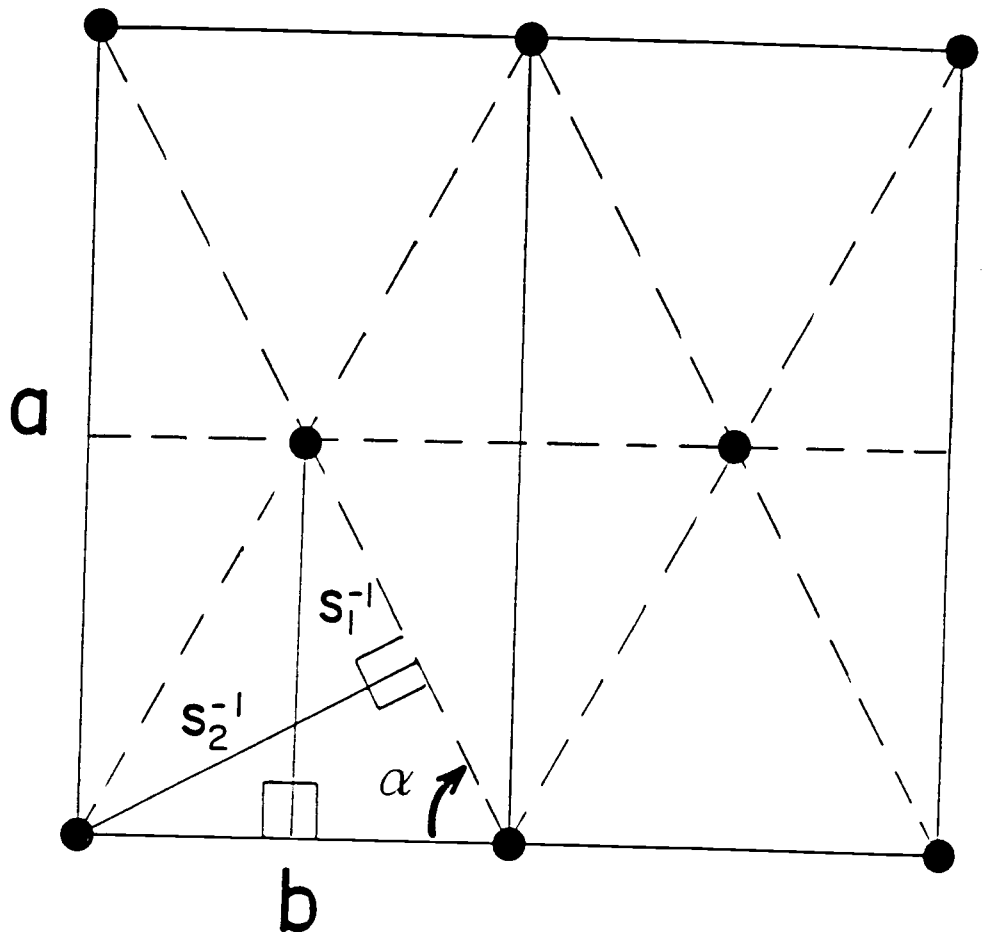

Figure 15: Relationship of oberved reflections to lattice dimensions for a centered rectangular (distorted hexagonal) plane lattice. The angle α is related to the observed reflections by $\cos\alpha = s_2^{-1}/(2s_1^{-1})$ and the cell edges by $a = 2s_1^{-1}$ and $b = s2_1^{-1}/\sin\alpha$.

at a distance $d = (s_1^{-1})/\sin\alpha$. The area per molecule or chain A is determined by a and b, however, such that

$$A = bs_1^{-1}. \tag{25}$$

If the packing is hexagonal, α is 60° and s_1 and s_2 are identical so that only one peak is observed at s. The second dimension b is then related to the observed peak by

$$b = s^{-1}/\sin 60° \tag{26}$$

and the area is

$$A = bs^{-1}. \tag{27}$$

If the plane lattice is primitive rectangular, $\alpha = 90°$, $a = s_1^{-1}$ and $b = s_2^{-1}$, and $A = ab$.

If three strong peaks occur in the wide-angle region, a non-rectangular plane lattice is indicated and the reflections index as

$$1/d_{hk} = [(h/a_p\sin\gamma)^2 + (k/b_p\sin\gamma)^2 - 2(h/a_p\sin\gamma)(k/b_p\sin\gamma)\cos\gamma]^{\frac{1}{2}}, \tag{28}$$

in which a_p and b_p are the cell edges and γ is the angle between them. In this case, the area A is given by

$$A = b_p s_2^{-1}. \tag{29}$$

Application of this analysis to the low-, intermediate- and wide-angle regions of the diffraction patterns from lipid bilayers thus yields three parameters: the lamellar repeat distance d, the area per molecule A_l and the area per side chain A_c. These parameters can be used to calculate other bilayer parameters, such as thickness of the lipid bilayer, sidechain tilt angle and hydration level, leading to a comprehensive description of the bilayer in a given phase. The method by which this is accomplished is presented in the next section. The analysis will be used to reevaluate the bilayer parameters of the phases of DPPC and to compare the structures of perturbed bilayers to those of pure DPPC.

STRUCTURAL PARAMETERS OF FULLY HYDRATED BILAYERS OF DPPC

Unperturbed Model

To assess the effects of perturbations to a particular system, the characteristics of the unperturbed model system should be well-defined, if not well-understood. The utter importance that the model system be carefully defined is readily evident upon surveying the literature concerning lipid phases and phase transitions. That the phases of the pure lipids are not yet fully characterized and are only partially understood physically is somewhat surprising. In part, this situation is due to differences in the physical requirements of the various experimental techniques applied and it is exacerbated by the lack of agreement among experimentalists upon preparative and procedural protocols for model membrane studies. The necessity that each laboratory establish its own model system and characterize it carefully is dictated by the sensitivity of the phase behavior and structural parameters of model membranes to composition, preparative technique and thermal history. For studies in this laboratory, a suspension of fully hydrated multilamellar vesicles of pure DPPC was chosen as the unperturbed model system.

Choice of system

Fully-hydrated multilamellar vesicles are convenient model systems for several reasons. MLVs are thermodynamically stable and are sufficiently well-ordered to produce a powder-type diffraction pattern under x-ray irradiation. In addition, sample preparation is relatively straight-forward. Hydration level is eliminated as a variable and maximum hydration is maintained simply by sealing the sample tube.

DPPC was chosen as the model lipid for several reasons. First, it is a stable, zwitterionic (and therefore neutral) phospholipid which is commercially available in high purity. Second, it exhibits four lamellar phases in a temperature range which is experimentally convenient. Third, it is currently the most widely-studied synthetic lipid, so results of the studies presented here can be compared with previous work. Fourth, as a phospholipid, it is representative of the

major lipid fraction of many biological membranes.

Objectives

In the work presented here, parameters derived from diffraction data in the low-, intermediate- and wide-angle regions of the diffraction patterns from fully-hydrated multilamellar dispersions of DPPC will be used to describe the bilayer structures in each phase. Particular attention is paid to the subgel phase, which has only recently been identified [82-86] and which has not yet been fully characterized. A second focus is on the structural changes occurring during the phase transformations to gain a clearer understanding of the molecular events involved. A third objective is to use the diffraction data to determine unambiguously the presence and degree of tilt in the sidechains in the rippled phase.

Materials and Methods

The DPPC used in the experiments for these studies, obtained from Sigma Chemical Company, was stated to be >99% pure. Its purity was confirmed by TLC, so the lipid was used without further purification. The water of hydration was purified in a Millipore "Milli-Q" ultrafiltration system. The measured resistivity was greater than 15MΩ-cm and the pore size of the final filter was 0.22μm.

The MLV dispersions of DPPC were prepared by the following standard method. The dry lipid was dissolved in a 50:50 $CHCl_3$/MeOH solution in a glass vial and the solvent removed by evaporation under a stream of N_2, followed by overnight vacuum desiccation. The sample was hydrated at a temperature above the main transition temperature (45-50°C), vortexed vigorously for one minute and incubated for one hour at the hydration temperature with intermittent, brief vortexing. The resulting suspension was centrifuged to concentrate the lipid phase in the bottom of the vial. A large portion of the excess water phase was removed and the lipid sample transferred to 1mm-diameter glass capillaries (1-2mg/capillary). The lipid phase was further concentrated by centrifugation and all but a small meniscus of excess water removed. The capillaries were then flame-sealed and centrifuged at 5500xg for 1-2 hours to obtain sufficiently high concentrations for

x-ray studies. Samples were either annealed at 0°C in the x-ray sample stage until the low- and wide-angle patterns were stable in time (≥70hrs) or annealed in the refrigerator at 4°C for at least one week and transferred quickly to the cooled sample stage. Identical results were obtained with both methods.

Analysis of x-ray data to obtain bilayer structure

The general procedure for determining a bilayer structure uses different types of information obtained from different regions of the diffraction pattern. The complete diffraction pattern extends roughly from $(1/100)\text{Å}^{-1}$ to $(1/3)\text{Å}^{-1}$. The reflections in the $(1/100)\text{Å}^{-1}$ to $(1/10)\text{Å}^{-1}$ region (low-angle), originating from the lamellar structure, correspond to the repeat distance d and provide the relative intensities for calculation of projected electron density profiles. The structure factors F_h are obtained from the integrated relative intensities $(n^2 I_h/I_1)^{\frac{1}{2}}$ using the relation:

$$F_h = (n^2 I_h/I_1)^{\frac{1}{2}}\cos(2\pi hx/d) \qquad (30)$$

in which x is a fractional distance along the repeat axis.

Peak positions in the $(1/10)\text{Å}^{-1}$ to $(1/6)\text{Å}^{-1}$ region (intermediate-angle) are used to determine the unit cell dimensions a_1 and b_1 in the headgroup region and thus the area per molecule A_1. For a primitive or centered rectangular cell,

$$A_1 = a_1 b_1/n_1, \qquad (31)$$

in which n_1 is the number of lipids per unit cell.

Peak positions in the $(1/6)\text{Å}^{-1}$ to $(1/3)\text{Å}^{-1}$ region (wide-angle) originate from sidechain order and are used in a similar manner to determine the axes a_c and b_c of the two-dimensional unit cell and A_c:

$$A_c = a_c b_c/n_c, \qquad (32)$$

in which A_c is the area per chain and n_c the number of chains per unit cell. With this data, the tilt angle of the side chains Φ can be calculated:

$$\Phi = \cos^{-1}(2A_c/A_1) \qquad (33)$$

If the volume of the lipid is also available, the information from the diffraction experiments is sufficient to obtain the remaining bilayer parameters defined in Figure 16 and listed in Table 2. For DPPC, the molecular volume at a given temperature can be obtained from specific

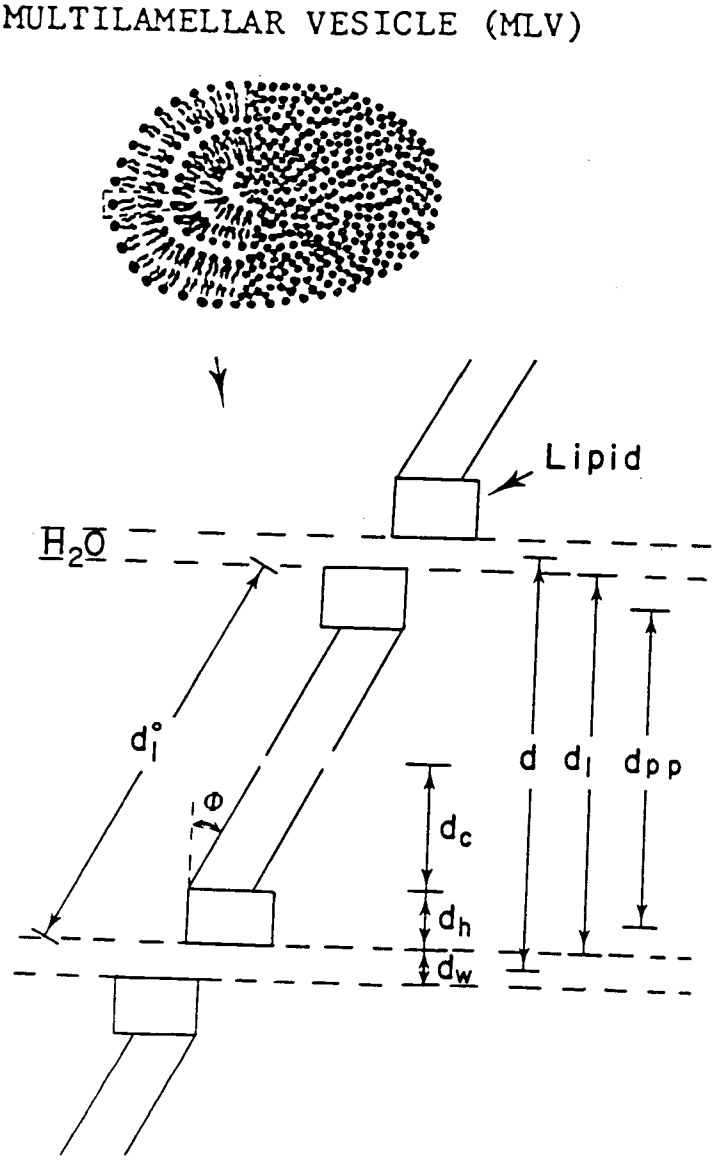

Figure 16: Structural parameters for lipid bilayers

d (Å): lamellar repeat distance from spacings in low-angle
d_l (Å): head-to-head distance in tilted lipids
d_l° (Å): head-to-head distance in untilted lipid
d_{pp} (Å): peak-to-peak distance in projected electron density profile
d_w (Å): thickness of the water region between bilayers
d_c (Å): thickness of the hydrocarbon portion of a lipid molecule
d_h (Å): width of the head group of a lipid molecule
Φ (°): tilt of the sidechain axes relative to bilayer normal

volume measurements [87,88].

The remaining parameters are calculated as follows. The length of the lipid portion of the bilayer when the molecules are untilted ($d_l°$) is related to the volume and sidechain area by the relation:

$$d_l° = V_l/A_c. \quad (34)$$

The width of the lipid portion of the bilayer when the chains are tilted (d_l) is then:

$$d_l = d_l°\cos\Phi. \quad (35)$$

If d_l is compared to d_{pp}, the peak-to-peak distance from the corresponding electron density profiles, changes in the headgroup configuration from phase to phase or system to system can be inferred.

The hydration level (n_w = mol H_2O/mol lipid) can also be obtained from these measurements:

$$d_w = d - d_l, \quad (36)$$

so

$$n_w = A_l d_w/2V_w, \quad (37)$$

in V_w is the molecular volume of water (29.9Å^3).

The volume of the lipid and its associated waters (V_x) is:

$$V_x = A_l d/2 = n_w V_w + V_l. \quad (38)$$

Results

Figure 17 shows the diffraction patterns from MLVs of DPPC in excess water as the temperature is raised from ~0°C after at least three days annealing. Data are collected at each temperature for 6-12 hours, so each pattern represents an equilibrium configuration. Table 2 lists the observed and calculated bilayer parameters for samples of pure DPPC in excess water. Figure 18 shows the electron density profiles in each phase and Table 3 lists the relative intensity data from which the profiles were generated.

Subgel phase L_c'

The low-temperature subgel phase L_c' [82-85] is characterized by a high degree of order. The low angle diffraction corresponds to a lamellar repeat distance of 59.5Å.

The sidechain area is calculated from lattice parameters based on the assignment of the (1/4.44)Å^{-1} and (1/3.86)Å^{-1} peaks to the (2′0′)

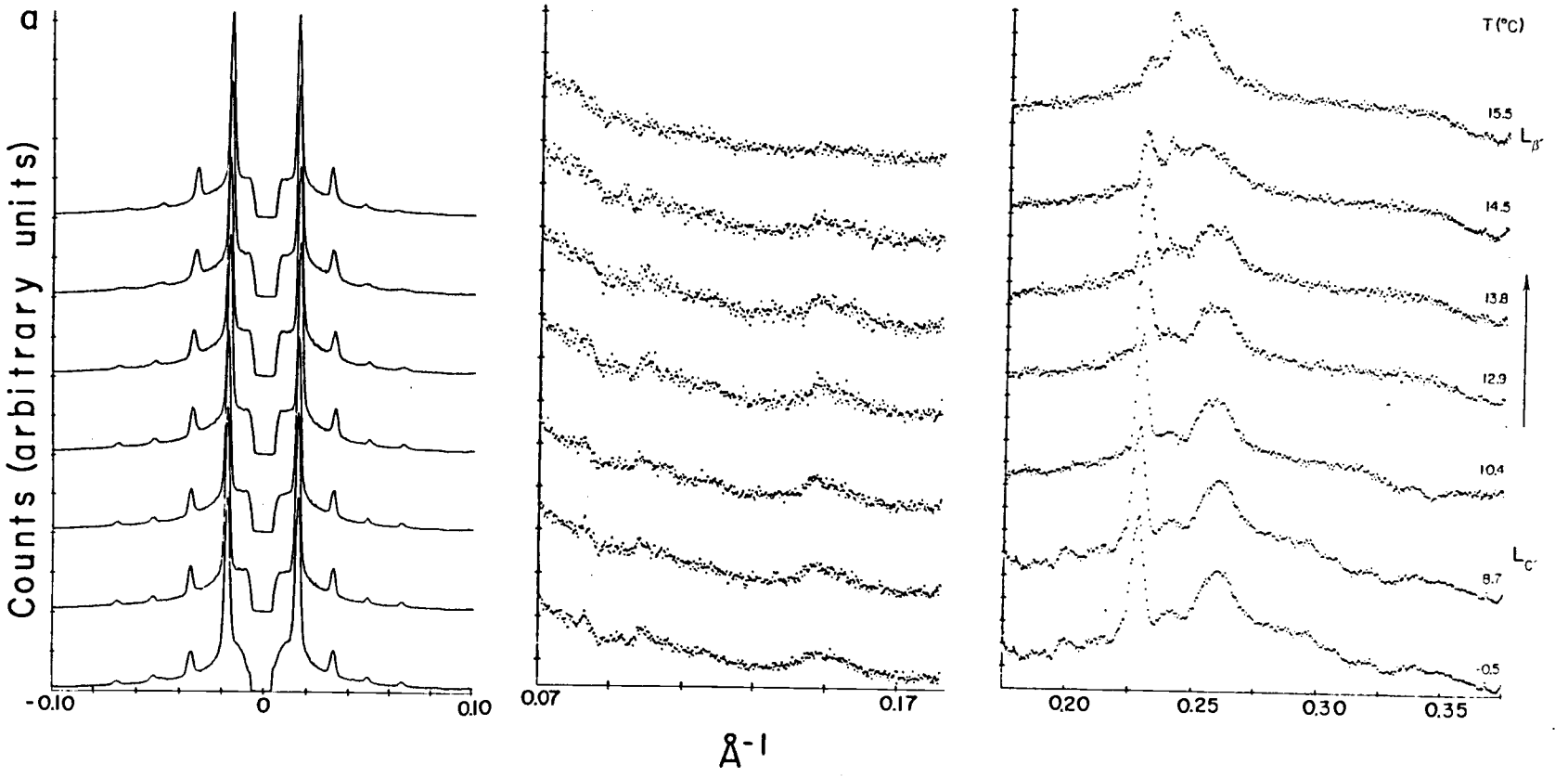

Figure 17: Low-, intermediate- and wide-angle diffraction patterns from MLVs of DPPC in excess H_2O as a function of temperature.
a) subgel $L_{c'}$ to gel $L_{\beta'}$ phases

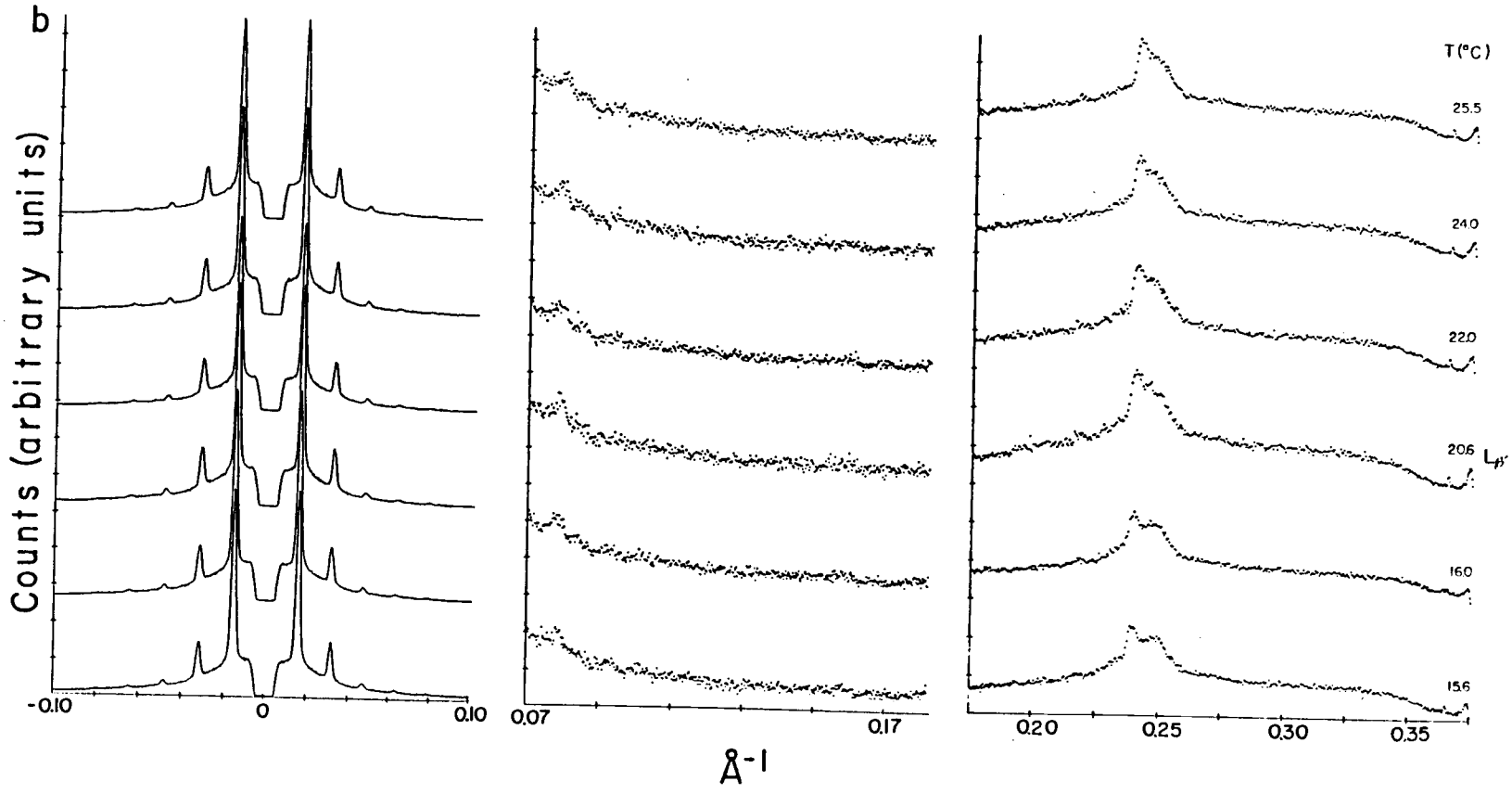

Figure 17 continued: Low-, intermediate- and wide-angle diffraction patterns from MLVs of DPPC in excess H_2O as a function of temperature. b) gel $L_{\beta'}$ phase

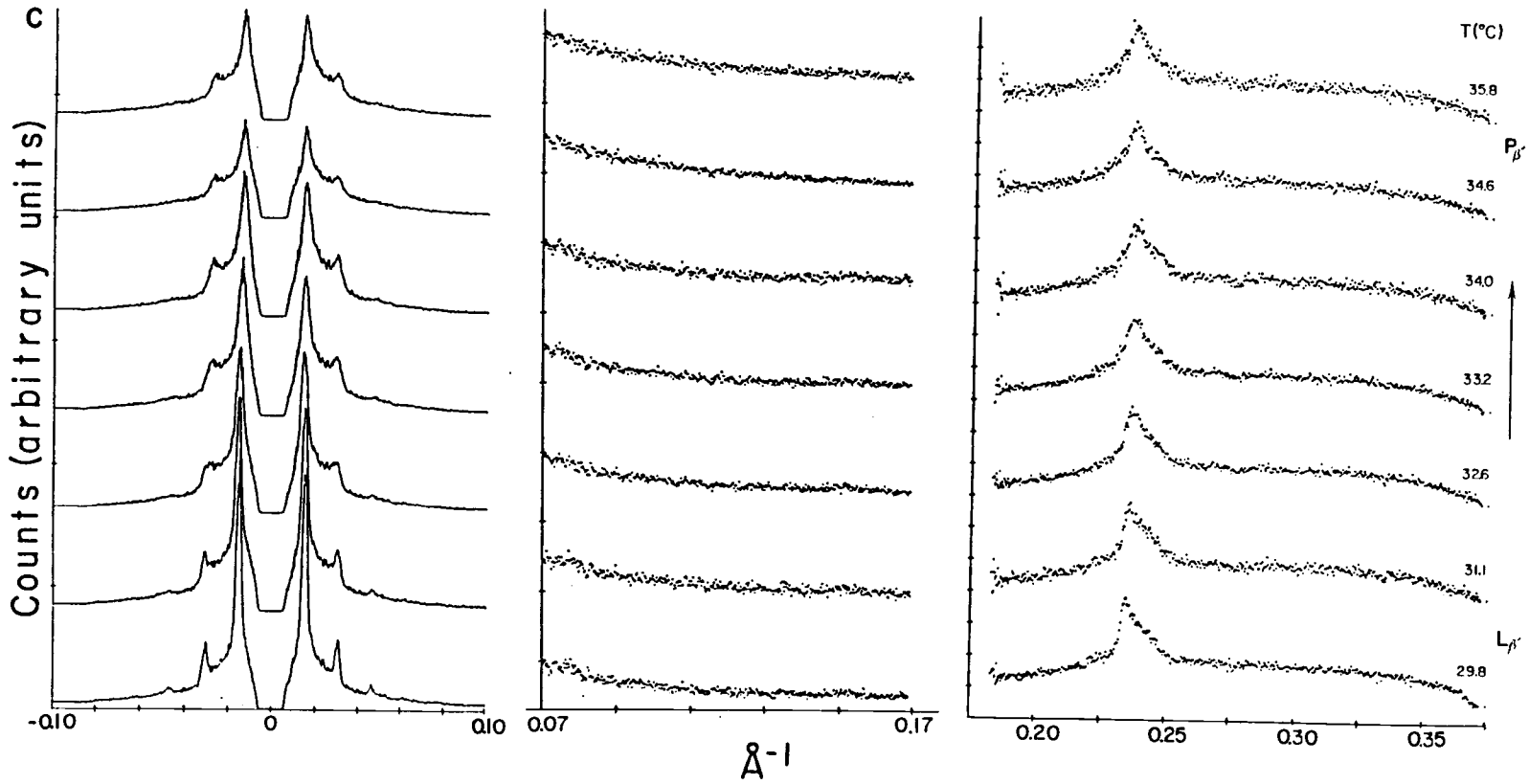

Figure 17 continued: Low-, intermediate- and wide-angle diffraction patterns from MLVs of DPPC in excess H_2O as a function of temperature. c) gel $L_{\beta'}$ to rippled $P_{\beta'}$ phase

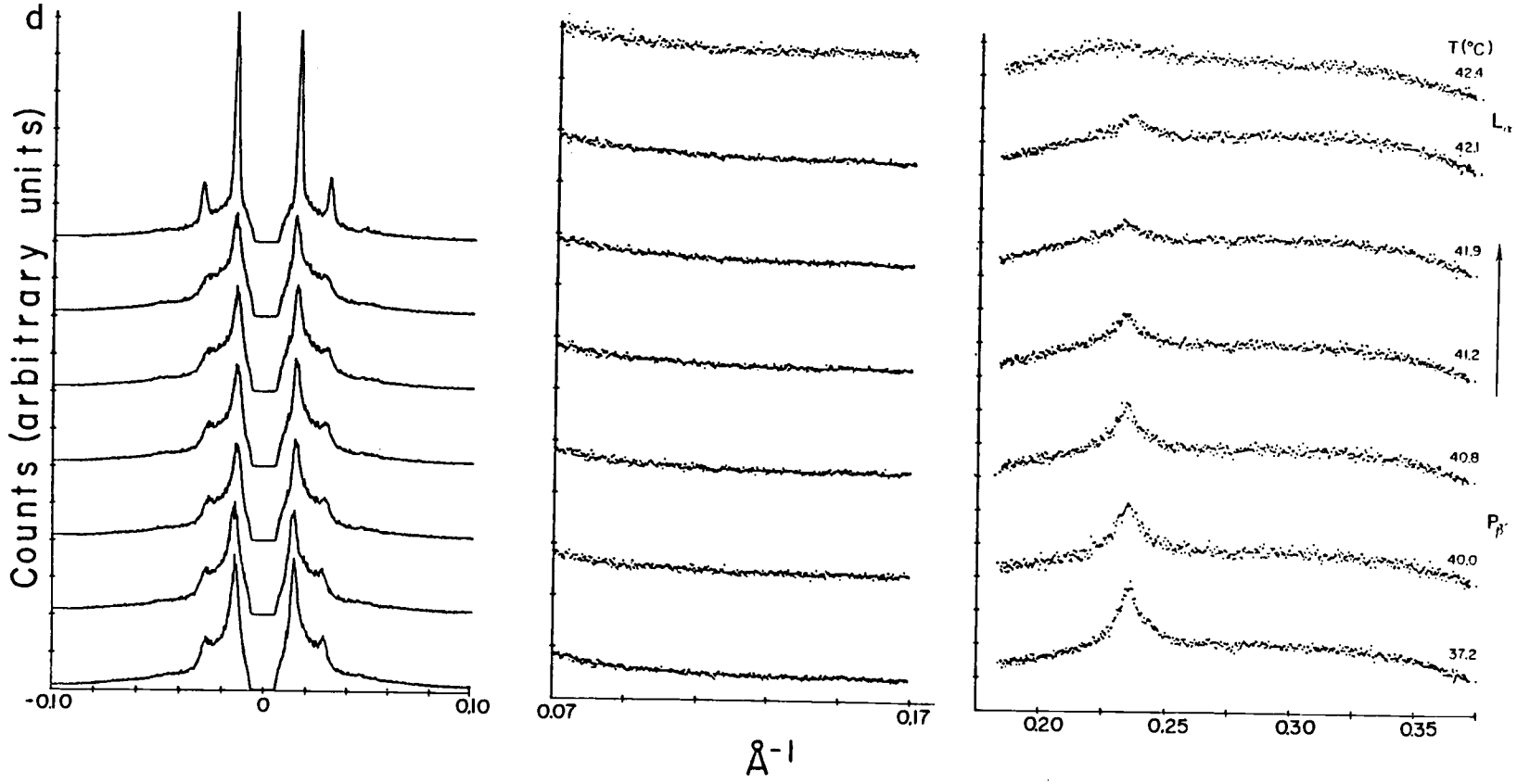

Figure 17 continued: Low-, intermediate- and wide-angle diffraction patterns from MLVs of DPPC in excess H_2O as a function of temperature. d) rippled $P_{\beta'}$ to liquid crystalline L_α phases

TABLE 2

Observed and calculated bilayer parameters for MLVs of DPPC in excess H2O

Phase	$L_{c'}$	$L_{\beta'}$	$P_{\beta'}$	L_{α}
d (Å) (001)	59.5	64.4	71.2	67.0
(02)	10.0	6.55	6.63	6.87
(21)	9.39	---	---	---
(03)/(31)	6.61	---	---	---
(13)	6.39	---	---	---
(2′0′)	4.44	4.22	4.20	4.33
(1′2′)	3.86	4.11	---	---
a_1	21.26	7.56	7.66	7.93
b_1	20.00	13.10	13.26	13.74
a_c	8.88	9.41	9.70	10.00
b_c	8.58	8.44	8.40	8.66
A_1 (Å^2)	53.15	49.54	50.79	54.48
A_c (Å^2)	19.05	19.86	20.37	21.65
Φ (°)	44.21	36.70	36.67	37.37
V_1 (Å^3)	1103	1145	1166	1225
V_x (Å^3)	1581	1595	1808	1825
d_1°(Å)	57.90	57.65	57.24	56.58
d_1 (Å)	41.51	46.22	45.91	44.95
d_{pp} (Å)	40.07	41.77	42.04	39.21
d_1-d_{pp} (Å)	1.44	4.45	3.87	5.74
d_w (Å)	17.99	18.18	25.29	22.03
n_w (mol/mol)	15.99	15.06	21.48	20.07
wt% H_2O	28.18	26.97	34.50	32.98
T_c (°C)	13.5	33.5	41.5	
ΔT_c (°C)	2.3	2.1	0.8	

d = lamellar repeat distance
$A_1 = a_1 b_1 / n_1$; n_1 = no. lipids per cell
$A_c = a_c b_c / n_c$; n_c = no. chains per cell
$\Phi = \cos^{-1}(2A_c/A_1)$
V_1 = molecular volume of lipid from Nagle [87,88]
$V_x = A_1 d$ = volume of one lipid molecule & associated H_2Os
$d1° = V_1/A_c$
$d_1 = d_1° \cos\Phi$
d_{pp} = peak-to-peak distance of electron density profile
dw = d-dl
$nw = dw\ A_1/2Vw = (V_x - V_1)/V_w$; nw = mol H_2O/mol lipid
Vw = 29.9Å^3 (volume of one molecule of water)

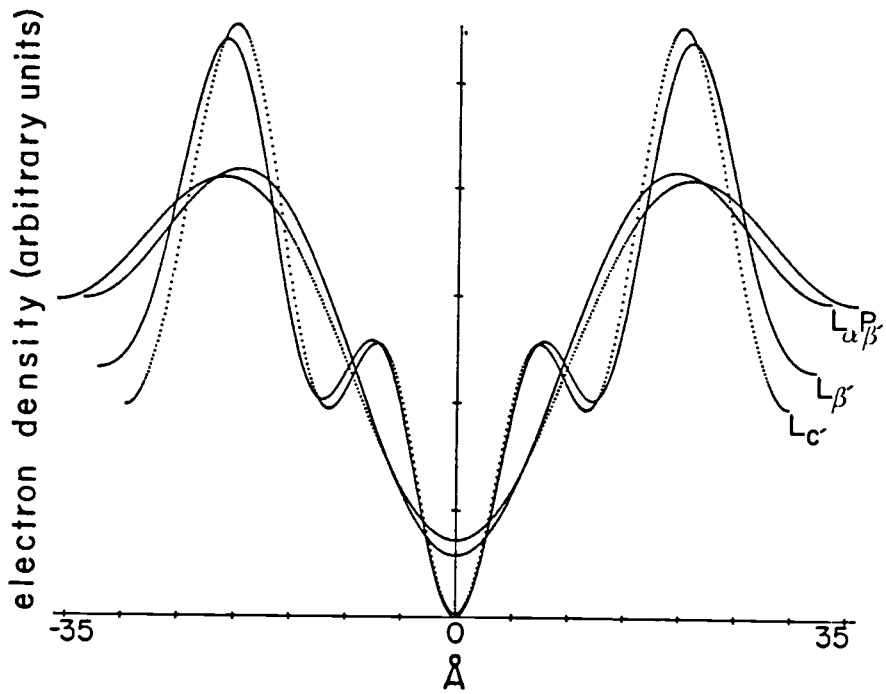

Figure 18: Projected electron density profiles of bilayers of DPPC in excess H_2O. Profiles were generated from data in Table 3.

TABLE 3

Relative intensities for MLVs of DPPC in excess H_2O

Phase	T (°C) d (Å)	Order h	Intensity I_h	Relative Intensity $(h^2 I_h / I_1)^{1/2}$
$L_{c'}$	-0.5	1	12.55	-1.00
	59.5	2	1.81	+0.76
		3	0.51	-0.60
		4	0.33	-0.65
		5	0.05	-0.32
$L_{\beta'}$	24.1	1	12.89	-1.00
	64.4	2	2.61	+0.90
		3	0.43	-0.55
		4	0.20	-0.50
		5	0.12	-0.48
$P_{\beta'}$	35.8	1	9.70	-1.00
	71.8°C	2	2.20	+0.95
L_{α}	43.7	1	12.28	-1.00
	67.0	2	2.73	+0.94

and (1′2′) reflections, with the primes indicating that the indices are associated with the side chains. Then a_c is 8.88Å, b_c is 8.58Å and the area per chain A_c is 19.05Å^2.

In previous works [82,83,86,89], the (1/10.1)Å^{-1} and (1/9.06)Å^{-1} peaks in the intermediate region of the diffraction pattern from subgel DPPC have been indexed as the (10) and (01) reflections from a primitive rectangular cell with two lipid molecules per cell. Analysis based on these assignments leads to A_l = ~46Å^2 and n_w = ~10, representing a decrease in area and a decrease in hydration level relative to the higher-temperature phases, as discussed below. The basis of the assignment to a primitive rectangular cell was the close match between prominent higher-order calculated and observed reflections, with the molecules treated as cylinders in an orthorhombic cell.

However, this analysis, which will be referred to as Case 1, is not unique in producing a match between the major observed reflections and their calculated values. The validity of the assignments is suspect for several reasons:

1) At high statistics, additional small reflections are observable which cannot be accounted for with the Case 1 analysis.

2) In the Case 1 analysis, the area per lipid and the hydration level are lower in the subgel phase than in the gel phase. However, as the sample is annealed from the gel to the subgel phase, the (01) reflection shifts toward lower angles, reaching a limiting value of (1/9.4)Å^{-1}, while the (10) reflection remains virtually constant at (1/10.0)Å-1. Since the area per molecule is directly proportional to the product of the two axes if the cell is rectangular, this is a trend toward larger areas and hydration levels as the sample is annealed. In fact, as the sample is warmed through the subgel phase to the subtransition, the trend is reversed, representing a gradual change to smaller areas and lower hydration levels as the gel phase is approached. This is contradictory to the result that the area and hydration are lower in the subgel than in the gel phase.

3) The peak-to-peak distance d_{pp} in the subgel phase is smaller than that in the gel phase. The smaller value suggests that the thickness of the hydrocarbon region decreases in the subgel phase,

which in turn implies a larger tilt angle and higher hydration [34].

These contradictions are removed if the reflections can be correlated with a larger molecular area. In the analysis of the sidechain packing, the two nearby peaks in the wide-angle region are assumed to indicate a centered rectangular plane lattice. This same approach can be applied to the intermediate region to analyze the headgroup packing. The peaks at $(10.0)Å^{-1}$ and $(9.39)Å^{-1}$ are then indexed as the (02) and (21) reflections from a centered rectangular cell, so that a_1 is 21.27Å, b_1 is 20.00Å and the area per headgroup A_1 is $53.15Å^2$. This analysis will be referred to as Case 2.

To determine the width of the lipid portion of the bilayer d_1, the length of the molecule in the absence of tilt $d_1°$ must be known. Using $A_c = 19.05Å^2$ and $V_1 = 1103Å^3$ [88] in Equation (33), this parameter, which is independent of the headgroup packing, is 57.90Å.

In Case 1, using Equations (32) and (34), Φ is 33.7° and d_1 is 48Å, which is 7Å longer than d_{pp}. A difference of this magnitude does not negate the validity of the assignments, since the relationship between the two parameters in unknown in most cases. However, labelling studies using neutron diffraction have determined the end-to-end distances in the gel phase at less than full hydration levels [90]. In the gel phase at 25wt% H_2O, this distance was 48.8Å; at 5wt% H_2O, the value increased to 50Å.

The dependence of the position of the high-density peak on the number of orders used to calculate the electron density profile has also been determined [91]; the more orders used, the closer the peaks to the ends of the headgroup region. With only five orders, as observed in the subgel phase, a discrepancy between d_1 and d_{pp} is expected, and a difference of up to 10Å is not physically unreasonable. However, Inoko and Mitsui, comparing the value of d_1 calculated from density and volume measurements with d_{pp} from the electron density profiles [96], observed a difference of only 4Å at 5°C in the gel phase, so the discrepancy need not be large. The relationship of d_1 and d_{pp} alone is insufficient to negate the invalidate either Case 1 or Case 2, since definitive studies are not available for the subgel phase.

For comparison, the bilayer parameters can be calculated using the

TABLE 4

Calculated and observed indexed reflections of DPPC subgel phase. Indexing is based on centered rectangular plane lattices in both the headgroup and sidechain regions.

s_1^{-1} = 10.00Å a_1 = 21.26Å $s_1'^{-1}$ = 4.44Å a_c = 8.88Å
s_2-1 = 9.39Å b_1 = 20.00Å $s_2'^{-1}$ = 3.86Å b_c = 8.58Å

	Reflections			Reflections	
Index	Calculated	Observed	Index	Calculated	Observed
10	21.26		33	4.86	
01	20.00		42	4.70	4.70
11	14.57		24	4.52	4.54
20	10.64	10.71	2′0′	4.44	4.44
02	10.00	10.00	0′2′	4.29	4.24
21	9.39	9.39	50	4.25	
12	9.05		51	4.16	4.16
1′0′	8.88		43	4.16	
0′1′	8.58	8.54	2′2′	4.09	
30	7.09		34	4.09	
31	6.68	6.76	05	4.00	4.01
03	6.67	6.61	2′1′	3.94	3.94
13	6.36	6.39	15	3.93	
1′1′	6.17	6.15	52	3.91	3.91
40	5.32	5.2	1′2′	3.86	3.86
41	5.14	5.11	44	3.64	3.64
04	5.00	5.02	53	3.59	
14	4.87		60	3.54	3.53

Case 2 headgroup area. With A_l equal to 53.15Å^2, the cant angle of the side chains Φ is 44.2°. Using this value in Equation (34), the width of the lipid portion of the bilayer d_l is 41.51Å. This differs from the measured peak-to-peak distance from the corresponding electron density profile by only 1.44Å, suggesting a tightly-folded headgroup, if Case 2 is valid.

Under the Case 2 assumption, the thickness of the water region between bilayers d_w, calculated from Equation (35), is similar to that in the gel phase, but the number of water molecules n_w associated with each lipid is larger by 1 because of the larger area A_l.

The new assignments of the peaks at intermediate angles of the diffraction spectrum account for all the peaks which appear in the intermediate- and wide-angle regions. This supports the Case 2 assumption, since the Case 1 assumption does not account for all reflections observed. The calculated and observed reflections based on the new assignments are listed in Table 4.

Subtransition T_s

Figure 17 shows the sequence of diffraction patterns as the temperature is raised through the subtransition. In Figure 19, the positions of the reflections are plotted as a function of temperature. Figure 20 shows the temperature dependence of the background-corrected intensities of the reflections. These figures show that the transition to the gel phase occurs over a temperature range of several degrees.

As noted by Ruocco and Shipley [83], as the sample is cooled, the positions of the wide-angle reflections typical of the gel phase shift gradually until the limiting values characteristic of the crystal phase are reached. This agrees with our observations. However, on raising the temperature through the subtransition, the reverse process does not occur. In the wide-angle region, the gel-phase peaks emerge and coexist with the peaks from the subgel phase. As the intensities of the gel-phase peaks increase, those of the subgel phase decrease, as seen in Figure 20. In addition, the relative intensity of the 1/4.44 Å^{-1} peak begins to decrease rapidly at a lower temperature (~10°C) than that at which the long spacing begins to change significantly (~12-14°C). Although the lamellar repeat distance increases gradually

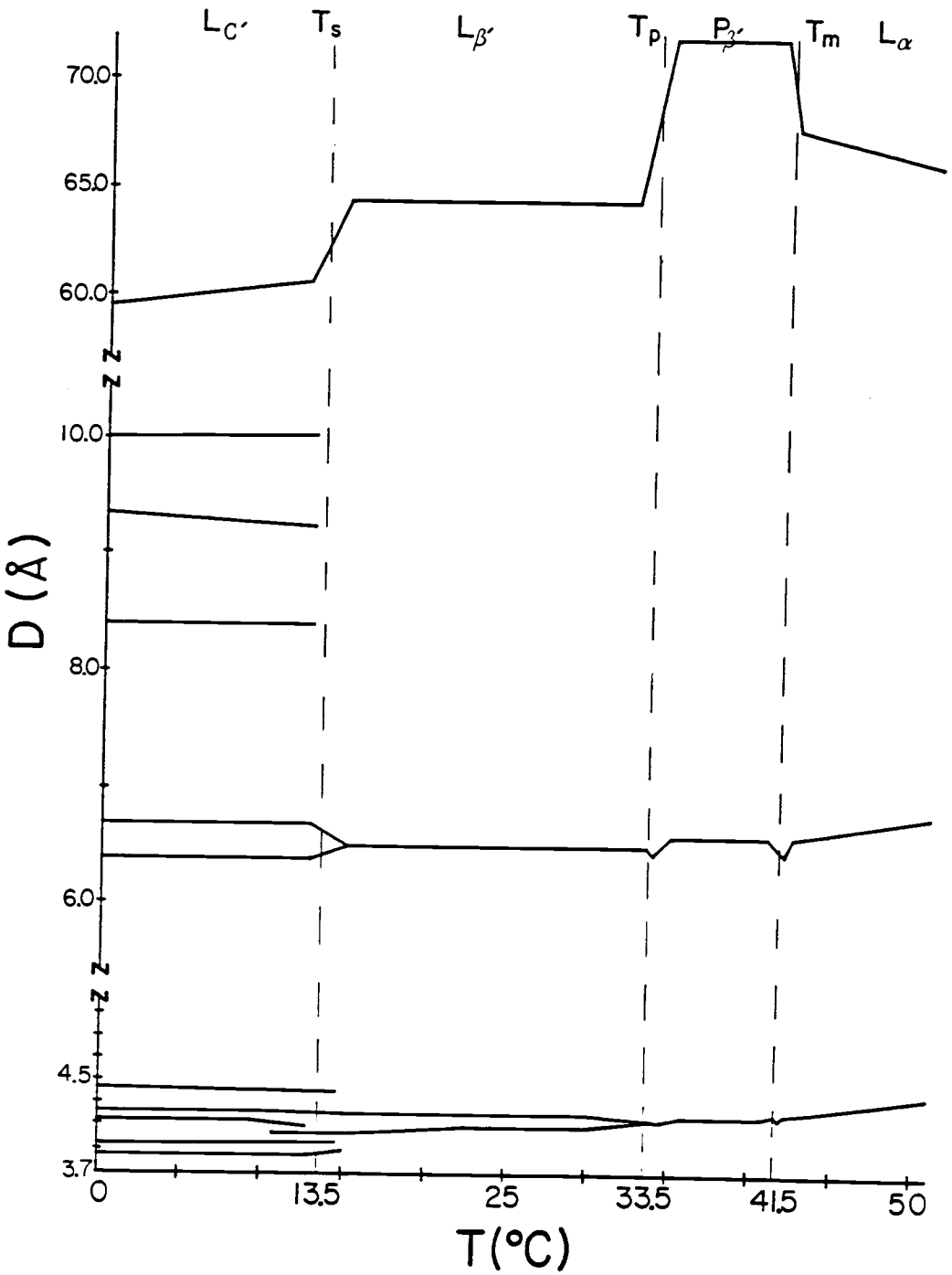

Figure 19: Temperature dependence of peak positions in diffraction patterns from MLVs of DPPC in excess H_2O

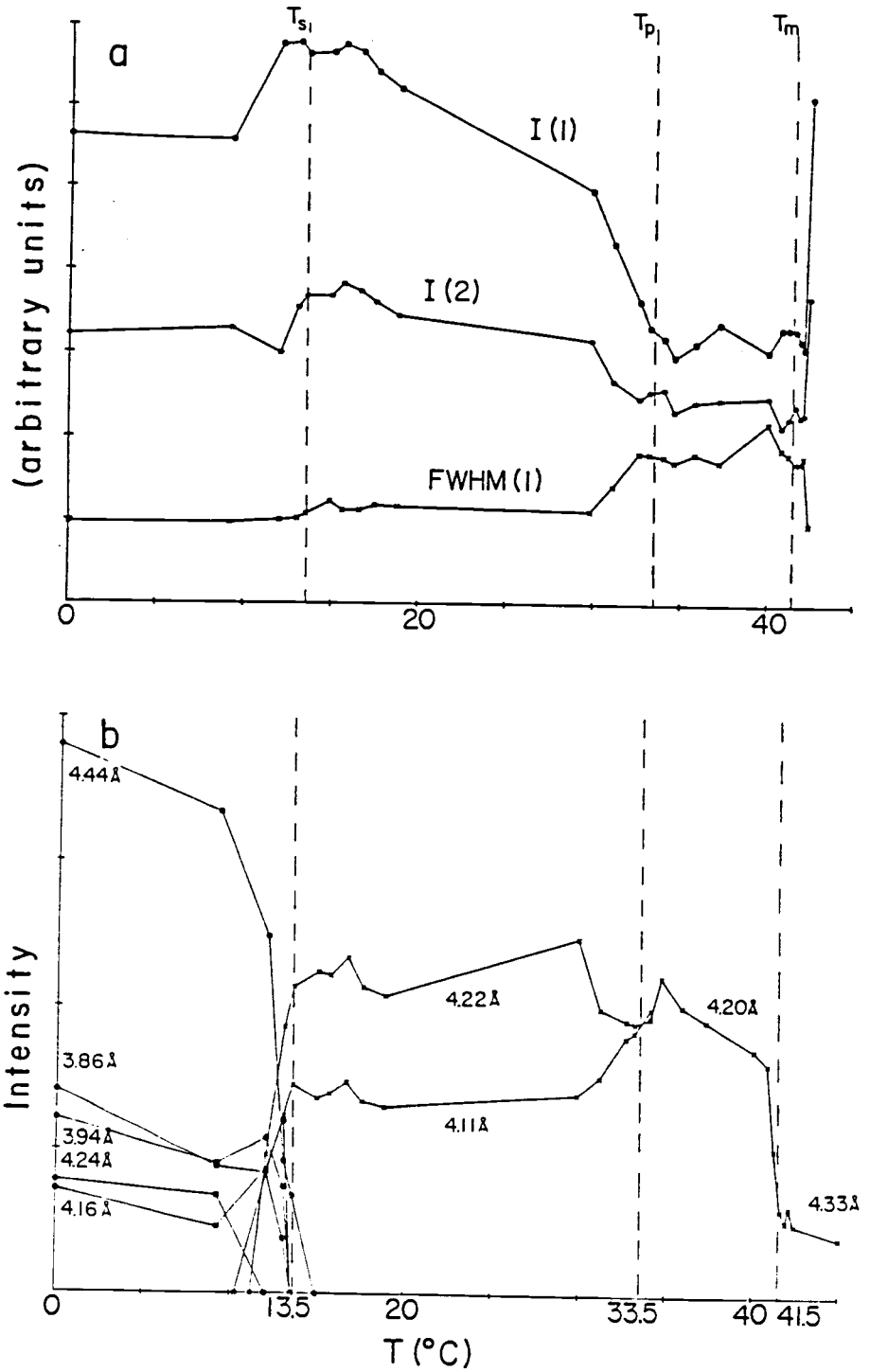

Figure 20: Variation in peak intensities as a function of temperature. a) the intensity of the first-order I(1) and second-order I(2) low-angle reflections and in the full-width half-maximum FWHM(1) of the first-order peak and b) in the intensities of the wide-angle reflections from MLVs of DPPC in excess H_2O as a function of temperature.

through the subgel phase, the low-angle diffraction pattern shows no evidence that the subgel and gel phases coexist. This suggests that the sidechain configurations may play an important role in the subtransition, in support of the findings of Finegold and Singer [92]. They observed subgel phases both in DPPC and in the diheptadecyl analog, but not in an equimolar mixture of the two. In contrast, Casal and coworkers [93] found no evidence in the infrared spectra of deuterated derivatives of DPPC that the acyl chains played any major role in the subtransition. This discrepancy in interpretation of the role of the side chains in subgel formation is an example of the ambiguities which arise in attempts to describe the phase behavior of lipids.

The gradual change in the repeat distance and the gradual decrease in the length of the a_1-axis (shrinking the unit cell area to almost square) as the temperature is raised through the subgel phase indicates a gradual decrease in tilt angle and decrease in hydration as the transition temperature is approached. The relative constancy of the wide-angle peak positions suggests that the sidechain packing mode remains unchanged until the transition temperature is reached.

Planar gel phase $L_{\beta'}$

By 15°C, the conversion from the subgel to the planar gel phase is complete. The repeat distance, which has stabilized at 64.4Å, remains constant as the temperature is increased through the range of the gel phase to the onset of the pretransition (~32°C).

The analysis applied to the subgel phase can be extended to interpret the gel phases if information regarding headgroup arrangement is available. In fact, there is a clue in the diffraction spectrum. In the subgel phase, the ~6.7Å and ~6.4Å peaks were indexed as the (31) and (13) reflections from the two-dimensional unit subcell describing the headgroup in-plane ordering. As the transition to the gel phase progresses, these two peaks coalesce to a weak and broad peak at ~6.6Å. That this peak is directly related to the subgel peaks from which it originates is a logical assumption, so it must reflect headgroup ordering. The appearance of a single peak, rather than two, suggests hexagonal packing, with all the distances between molecules equal.

This distance, which represents the second dimension in the packing parameters (the observed reflection represents the first dimension), is calculated using the same analysis as in the subgel phase. An unambiguous headgroup area can thus be obtained and the remaining parameters calculated. With the $(1/6.55)\text{Å}^{-1}$ peak attributed to hexagonal packing, an area of 49.45Å^2 per molecule is obtained.

In the wide angle region, two peaks are present, a sharp peak at $(1/4.22)\text{Å}^{-1}$ and a broader peak at $(1/4.11)\text{Å}^{-1}$. The intensities of both are lower than that of the major peak in the subgel phase. This pattern derives from side chains tilted 36.7° arranged in a distorted hexagonal lattice, with four molecules at a distance of 4.83Å and two at distance of 4.71Å from the central molecule. The observed peaks can be indexed as the (2′0′) and (1′2′) reflections from a rectangular lattice with a_c = 8.44Å and b_c = 9.41Å. The area per side chain A_c is 19.86Å^2. Using these parameters to calculate d_1 yields a value of 46.22Å, which is somewhat smaller (<3Å) than the end-to-end distance measured by Büldt [94] using neutron diffraction in samples at lower hydration. Since a lower hydration is associated with a smaller chain tilt and longer effective length of the molecules, this difference is expected.

Starting at the midpoint of the subtransition, wide-angle reflections from both the subgel and gel phase coexist, so bilayer parameters for each phase during the transition can be calculated. At the transition midpoint, the hydration levels in both phases is 15.3, indicating an energetic equivalence of the two packing modes at the transition. As the temperature is raised to 25°C, the positions of the wide-angle peaks shift in such a way that the sidechain area increases. The length of a_c gradually increases from an initial value of 9.24Å at the onset of the subtransition to its limiting value of 9.41Å at ~25°. In contrast, the position of the peak from the headgroup order remains constant throughout the range of the gel phase. With the area per head group and the lamellar repeat distance held constant while the area per side chain increases, the hydration level gradually decreases to a minimum value of 15.1 at T ~ 25°C, remaining constant up to T ~ 30°C. By direct measurements of d and water content, Janiak and coworkers [50,95] also observed a decrease in the hydration level, accompanied by

a decrease in tilt angle, as the temperature is raised through the $L_{\beta'}$ phase. They determined a limiting value of 15 water molecules, eleven of which are tightly bound to the head group [35]. It seems unlikely that these tightly bound water molecules would be released at the lower temperatures of the subgel phase.

Pretransition T_p

In the transition from the lamellar gel ($L_{\beta'}$) to the rippled ($P_{\beta'}$) phase, the lamellar repeat distance begins to increase at ~32°C and continues to increase through the transition region, which reaches completion at ~34.5°C. As seen in Figure 17 and quantified in Figure 20, the shape of the low-angle peaks begins to change at the onset of the transition (~31°) to the rippled phase. The peaks begin to broaden and remain broad until the transformation to the fluid phase is complete (42.2°C). Conversely, the heights of the peaks decrease relative to the background, while the total intensities of the peak are only slightly decreased from those in the gel phase. These changes in the shapes of the peaks may reflect the broader distribution of values for the lamellar spacing resulting from the rippling.

As the temperature is raised from ~30°C, the two wide-angle peaks coalesce and the intensities become more equal, as the hexagonal packing becomes less and less distorted. At ~34.5°C, the resulting single peak at $(1/4.16)Å^{-1}$ is at a maximum intensity and the side chains are packed in a regular hexagonal array in which each chain is surrounded by six other chains, each at a distance of 4.80Å from the reference chain. When the temperature is raised further, the peak again shifts to $(1/4.20)Å^{-1}$, maintaining the hexagonal packing.

Rippled gel phase $P_{\beta'}$

A wide range of values for the lamellar repeat distance (66-77Å) have been reported for the fully hydrated rippled phase [48,50,96-98]. Albon [78] has suggested that two separate phases are involved. The average value observed in this laboratory was 71.2 ± 1.4Å. Higher resolution x-ray studies and freeze-fracture work in other laboratories have determined the amplitude of rippling to be 15Å to 25Å [99] and the periodicity to be 100-300Å [34,50], with a width of up to 1000 Å [98].

The wide-angle diffraction in the rippled phase is characterized by a single peak at $(1/4.20)Å^{-1}$. This type of diffraction is characteristic of that from hexagonal packing in which the chains are separated by 4.83Å, with an area per chain of $20.37Å^2$.

As the temperature is raised through the range of the rippled phase, the value of the wide-angle peak remains fairly constant, but the intensity decreases gradually, possibly indicating the increasing presence of gauche conformations and kinks in the side chains. Gaber and coworkers [100], using Raman difference spectroscopy with deuterated lipids, obtained results at 37°C consistent with the presence of a single hexagonal phase with some gauche conformations (1 or 2) near the ends of the side chains.

Table 2 summarizes the observed parameters for the rippled phase. The area per side chain again agrees closely with the value of Ruocco and Shipley ($20.3Å^2$). The value for d_1 is slightly smaller (45.91Å vs. 47.3Å) than that of Inoko and Mitsui while n_w (21.48 vs. 18.5) and d (71.2Å vs. 69.7Å) are larger. The value for n_w from Inoko and Mitsui was calculated from their data.

Sidechain tilt angle in the rippled phase

The presence or absence of chain tilt in the rippled phase has been a long-standing controversy in lipid studies [47,48,50,96,98, 99,101-103].

The origin of the dispute lies in a misinterpretation of an analysis presented by Tardieu et al. [34]. These workers calculated the wide-angle diffraction patterns which would be observed for untilted cylinders hexagonally packed and for tilted cylinders packed in a distorted hexagonal array. Their calculations showed that diffraction pattern from an array of untilted, hexagonally-packed cylinders would exhibit a single, sharp, symmetric peak while the pattern in the tilted case would consist of two peaks, one sharp and one broad. Comparison of the calculated patterns with the observed gel-phase pattern, which shows one sharp peak above $(1/4.2)Å^{-1}$ and one broad one at higher angles, led them to conclude that the side chains in the L_{β} phases of the straight-chain compounds are tilted and arranged in a distorted hexagonal cell. This conclusion is universally

accepted.

However, based on the analysis by Tardieu et al., many workers, observing a single peak in the wide-angle region of the pattern from the rippled phase, have consequently deduced that there is no tilt in the side chains. The fallacy lies in the assumption that if a single peak appears, then the chains are untilted. In fact, a single peak also appears if tilted sidechains are in a true hexagonal array, in which all the distance between the chains are equal.

A more reliable indicator of tilt is the presence of intensity maxima away from the equatorial axis in the wide-angle region. However, determination of the zero of this axis is ambiguous for unoriented bilayers and the rippled phase is not generally observed in oriented, supported bilayers. In unsupported, oriented bilayers, Alecio et al. [98] did observe a rippled phase, which exhibited off-axis intensity, indicating the presence of tilt in this type of sample.

Although it might be argued that the presence of tilt in the rippled phase of oriented samples does not confirm the presence of tilt in unoriented samples, the presence of tilt can be established based on bilayer parameters obtained by application of the analysis used for the planar phases.

The headgroup area can be determined from the diffraction data. Assigning the weak peak at $(1/6.63)\text{Å}^{-1}$ to the reflection from hexagonal packing from the headgroups, the area per molecule is 50.79Å^2, slightly larger than that in the gel phase. This is somewhat larger than the value calculated from data by Inoko and Mitsui (49.3Å^2) [96], but the hydration level of their rippled phase was lower, so a smaller headgroup area is expected.

The side chains are packed in a regular hexagonal lattice, with an area per chain of 20.37Å^2. If the side chains were untilted, then the area per head group would equal twice the area of a side chain, so that

$$A_l = 2A_c = 40.74\text{Å}^2,$$

considerably smaller than that calculated from the diffraction data and considerably smaller than that in the gel phase, which seems unlikely.

The hydration level implicit in the absence of tilt is unreasonably low. If the side chains were untilted, the width of the lipid portion of the bilayer would be equal to $d_l°$, which is related to

the molecular volume and sidechain area by Equation (33). With V_l equal to 1166Å^3 and A_c equal to 20.37Å^2, $d_l°$ is 57.24Å. Since the lamellar repeat distance is 66-72Å, d_w is 9-15Å. If the headgroup area is just twice the sidechain area, or 40.74Å^2, then n_w is only 6-10, which is about half the values reported in the literature from hydration studies [96,97].

The tilt angle and hydration level can also be determined from the x-ray data. In this case, headgroup area is 50.79Å^2, so the tilt angle, determined by Equation (32), is 36.7°, similar to that in the gel phase and in support of the similarity of molecular parameters observed by Inoko and Mitsui in the two phases [96]. It is commonly accepted that the hydration level and sidechain tilt are correlated: a larger tilt is accompanied by a higher hydration level [34]. Since the maximum hydration level in the rippled phase is significantly higher than that in the gel phase, the change in tilt would be expected to be toward a higher, not lower, value. Furthermore, the rippled phase is observed only in samples hydrated at 20wt% or greater [50]. This hydration level implies the presence and necessity of tilt in the formation of the rippled phase.

The peak-to-peak distance d_{pp} from the electron density profiles can be compared to d_l to examine the validity of the assertion that the chains are untilted. Inoko and Mitsui [96] report d_{pp} to be 43.5Å, while we observe 42.04Å at higher hydration. If the chains were untilted and d_l and $d_l°$ were equivalent (57.24Å), the difference between d_l and d_{pp} would be 14-15Å, compared to a difference of only 4.5Å in the gel phase. If the area per lipid A_l is taken as 50.79Å^2, the difference is reduced to 4Å, more similar to the gel-phase difference.

The presence of tilt has been observed in multilayers, but not in single bilayers [79], suggesting the role of interbilayer headgroup interactions in its induction. The larger headgroup area induced by the interbilayer repulsive interactions is accompanied by increased hydration and tilt.

Thus the evidence for the presence of tilt in the rippled phase is substantial and a long-standing controversy is settled.

Main transition T_m

As seen in Figure 20, the intensity of the wide-angle peak begins to fall rapidly at ~41°C, signalling the onset of the main transition, from the rippled to the liquid crystalline phase. Vestiges of diffraction from the hexagonal phase are in evidence to >42°C. This is in agreement with earlier work by Gottlieb and Eanes [104], who analyzed the low and wide angle x-ray diffraction patterns of DPPC samples at various concentrations of water. They observed the coexistence of the rippled and liquid crystalline phase over a temperature range which varied with concentration.

Fluid phase L_α

By 42.5°C, the transition to the liquid crystalline phase is complete. In this phase, the side chains contain a larger number of gauche bonds and possess a high degree of rotational freedom [100]. Studies using ^2H- and ^{31}P-NMR [105] have shown that the head group also exhibits a high degree of motional freedom.

The wide-angle diffraction pattern shows only a broad band centered at ~$(1/4.33)Å^{-1}$. Assuming hexagonal packing with the chains separated by ~5.00Å, the area per side chain is $21.65Å^2$.

The low-angle spacing is again more ordered, with narrower peaks. The lamellar repeat distance decreases over a narrow temperature range (~0.8°C) from ~71 to ~67Å. As the temperature is increased above the transition temperature, the repeat distance continues to decrease gradually and linearly. Just above the transition, the interlamellar hydration level is about 33wt% in this phase, which is similar to that of the $P_{\beta'}$ phase (~34wt%) and higher than that in the $L_{\beta'}$ phase (~27wt%).

In the diffraction patterns of the liquid crystalline phases, the peaks in the intermediate region which result from molecular ordering are very weak and broad. However, using the peak at $(1/6.87)Å^{-1}$ as the 02 reflection of a hexagonal cell leads to an area per molecule of $~54.48Å^2$, slightly smaller than the value calculated from data in Inoko and Mitsui ($56.8Å^2$). The values in Table 2 are calculated based on the hexagonal assignment of the reflection, but the peak may actually be related to the molecular order in a different way. A second reflection

at lower angles, corresponding to a longer cell axis would increase the area slightly and bring the values of A_l and d_l into agreement with the values reported by Inoko and Mitsui. Our value of d_{pp} agrees with theirs (39Å) and our value of d_l is <2Å shorter than the lipid width obtained from the data of Büldt [90] at lower hydration. The lower value is expected at the lower hydration.

Summary

Comparison of values for parameters calculated from headgroup and sidechain reflections with the known volumes and observed bilayer widths confirms the validity of the method of analysis and of the assignments of the reflections. In this method, the reflections in the intermediate- and wide-angle regions of reciprocal space are converted directly to real space and analyzed geometrically to obtain planar unit cell dimensions for the head groups and the side chains. Using the relationship of the volume and sidechain area to obtain the length of the lipid molecule, the remaining bilayer parameters, including the hydration levels and widths of the lipid and water portions of the bilayer, are calculated. The width of the lipid portion of the bilayer is compared to the peak-to-peak distance from the corresponding electron density profile. Applying the method to fully-hydrated MLVs of DPPC, the following results were obtained:

1) Based on the somewhat large discrepancy between the calculated value for the lipid width in the bilayer (47.84Å) and the peak-to-peak distance in the electron density profile (42.26Å) and on decreases in lipid area, hydration level and sidechain tilt angle as a function of increasing temperature, the peak assignments based on a primitive rectangular subcell for the head groups in the subgel phase of pure DPPC were rejected.

If the reflections in the intermediate region are reassigned to define a centered rectangular subcell, a larger area per molecule is obtained and the calculated lipid width agrees more closely with the width from the electron density profile. In contrast to earlier assertions, the lipid is more hydrated (n_w = 15.2) and the tilt angle of the side chains (Φ = 44.2°) greater in this phase than in the gel phase.

2) Although the gel phase transforms gradually into the subgel phase on annealing at low temperatures, with no defined transition, the reverse process does not occur as the temperature is raised through the subtransition. The subgel and gel phases coexist over a ~2.5° temperature range.

3) The structures of the bilayers in the gel phases have previously been ill-defined because the arrangement of the headgroups was unknown. However, the headgroup arrangement can be determined by analysis of the weak reflections in the $(1/6.5)Å^{-1}$ region of the diffraction pattern. The presence of the single peak in this region indicates hexagonal packing with an area per molecule of $\sim 50Å^2$. The bilayer parameters in both gel phases are very similar, except that the hydration level is much higher in the rippled phase (~21) than in the planar phase (~15).

4) The observed changes in hydration at constant d in the gel phase bring into question the practice of assuming that the hydration limit has been reached solely on the absence of changes in d [83,96]. Without monitoring the headgroup and sidechain packing, the hydration level cannot be assessed.

5) The similarity of parameters in the two gel phases extends to tilt angle. In both phases, the side chains are tilted ~37°. If the chains were untilted in either phase, the bilayer width would be >55Å, but the observed bilayer widths are actually ~10Å shorter than this. This settles the controversy over the presence or absence of tilt in the rippled phase.

6) As indicated by the gradual decrease in the intensity of the wide-angle peak in the rippled phase, the side chains disorder gradually as the temperature is raised toward the main transition temperature. In contrast, both the relative intensities and the values of the peaks from the lamellar order remain fairly constant over the range of the phase and change abruptly at the transition.

7) Some laboratories report a lamellar repeat distance of ~60Å in the liquid crystalline phase, but most report a value 65Å or greater. The lower value may be due to the assignment of the peak at $\sim(1/20)Å^{-1}$ as the third-order reflection, corresponding to a lamellar repeat of ~60Å. However, the first- and second-order reflections

indicate a larger repeat distance of ~67Å. In addition, if the 'third-order peak' at ~(1/20)Å^{-1} is expanded, it appears as a doublet and may be related to the headgroup order.

Discussion

In the subgel phase, in contrast to previous analyses (including our own), the headgroup area, the hydration level and tilt angle are larger than the values observed in the gel phase. The bilayer thickness d_1 is 4.7Å less than that in the gel phase, while the molecular volume is only ~30Å^3 less. If the headgroup areas were the same, the subgel d_1 would be ~1Å less than that of the gel phase. If the area were ~46Å^2 as reported previously, the expected d_1 would be ~50Å. The difference between the subgel- and gel-phase values of d_1 can only be explained by a larger headgroup area in the subgel phase.

The values of the parameters which describe the gel and liquid crystalline phases in Table 2 agree well with those of Ruocco and Shipley [82] and Inoko and Mitsui [96]. A discrepancy in hydration levels of the rippled phase between the value in Table 2 and the value calculated from the data of Inoko and Mitsui is attributable to the discrepancy in repeat distances d (71.9Å vs. 69.7Å). Albon [78] also reports a lower value for d (66Å) and lower hydration, but Janiak et al. [50] report a d of 70Å. Albon suggests that two different packing modes may be allowed in this phase. In addition, using the distance between charged groups in a given molecule (4.68Å) and the dimensions of the head group when the oxygen atoms are tilted 30°, he estimates headgroup areas in the gel phases to be either 48Å^2, if one oxygen atom is penetrating the choline sphere, or 51Å^2, if no penetration occurs. The higher value corresponds to the value in Table 2, suggesting that penetration occurs in the planar but not the rippled phase.

Albon also reports an area for the head group in the liquid crystalline phase, but his value seems unreasonably large. If the area is 66Å^2, as he suggests, the expected d_1 would be 2(1225)/66 = 37Å, compared to the observed value of 44.95Å. Since d_{pp} is 39Å, the larger area implies that the peaks in the electron density profile lie outside the molecule.

The parameters in Table 2 yield additional information about the

states of the bilayer in different phases. As the temperature of the sample is raised through each transition, the calculated value for d_1° decreases. This reflects the increasing disorder in each phase and the presence of gauche bonds and kinks in the higher-temperature phases.

The increasing disorder is also reflected in the volume per methylene unit. This can be calculated either from the relation:

$$V(-CH_2-) = 1.23(A_1/2)\cos\Phi, \qquad (39)$$

in which 1.23Å is d for one methylene unit, or from:

$$V(-CH_2-) = 1.23\ A_c. \qquad (40)$$

Use of either expression leads to values for $V(-CH_2-)$ of 23.43, 24.43, 25.04 and 27.49Å^3 in the $L_{c'}$, $L_{\beta'}$, $P_{\beta'}$ and $L\alpha$ phases, respectively, which agree well with values calculated by Nagle and Wilkinson [87]. Including 14 methylene carbons in the hydrocarbon volume V_c and estimating the volumes of a methyl group as 45Å^3 in the subgel phase, 50Å^3 in the gel phases and 55Å in the liquid-crystalline phase, the values of V_c for each of the phases are 746, 784, 801 and 880Å^3 in the $L_{c'}$, $L_{\beta'}$, $P_{\beta'}$ and L_α phases, respectively. Subtracting these volumes from the volume of the lipid V_l results in values of 377, 367, 367 and 345Å^3 for the volumes of the head groups in the $L_{c'}$, $L_{\beta'}$, $P_{\beta'}$ and L_α phases, respectively. These values are in the range of those reported by other workers [32,87,106]. The average of V_c in the planar and rippled phase is equal to the volume reported by Nagle et al. [106] and both V_c and V_h agree with their values in the fluid phase. Expansion in the hydrocarbon region is clearly responsible for the majority of the increase in volume as a function of phase.

The structures of the bilayers of DPPC in all four phases are thus fully described and the effects of small perturbations to this system can be investigated.

STRUCTURAL PARAMETERS OF FULLY HYDRATED BILAYERS OF ISOACYLPHOSPHATIDYLCHOLINES

Intrinsic perturbations

Previous studies on systems of structurally modified lipids have revealed striking differences in their phase behavior compared to that of the parent compound [107-111]. Earlier work in our laboratory showed that the substitution of a single bromine atom for a midchain hydrogen obliterated the gel phase of the lipid [56]. Originally, bromine had been chosen as the midchain substituent to increase the electron density in the center of the bilayer for detection by x-ray diffraction methods. The effect on the phase transition had not been anticipated. However, subsequent monolayer film studies showed a similar phenomenon in bromine-substituted stearic acid: the monolayer film remained in the liquid expanded phase up to the point of collapse [107]. These results led to a further interest in the effects of sidechain modifications on the phase behavior of model membranes.

Modified lipids are also of significant biological interest because lipids with somewhat surprising structures have been found in natural membranes. Some such lipids include cyclohexyl-, cyclopropyl-, iso- and ante-isomethyl-branching in the side chains [112-114]; in other cases, bipolar lipids are formed by isopranyl ether linkages at the midplane of the bilayer [115]. The biological reasons for these modifications and the role they play in the function of the host membranes are not clearly understood.

The methyl-branched lipids are relevant to our work because of the similarity of the molar volume of bromine (27Å^3) to that of a methyl group (23Å^3) [116]. This similarity, coupled with availability, has led to the investigation of the thermotropic phase behavior of two iso-methyl-branched lipids: 1,2-di(15-methyl)hexadecanoylphosphatidyl-choline (17iPC), with an even number of carbons in the length of the side chains, and 1,2-di(18-methyl)nonadecanoylphosphatidylcholine (20iPC), with an odd number. The structures of these two lipids are shown in Figure 3.

As evident in Figure 3, 17iPC is a direct analog of DPPC. Each

side chain is 16 carbons long, with one of the hydrogens at the penultimate carbon (C15) replaced by a methyl group. The methyl substituent is in the area of the bilayer which is characterized, even in the ordered phases, by low density and high fluidity. If substitution were in the midchain region, where sidechain packing is important, the perturbation would be expected to be much greater, especially in the ordered phases. Substitution further along the chain toward the headgroup, as in the brominated lipid previously investigated, introduces the additional possibility that the headgroup configuration might be directly affected. Thus end-chain methyl substitution to the 16-carbon side chain represents a minimal structural modification to the model system.

To investigate the even-odd effect in the structural parameters of the bilayer, a methyl-branched analog with side chains an odd number of carbon atoms in length was necessary. However, in some of the branched-chain compounds, notably both 16iPC and 18iPC (the closest analogs to DPPC), the two transitions coalesce [111], which obviates the characterization of each phase. For this reason, 20iPC, which exhibits transitions which are well-separated and well-defined, was the analog of choice. In this lipid, the number of carbons contributing to the length of the side chains is odd (19).

Even-odd effects have been observed in the physical properties of long chain hydrocarbons. A particular property is not a linear function of the number of carbon atoms in a hydrocarbon chain, but depends on whether an even or odd number of carbon atoms are present. This effect is seen in the alternation in the melting points, but not the boiling points, of alkanes as a function of chain length [117]. The same effect appears in the chain-length dependence of the pretransition temperatures of straight-chain, saturated diacylphosphatidylcholines, but not in the main transition temperature [49]. The branched-chain lipids also exhibit this effect in the temperature dependence of their transitions.

Materials and Methods

The two isobranched lipids 17iPC and 20iPC were synthesized by R. N. A. H. Lewis as described previously [111]. Samples were prepared by

the method used to prepare the pure DPPC samples, but with benzene as the evaporating solvent.

Qualitative Results

Representative diffraction patterns from each phase of the iPCs and the temperature dependence of the spacings are shown in Figures 21-24. In Figure 25, projected electron density profiles for the iPCs in each phase, calculated from the data in Table 5, are presented. Some qualitative aspects of the phase behavior of these lipids are evident from inspection of these figures.

17iPC

This isobranched analog of DPPC exhibits only the subgel, gel and liquid crystalline phases. No rippled phase is observed. Compared to DPPC, the subgel phase is stable to higher temperatures and its main transition temperature is lower, so the range of the gel phase is smaller (~9°C vs. ~20°C) in the methyl-branched species. There is also a well-defined coexistence region that spans ~3°C. In contrast to the behavior of DPPC, this coexistence extends to the lamellar structures from each phase, a evidenced by the double peaks in the low-angle diffraction at 19.5°C (Figure 21a).

The general appearance of the low-angle lamellar diffraction in the subgel phase is similar to that from DPPC, but the wide-angle pattern is characterized by a large number of discrete peaks of low intensity in addition to a single, very sharp peak near $(1/4.5)\text{Å}^{-1}$. The background scattering is low, suggesting a high degree of order. In the gel phase, the wide-angle pattern is qualitatively similar to that of DPPC, but the spacings of the two peaks are more similar to those of the subgel DPPC. In the liquid crystalline phase, the broad wide-angle peak occurs at $\sim(1/4.4)\text{Å}^{-1}$, as in DPPC. Because of the absence of the rippled phase, the lamellar repeat distance increases at the main transitition, despite chain melting.

20iPC

Like the 17iPC, this methyl-branched analog exhibits only the subgel, gel and fluid phases. Both the low- and wide-angle diffraction

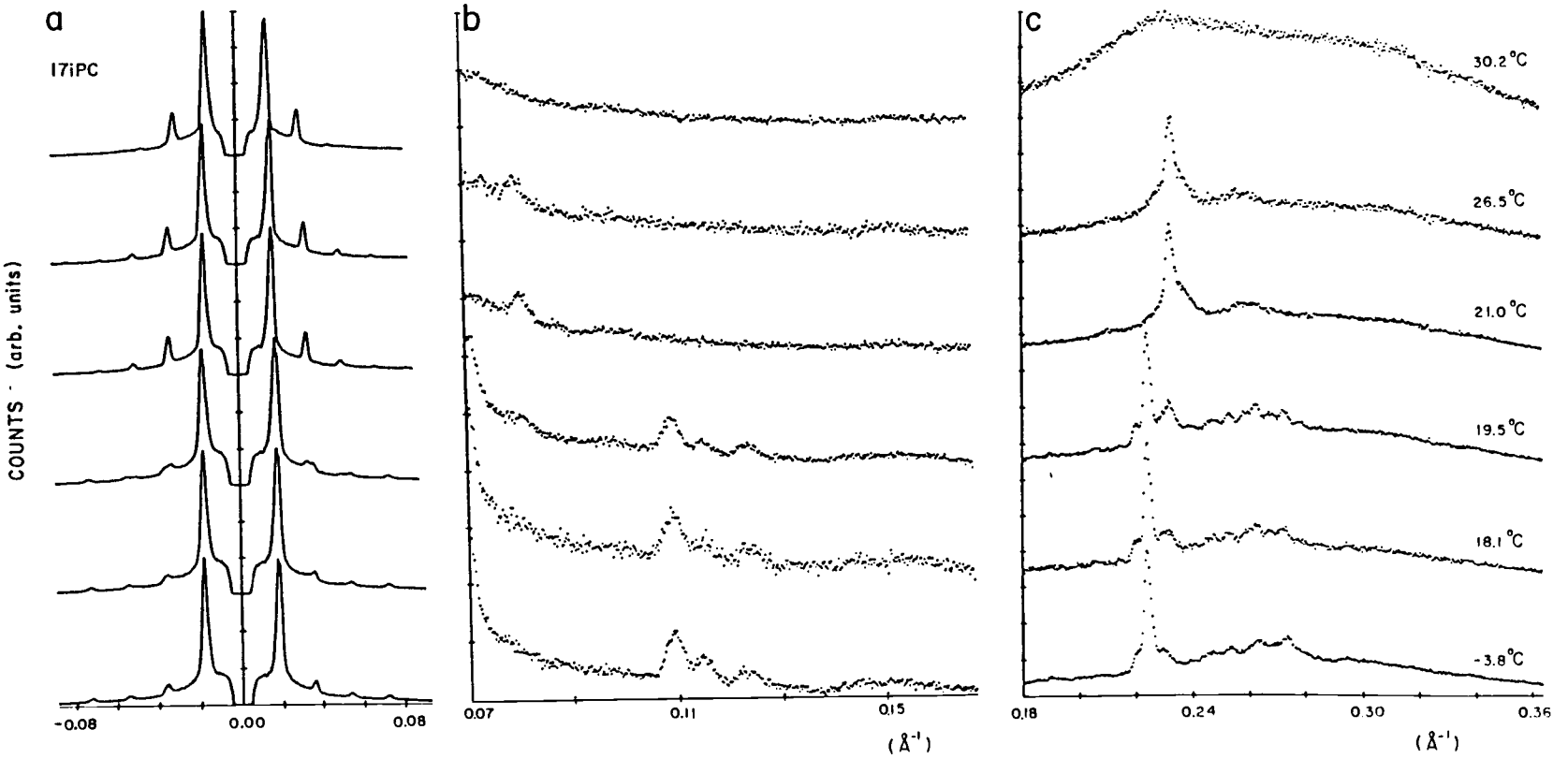

Figure 21: Low-, intermediate- and wide-angle diffraction patterns from MLVs of 17iPC in excess H_2O. Representative patterns from the subgel $L_{c'}$, gel $L_{\beta'}$ and liquid crystalline L_{α} phases at a) low angles, b) intermediate angles and c) wide angles.

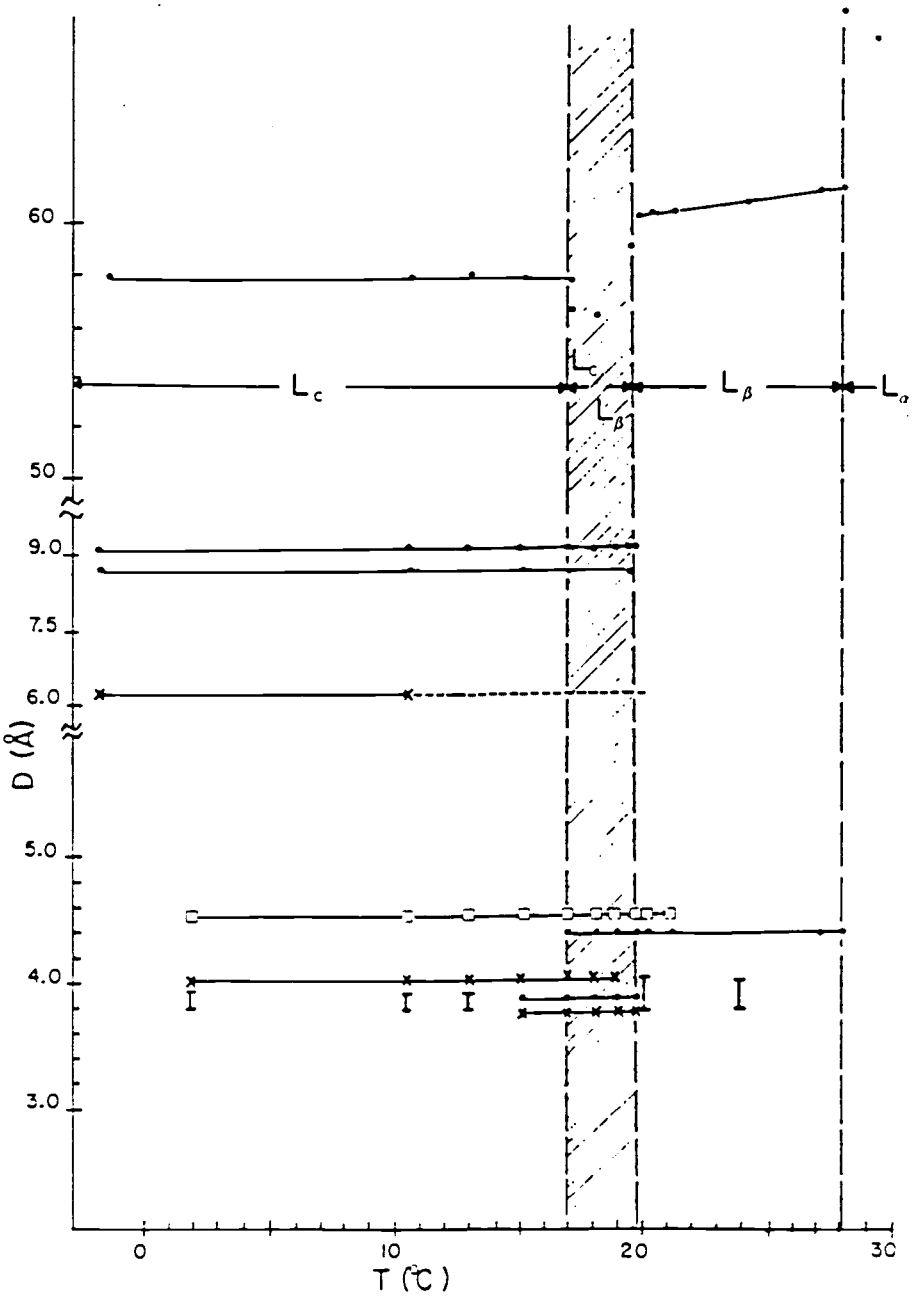

Figure 22: Temperature dependence of spacings in bilayers of 17iPC in excess H_2O

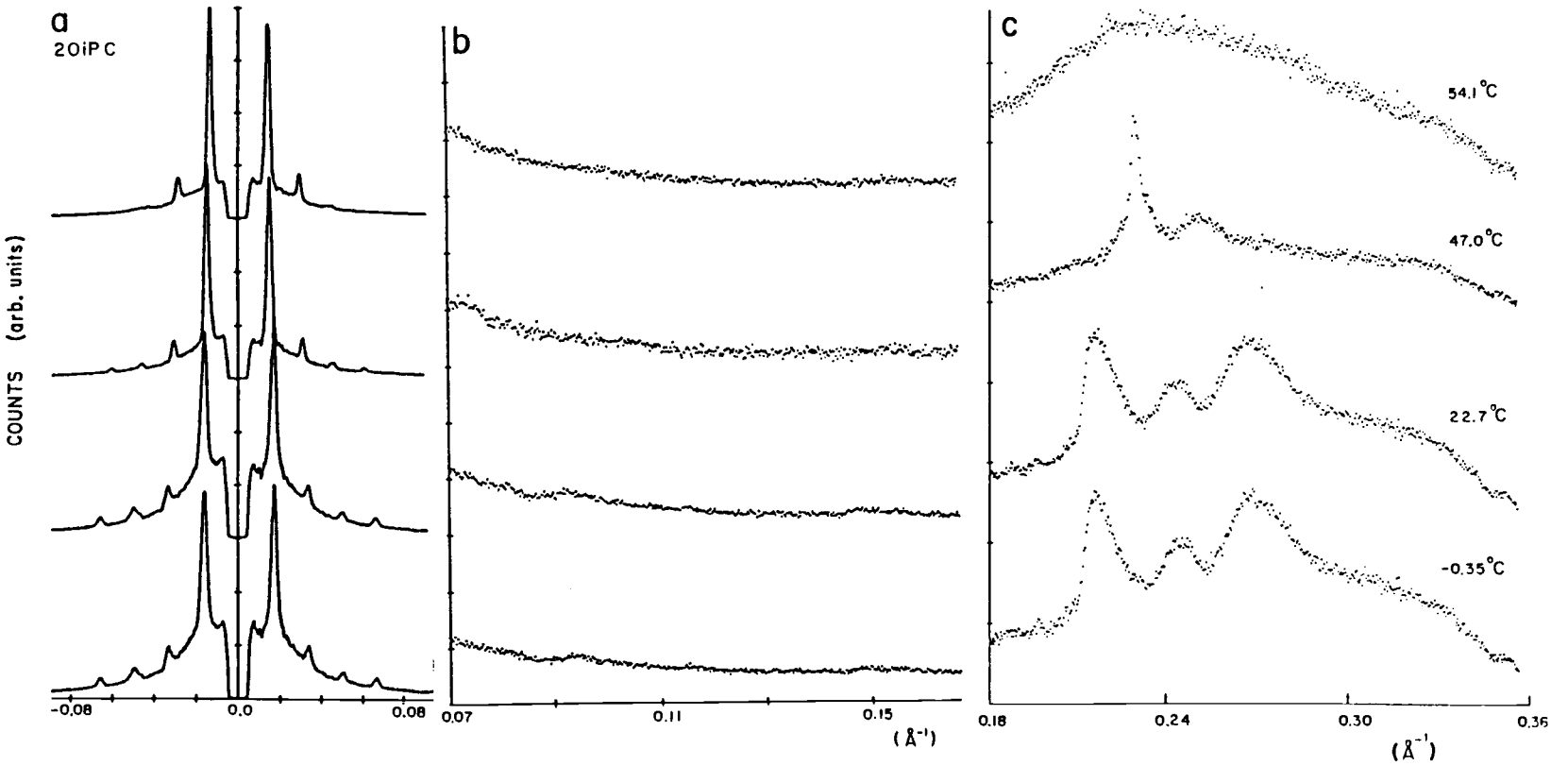

Figure 23: Low-, intermediate- and wide-angle diffraction patterns from MLVs of 20iPC in excess H_2O. Representative patterns from the subgel $L_{c'}$, gel $L_{\beta'}$ and liquid crystalline L_{α} phases at a) low angles, b) intermediate angles and c) wide angles.

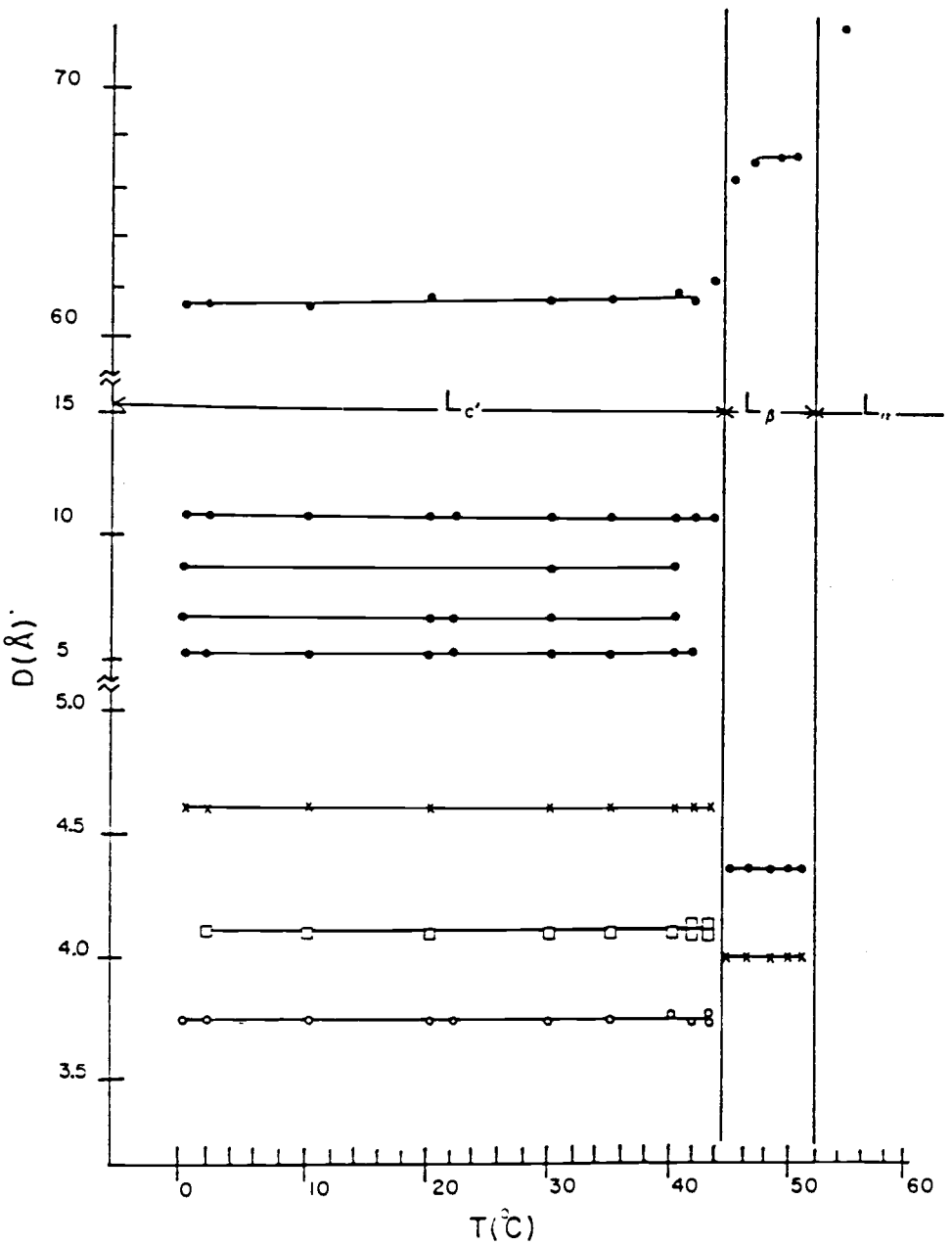

Figure 24: Temperature dependence of spacings in bilayers of 20iPC in excess H_2O

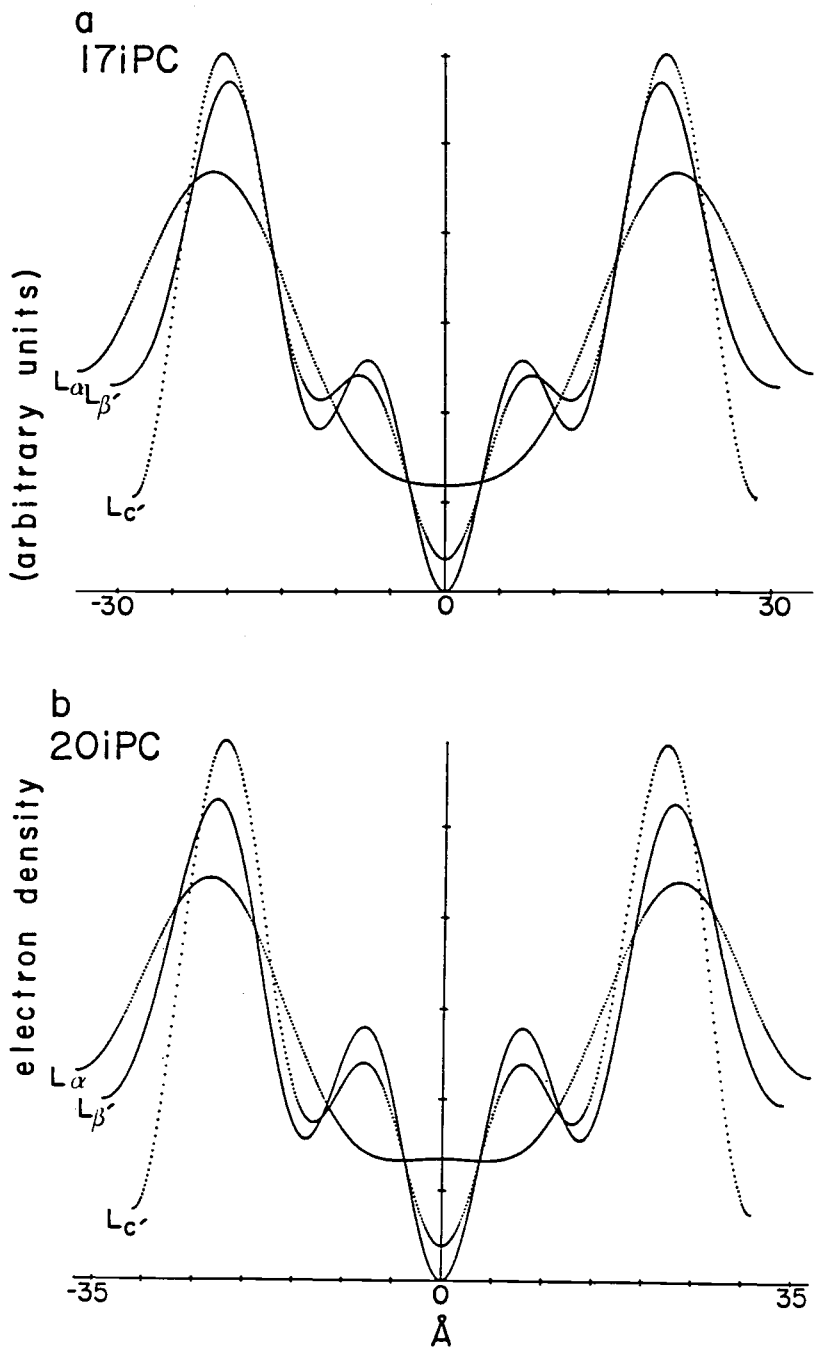

Figure 25: Projected electron density profiles for bilayers of 17iPC and 20iPC in excess H_2O. Profiles from the subgel $L_{c'}$, gel $L_{\beta'}$ and liquid crystalline L_α phases from a) 17iPC and b) 20iPC.

TABLE 5

Relative intensity data for bilayers of 17iPC and 20iPC in excess H_2O

Lipid	Phase T(°C) d(Å)	Order h	Intensity I_h	Relative Intensity $(h^2 I_h / I_1)^{1/2}$
17iPC	$L_{c'}$	1	10.20	-1.00
	-1.6°C	2	1.45	+0.75
	57.25Å	3	0.63	-0.75
		4	0.45	-0.84
	$L\beta'$	1	11.60	-1.00
	24.1°C	2	2.20	+0.87
	61.37Å	3	0.55	-0.65
		4	0.18	-0.50
		5	0.13	-0.53
	$L\alpha$	1	11.65	-1.00
	30.0°C	2	2.55	+0.94
	67.49Å	3	0.28	-0.47
20iPC	Lc'	1	8.10	-1.00
	0.0°C	2	0.92	+0.67
	61.88Å	3	0.65	-0.85
		4	0.53	-1.02
	$L\beta'$	1	10.60	-1.00
	47.2°C	2	1.25	+0.69
	68.17Å	3	0.50	-0.65
		4	0.45	-0.82
		5	0.10	-0.49
	$L\alpha$	1	8.40	-1.00
	54.0°C	2	1.60	-0.87
	73.55Å	3	0.30	-0.57

patterns of 20iPC in the subgel phase are characterized by more background scattering than either DPPC or 17iPC. In addition, the wide-angle pattern is qualitatively different, exhibiting only three broad peaks in this region. In the gel phase, the low- and wide-angle patterns are similar to those of DPPC, including background level, but the peak positions in the wide-angle are comparable to those of the subgel in DPPC. The liquid crystalline phase of 20iPC exhibits a pattern analogous to that of DPPC.

Quantitative Results

Table 6 presents the observed and calculated parameters for the three phases of the iPCs plus those for the analogous phases for DPPC. The parameters for the rippled phase of DPPC have been omitted for clarity and to emphasize similarities between the phases of the three species.

Subgel phases

17iPC

The wide-angle region of the subgel of 17iPC shows one strong, sharp peak at $(1/4.53)Å^{-1}$ and a series of small but well-defined peaks at wider angles. If the strong peak is analyzed as the reflection from hexagonal packing of the side chains, an area per chain of $23.70Å^2$ is obtained. Since the volume of methylene unit in long-chain hydrocarbons in ordered phases is generally less than $25Å^3$, this area would imply a length per methylene unit of only ~1Å, compared to the 1.2 - 1.3Å usually observed [118]. An alternative is that the net plane lattice is square, with $a_c = b_c = 9.06Å$ and $A_c = 20.52Å^2$. This area is somewhat larger than that in DPPC.

The intermediate region of the pattern is characterized by several peaks, four strong peaks at $(1/9.14)Å^{-1}$, $(1/8.73)Å^{-1}$, $(1/8.16)Å^{-1}$, $(1/8.04)Å^{-1}$ and two weak ones at $(1/6.87)Å^{-1}$ and $(1/6.51)Å^{-1}$. The only peak which can reasonably be attributed to lamellar order is the one at $(1/8.16)Å^{-1}$, corresponding to a 7th-order reflection from a repeat of 57.12Å. If the three remaining strong peaks at $(1/9.14)Å^{-1}$, $(1/8.73)Å^{-1}$ and $(1/8.04)Å^{-1}$ are referred to a parallelogram lattice, the area per molecule would be only $44.10Å^2$. To check the validity of the

TABLE 6

Structural parameters of bilayers in MLVs of DPPC, 17iPC and 20iPC in excess H_2O

$L_{c'}$ phase	DPPC			17iPC			20iPC	
d (Å)	59.5			57.2			61.9	
s_1^{-1} (02)	10.0	(20)	8.73	(31)	6.87	(20)	10.9	
s_2^{-1} (21)	9.39	(02)	6.51	(13)	6.51	(02)	10.1	
$s_1'^{-1}$ (2′0′)	4.44	(2′0′)		4.53		(2′0′)	4.62	
$s_2'^{-1}$ (1′2′)	3.86	(0′2′)		4.53		(0′2′)	4.12	
						(2′1′)	3.75	
a_1	21.26		17.46		21.88		21.80	
b_1	20.00		13.02		20.46		20.20	
a_c	8.88			9.06			9.24	
b_c	8.58			9.06			8.70	
A_1 (Å^2)	53.15		56.83		55.96		55.05	
A_c (Å^2)	19.05			20.52			20.10	
Φ (°)	44.21		43.77		42.83		43.10	
V_1(Å^3)	1103			1158			1292	
V_x(Å^3)	1581		1625		1648		1704	
d_1° (Å)	57.90			56.43			62.84	
d_1 (Å)	41.51		40.73		40.18		45.88	
d_{pp} (Å)	40.07		40.70		40.70		44.19	
d_1-d_{pp} (Å)	1.44		0.03		0.68		1.69	
d_w (Å)	17.99		16.47		15.82		16.02	
n_w (mol/mol)	15.99		15.65		14.80		14.75	
wt% H_2O	28.18		26.99		25.91		23.88	
T_c (°C)	13.5			18.2			44.0	
ΔT_c (°C)	2.3			2.5			2.5	
$L_{\beta'}$ phase								
d (Å)	64.4			61.0			67.2	
s^{-1} (02)	6.55			6.61			6.82	
$s'_1{}^{-1}$ (2′0′)	4.22	(2′0′)		4.31		(0′2′)	4.40	
$s'_2{}^{-1}$ (1′2′)	4.11	(0′2′)		4.25		(2′1′)	4.02	
		(2′1′)		3.85				
a_1	13.10			13.22			13.64	
b_1	7.56			7.63			7.88	
a_c	9.41			9.20			9.04	
b_c	8.44			8.62			8.80	

TABLE 6 continued

A_1 (Å^2)	49.54	50.43	53.74
A_c (Å^2)	19.86	19.83	19.89
Φ (°)	36.70	38.15	42.25
V_1 (Å^3)	1145	1202	1376
V_x (Å^3)	1595	1538	1806
d_1° (Å)	57.65	60.62	69.18
d1 (Å)	46.22	47.67	51.21
d_{pp} (Å)	41.77	39.67	45.81
d_1-d_{pp} (Å)	4.45	8.00	5.40
d_w (Å)	18.18	13.33	15.99
n_w (mol/mol)	15.05	11.24	14.37
wt% H_2O	26.97	20.98	23.41
T_m (°C)	41.9	28.1	52.0
ΔT_m (°C)	0.8	0.5	---
L_α phase			
d (Å)	67.0	67.0	72.3
s^{-1} (02)	6.87	6.61	6.69
s'^{-1} (0′2′)	4.33	4.36	4.42
a_1	13.74	13.22	13.38
b_1	7.93	7.63	7.72
a_c	10.00	10.06	10.20
b_c	8.66	8.72	8.84
A_1 (Å^2)	54.48	50.45	51.65
A_c (Å^2)	21.65	21.93	22.56
Φ (°)	37.39	29.62	29.12
V_1 (Å^3)	1225	1265	1461
V_x (Å^3)	1825	1690	1867
d_1° (Å)	56.58	57.68	64.76
d_1 (Å)	44.95	50.14	56.58
d_{pp} (Å)	39.21	43.76	47.94
d1-d_{pp} (Å)	5.74	6.38	8.64
d_w (Å)	22.03	16.86	15.72
n_w (mol/mol)	20.07	14.22	13.58
wt% H_2O	32.98	25.14	22.41

assignment, the width of the lipid portion of the bilayer can be calculated and compared to the observed d_{pp}. Since the measured volume of 17iPc in the subgel phase is 1158Å^3 [119], d_l would be 52.52Å, which is ~12Å longer than d_{pp} (40.70Å). Since the difference between d_l and d_{pp} in the subgel phase of DPPC is only ~1.5Å, this assignment is either incorrect or the headgroup configurations differ radically in the two analogs.

A similar discrepancy arises if the peak at (1/9.14)Å^{-1} is attributed to a reflection from a square plane cell or if the peaks at (1/9.14)Å^{-1} and (1/8.73)Å^{-1} are referred to a centered rectangular lattice. Assuming the value of d_l is similar to that of d_{pp}, as in DPPC, and using the known volume and d_{pp}, the value of A_l can be estimated to be ~57Å^2. Any assignment based on any combination of the four strong peaks leads to values of A_l either much too large or much too small. It may be that the strong peaks are low-order reflections from the sidechain subcell, since each corresponds to twice the value of a peak in the wide-angle region. This would imply a subcell with dimensions twice those listed in Table 6. This may result from the asymmetry introduced by the additional methyl group at the ends of the chains.

Two possibilities exist for obtaining a reasonable value for A_l. In analogy to the analysis for DPPC, the two broad peaks at (1/6.87)Å^{-1} and (1/6.51)Å^{-1} can be designated the (31) and (13) reflections, leading to a_l = 21.88Å, b_l = 20.46Å and A_l = 55.96Å^2. This value for A_l is just slightly smaller than the ~57Å^2 estimated from the molecular volume and d_{pp}. However, indexing based on these assignments does not account for the peak at (1/8.73)Å^{-1}, even if the larger sidechain area is used (Table 7). If the peaks are indexed as the (03) and (31) reflections, the peak at (1/9.14)Å^{-1} indexes as the (21) reflection, but the (1/8.73)Å^{-1} peak is still not accounted for. The only other assignments which yield reasonable parameters are the (1/8.73)Å^{-1} peak as the (20) and the (1/6.51)Å^{-1} as the (02) reflections, respectively. This results in primitive rectangular lattice with dimensions a_l = 17.46Å, b_l = 13.02Å and A_l = 56.83Å^2. This indexing does not account for the (1/6.87)Å^{-1} reflection. In either case, Φ is ~43-44° and n_w is ~15-16, similar to the values obtained for DPPC.

TABLE 7

17iPC subgel phase: calculated and observed reflections
comparison of two systems of indexing
reflections and cell parameters of 17iPC subgel phase

$s_1^{-1} = 6.87$ a = 21.88
$s_2^{-1} = 6.51$ b = 20.46
$s_1'^{-1} = 4.53$ a' = 9.06
$s_2'^{-1} = 4.53$ b' = 9.06

$s_1^{-1} = 8.73$ a = 26.19
$s_2^{-1} = 6.51$ b = 19.53
$s_1'^{-1} = 4.53$ a' = 9.06
$s_2'^{-1} = 4.53$ b' = 9.06

Index	Reflections		Index	Reflections	
	Calculated	Observed		Calculated	Observed
10	21.88		10	26.19	
01	20.46		01	19.53	
20	10.94	11.31	20	13.10	12.99
02	10.23	10.34	21	10.88	11.39
21	9.65		02	9.76	10.34
12	9.27		12	9.15	9.14
0'1'	9.06	9.14	1'0'	9.06	9.14
1'0'	9.06	9.14	0'1'	9.06	9.14
22	7.47	7.50	30	8.73	8.73
30	7.29	7.07	31	7.97	8.10
31	6.87	6.87	22	7.83	
03	6.80		40	6.55	6.51
13	6.51	6.51	03	6.51	6.51
1'1'	6.41	6.30	32	6.51	6.51
32	5.94		1'1'	6.41	
23	5.79		13	6.32	6.30
40	5.47		41	6.21	
41	5.28	5.27	42	5.44	
04	5.12		50	5.24	5.27
33	4.98		33	5.22	5.27
14	4.98		51	5.06	
42	4.82	4.81	04	4.88	
24	4.63	4.55	14	4.80	4.81
2'0'	4.53	4.47	43	4.62	
50	4.38	4.37	52	4.62	
51	4.28		24	4.57	4.55
43	4.27		2'0'	4.53	4.47
34	4.19	4.19	60	4.37	4.37
05	4.09		61	4.26	4.19
2'1'	4.05	4.06	34	4.26	4.19
52	4.02	3.95	53	4.08	4.06
15	4.02	3.95	2'1'	4.05	4.06
25	3.83	3.80	62	3.98	3.95
44	3.74	3.80	44	3.91	3.91
			05	3.91	3.91
			15	3.86	3.80

The lamellar repeat distance of 17iPC in the subgel phase is about 2Å smaller than that of DPPC. Based on the parameters calculated from the diffraction pattern, the difference in repeat is not due to a change in sidechain tilt or hydration, but to a change in the effective length of the molecule d_1°. This is likely due in part to the decrease in the average length of the methylene unit consequent to branching and in part to changes in the headgroup configuration. The close agreement between d_1 and d_{pp} may indicate a very tightly folded headgroup, resulting in a shorter effective length for both the head group and the molecule itself.

20iPC

Three broad, strong peaks at $(1/4.62)Å^{-1}$, $(1/4.12)Å^{-1}$ and $(1/3.75)Å^{-1}$ characterize the wide-angle region of the diffraction pattern of 20iPC in the subgel phase. Analysis of these peaks as the (2′0′), (0′2′) and (2′1′) reflections from a parallelogram plane lattice yields an area per side chain $A_c = 20.10Å^2$, similar to that from 17iPC. The actual dimensions of the lattice edges are $a_p = 10.6Å$ and $b_p = 8.70Å$, which are approximately twice the dimensions of the triclinic subcell in the isobranched fatty acid with 19 carbons (17-methyloctadecanoic acid) [118]. However, the area per chain is still determined by b_c and $s_1'^{-1}$, the base and height of the parallelogram, which are 8.70Å and 9.24Å, respectively. For convenience, the a_c and b_c in Table 5 refer to these values, rather than those of the actual cell edges.

The peaks in the intermediate region of the diffraction pattern from 20iPC in the subgel phase are at $(1/10.9)Å^{-1}$, $(1/10.1)Å^{-1}$, $(1/6.74)Å^{-1}$ and $(1/6.44)Å^{-1}$. If these peaks are referred to a primitive rectangular lattice, the area per molecule is $55.05Å_3$, slightly smaller than that in 17iPC in this phase. The tilt of the side chains is then 43.1° and the hydration level 14.8, both comparable to those in 17iPC. Table 8 lists the calculated and observed indexed reflections from subgel 20iPC.

TABLE 8

Calculated and Observed Reflections in Subgel 20iPC

Order	Calculated Value	Observed Value	Order	Calculated Value	Observed Value
10	21.8		33	5.14	
01	21.1		04	5.05	5.07
11	14.8		14	4.92	
20	10.9		42	4.80	
02	10.1		2′0′	4.59	4.62
21	9.59		24	4.58	
1′0′	9.19	10.9	50	4.36	4.37
12	9.16		51	2.26	
0′1′	8.24	9.88	43	4.24	
1′1′	7.43	9.31	34	4.15	
22	7.41		0′2′	4.12	4.12
30	7.27		05	4.04	
31	6.84		1′2′	4.02	
03	6.73	6.74	52	4.00	
13	6.43	6.44	35	3.97	
32	5.90		25	3.79	
23	5.73		2′1′	3.77	3.74
40	5.45		44	3.70	
41	5.26		2′2′	3.72	

Calculated values for the side chains are based on a parallelogram lattice derived from reflections corresponding to 4.62Å, 4.12Å and 3.75Å, with a = 4.85Å and b = 4.35Å, γ = 71.3°. The values for the molecular packing are based on a square lattice, with a = b = 21.80Å.

Gel phases

17iPC and 20iPC

The pattern in the wide-angle region of the gel phase of 17iPC is similar to that of the $L_{\beta'}$ phase in DPPC, but the main peak is sharper and shifted to lower angles. The shoulder which flanks the main peak is diminished in intensity compared to that of the shoulder in DPPC and a third, broad peak appears at wider angles. The diminished intensity of the shoulder and the presence of the broad peak suggest that the lattice is a parallelogram, with cell edges of 4.70Å and 4.60Å and A_c = 19.83Å^2, similar to that in the gel phase of DPPC. Again, the area is determined by $s_1'^{-1}$ and b_c, which are used to determine a_c and b_c in Table 5. If the (1/4.31)Å^{-1} and (1/3.85)Å^{-1} peaks are indexed as the (0′2′) and (2′1′) reflections, a square lattice with $a_c = b_c$ = 8.62Å and A_c = 18.58Å^2 results. This area is smaller than that of 17iPC in the subgel phase and smaller than that of DPPC in the gel phase and is thus suspect. Use of this area and the measured volume (1202Å^3,[119]) to calculate $d_1°$ gives 64.71Å for the length of the extended molecule, which seems unreasonably long. These assignments were therefore rejected in favor of the parallelogram lattice.

The pattern in the intermediate region is very similar to that of DPPC, with only a broad peak at (1/6.61)Å^{-1}. If this peak is indexed on a hexagonal plane lattice, the area per molecule is 50.43Å^2, so the tilt angle $\Phi = \cos^{-1}(2\ 19.83/50.43) = 38.2°$, slightly larger than that observed in DPPC. These parameters lead to a slightly larger d_1 than that of DPPC, although d_{pp} is slightly smaller. An uncurling of the head group may be indicated.

The overall lamellar repeat distance for 17iPC in this phase is lower than that of DPPC because of the lower hydration level and slightly larger tilt angle.

In 20iPC, the lattice net plane for the side chains is centered rectangular, as determined by the reflections at (1/4.40)Å^{-1} and (1.4.02)Å^{-1}. The area per chain is 19.89Å^2, similar to that of DPPC and 17iPC in this phase. The reflection indicating molecular ordering is at lower angles than in the 17iPC, so the area A_1 and tilt angle Φ are larger than in either DPPC or 17iPC. The hydration level, however, is intermediate between that of DPPC and that of 17iPC.

Liquid crystalline phases

17iPC and 20iPC

The wide-angle patterns of both 17iPC and 20iPC in the L_α phase are characterized by a single, very broad, diffuse peak centered at $(1/4.36)Å^{-1}$ and $(1/4.42)Å^{-1}$, respectively, similar to the pattern from DPPC. This indicates hexagonal packing in the net plane, with $21.93Å^2$ (17iPC) and $22.56Å^2$ (20iPC) per chain. The patterns in the intermediate region are also similar to that of DPPC, but the locations of the peaks lead to different molecular areas for DPPC, 17iPC and 20iPC, and therefore different tilt angles.

The molecules in 17iPC are apparently more ordered than DPPC in this phase, as indicated by the longer $d_1°$. The hydration levels in 17iPC and 20iPC are similar (~14 mol H_2O/mol PC).

Summary

This work represents the first detailed analysis of the structures of bilayers of isoacyl phospholipids. Although x-ray data was presented previously, the electron density profiles had not been generated. In addition, the molar volumes have recently become available, so the results from x-ray can now be compared to confirm peak assignments. The present analysis led to the following conclusions.

1) In the subgel phases, the original peak assignments for both 17iPC and 20iPC were referred to primitive rectangular lattices with molecular areas of $39.8Å^2$ in 17iPC and $47.7Å^2$ in 20iPC. Since these molecular areas are small compared to the known volumes of the lipids, the predicted bilayer widths would be large: 58.2Å in 17iPC and 54.2Å in 20iPC. However, the observed peak-to-peak distances are small: 40.70Å in 17iPC and 44.19Å in 20iPC. This led to a reevaluation of the peak assignments to obtain molecular areas compatible with the observed parameters. The new analysis yields hydration levels of ~15 in both 17iPC and 20iPC, in contrast to 0 in 17iPC and 7-8 in 20iPC with the old assignments. The new value is more similar to that observed in subgel DPPC.

2) In the subgel phase of 20iPC, the headgroup plane lattice is rectangular but the sidechain lattice is parallelogram. In 17iPC, the headgroup lattice is either primitive or centered rectangular, while the side chains are arranged in a square lattice. The sidechain areas in both species are larger than that in DPPC, as expected.

3) In the transition to the gel phase of 17iPC, the subgel and gel phase coexist over temperature range of 3°C. Unlike DPPC, the lamellar phases as well as the sidechain states coexist.

4) Neither isobranched lipid exhibits a rippled phase, but the planar gel phase is similar to that of DPPC. In the gel phase, the sidechain lattice for 17iPC is a parallelogram, but that for 20iPC is centered rectangular, more similar to DPPC. The sidechain areas in this phase are similar for all three species.

5) Although the subgel phases in the iPCs are more stable than the subgel phase of DPPC, the gel phases are less stable. The main transition temperature of 17iPC is ~13.5°C lower than that of DPPC.

6) The hydration levels and tilt angles in the fluid phase are lower in the iPCs than in DPPC.

Although the analysis presented above answers many questions concerning the bilayer structures of the two isobranched lipids studied, ambiguities remain. Similar structural studies of other lipids, in particular, the straight-chain analog of 20iPC, might provide a basis for a clearer interpretation of the data presented here.

STRUCTURAL PARAMETERS OF FULLY HYDRATED BILAYERS OF DPPC PLUS BROMOFORM

Extrinsic perturbations

The interaction of bromoform ($CHBr_3$) with model membranes is of interest from several standpoints. First, $CHBr_3$ is a small, lipophilic molecule (molecular volume: ~145Å^3 at room temperature; Hildebrand paramater: 21.5 MPa^{½}) which is expected to dissolve mainly in the hydrocarbon portion of an amphiphilic molecule. Earlier work by Wickman [120] had shown that vapor-phase bromoform was readily taken up by oriented multilayers of a 60:40 mixture of DMPC/cholesterol at room temperature. This result, combined with the continued interest in brominated compounds, led to investigation of the effects different concentrations of bromoform on the structures of the phases in MLVs of DPPC.

Secondly, bromoform can be regarded as a primitive anesthetic [121,122] and information concerning its effects on the structure of a multilamellar system adds to the body of knowledge concerning lipid-anesthetic interactions. Comparison of the effects of bromoform with those of other, more effective halogenated anesthetics, such as chloroform or halothane, may provide insight into the involvement of membrane lipids in the mechanism of anesthesia.

Thirdly, bromoform, as well as other trihalomethanes, is an environmental pollutant produced by the reaction of chlorine with the bromide ion and bromine-containing organic matter which naturally occur in the raw water supply [123-125]. A higher rate of human cancer has been noted in populations using water supplies which contain trihalomethanes than in those whose drinking water is free of them [126]. Thus the interaction of bromoform with lipids is both of environmental and pathological significance. Lipids which have been modified by environmental pollution have been found incorporated into systems in the food chain [127] and their effect may potentially be toxic [128].

Materials and Methods

Dipalmitoylphosphatidylcholine (DPPC) with a stated purity >99%

was purchased from Sigma Chemical Company. It gave one spot with TLC and was used without further purification. Only water filtered in a Millipore "Milli-Q" ultrafiltration system was used for sample preparation. Reagent-grade bromoform purchased from Mallinckrodt was distilled under nitrogen then added to the samples immediately after distillation. All other solvents were of the highest available grade and either used directly or distilled once.

Sample Preparation

In developing a procedure for preparing the DPPC/$CHBr_3$ samples, several factors were considered. To monitor the amount of $CHBr_3$ available for interaction with each molecule of lipid, concentrations are expressed as mole percent (mol%), defined as follows:

$$\text{mol\%} = \{m(CHBr_3)/[m(DPPC) + m(CHBr_3)]\} \times 100, \quad (41)$$

in which m represents the number of moles of the indicated species. Use of the more conventional molar (M) units

$$M = m(CHBr_3)/L(H_2O + DPPC + CHBr_3) \quad (42)$$

obscures the relationship between the lipid and the perturbing species.

However, even units of mole percent are meaningless if the small quantities ($\sim 10^{-1}\mu l$) of $CHBr_3$ were largely dissolved in the water phase. Multilamellar vesicles are normally prepared with a lipid/water concentration of 1-2mg/ml. Although the solubility of $CHBr_3$ is only slight ($\sim 1\mu l/ml$), the usual quantities of water in a sample preparation are more than large enough to compensate. To avoid loss of the less-than-microliter quantities of $CHBr_3$ to the water phase, the volume of water in the sample should be minimal when the $CHBr_3$ is added. This might be accomplished in several ways:

1) By using very much smaller volumes of water in the initial preparation of the vesicles

2) By adding the $CHBr_3$ to the dry lipid before vesicle formation

3) By removal of the bulk of the water from the original vesicle preparation prior to the addition of $CHBr_3$

All three methods were tested and found ultimately to give the same results. However, in both the first and second methods, vesicle formation was slow and the equilibration times were long. Since the third method provided reproducible experimental results which were identical to those of the first two methods and since it allowed for aliquot preparations at several DPPC/$CHBr_3$ concentrations, this method was adopted in the standard procedure described next.

The dry lipid was dissolved in a 50:50 v/v solution of chloroform/methane, which was removed by rotary evaporation under a stream of nitrogen to leave a thin film of the lipid in the glass vial. After vacuum desiccation overnight, the sample was heated to 45°C ($T > T_m$) and a large excess of water at 45°C was added. After vigorous vortexing for one minute, the hydrated sample was incubated above T_m for one hour with intermittent, brief vortexing. Four aliquots of the suspension of multilamellar vesicles produced by this procedure were transferred to separate vials which were subsequently handled identically, irrespective of bromoform addition. First, each vial was centrifuged for twenty minutes at 1500xg and all but ~10μl of excess water was removed. Using a 1μl syringe, an appropriate volume of $CHBR_3$ (0, 10, 20, or 30mol%) was added to each of the vials. The samples were then annealed for one hour above T_m and allowed to equilibrate at room temperature overnight. The contents of each vial were transferred to 1mm-diameter glass capillaries so that each capillary contained 2-3 mg of lipid. These samples were centrifuged at 1500xg for 20 min. to separate the lipid-rich vesicle phase from the excess water phase. Most of the excess water was removed by syringe, leaving only a small meniscus above the sample pellet. The capillaries, after being flame sealed and centrifuged at 5500xg, were placed in an annealing stage at 4°C for at least one week. Usually, the samples were transferred from the annealing stage to the cooled (~0°C) sample stage of the x-ray apparatus without being allowed to warm above the subtransition temperature (T_s) before measurements were begun. At least two spectra were taken at ~ 0°C to ascertain that annealing was complete. A few samples, prepared before the annealing stage was available, were

unavoidably exposed to room temperature before being mounted in the sample stage of the x-ray apparatus. These samples were cooled to 0°C and annealed in the sample stage itself for several days (>70 hrs.), until both the low and wide angle diffraction patterns stabilized.

Partition Coefficient

In a system of two immiscible liquids, the partition coefficient K is defined as the ratio of the concentration of a solute in one (organic) phase to the concentration of the solute in the other (aqueous) phase. Although the partition coefficient for bromoform in DPPC has not been measured, the coefficient for similar systems is known. Physical constants, including partition coefficients, for some related or similar solutes are shown in Table 9.

The partition coefficient for bromoform can be estimated from its aqueous solubility relative to the solubility of the other solutes in the table. The values of the partition coefficients in Table 9 suggest an inverse correlation with aqueous solubility: the lower the solubility, the higher the lipid/water partition coefficient. Based on this empirical relationship, the partition coefficient of bromoform would be expected to fall between that of halothane and benzene, or $\sim 2.5 \times 10^3$. A similar correlation between aqueous solubility and the partition coefficient P based on concentration units of mg/l is observed in the octanol/water system. An empirical relationship for the dependence of the partition coefficient on aqueous solubility in this system was reported by Leo [133]:

$$\log P = 4.5 - 0.75 \log S, \qquad (43)$$

in which the concentrations are expressed in mg/l. Applying this equation to calculate the partition coefficient for bromoform in the octanol/water system leads to a value for P of 74.5. For comparison of this value with values in Table 9, P must be converted to units of mole fraction. With the molecular weight $M(C_8H_{17}OH) = 130.23$ g/mol and the density $d(C_8H_{17}OH) = 0.827$ g/cm^3, $K \sim 330$.

If the calculated K = 330 is applied to the conditions of the experiments in this report, with a lipid concentration of 5mg/μl, the actual concentration of the bromoform in the bilayers would be 27mol% in the 30mol% samples and 8.5mol% in the 10mol% samples. However, for

TABLE 9

Physical Properties of Bromoform and Related Solutes

	M	V	δ	S	K		
Solute	gm/ mol	cm^3/ mol	$MPa^{\frac{1}{2}}$	mg/ $1H_2O$	X_B/X_W	Lipid System	T phase °C
$CHCl_3$	119.4	80.7	18.8	8232	$1.06x10^3$	DMPC (ULVs)	25 L_α
$C_2HBrClF$	197.4	106.4	18.1	3454	$2.05x10^3$	DMPC (ULVs)	30 L_α
$CHBr_3$	252.8	88.0	21.5	3190	---	--- ---	---
C_6H_6	78.1	88.7	18.7	1780	$2.75x10^3$	DMPC (MLVs)	25 L_α
CCl_4	153.8	97.1	17.6	1160	$6.91x10^3$	DMPC (ULVs)	30 L_α

M molar weight
V molar volume
δ Hildebrand parameter
S aqueous solubility
K partition coefficient

Aqueous solubilities for chloroform and halothane ($C_2HBrClF_3$) are converted from the values of S in Hill [129]. The partition coefficients for halothane and chloroform are from Kamaya [130]. The benzene partition coefficient is from Simon et al.[131] and that for carbon tetrachloride from Inoue and coworkers [132]. Molar volumes and cohesion parameters, except for halothane, are from Barton [116]. The molar volume of halothane is from Kamaya et al. [130] and the cohesion parameter is calculated using substituent parameters from Barton [116].

chloroform (P_{obs} = 93.3, P_{calc} = 37.4) and carbon tetrachloride (P_{obs} = 436.5, P_{calc} = 208.9), the calculated values of the octanol/water partition coefficient are lower than the observed values by a factor of two [134]. Furthermore, the observed octanol/water partition coefficients tend to be lower than those measured for diacyl lipids. Thus partitioning of bromoform into the lipid would be expected to be higher by at least a factor of two and probably more like a factor of four or five than the calculated octanol/water value. Even if the coefficient were as low as the calculated octanol/water value would predict, more than 80% of the total solute concentration would be in the lipid phase.

Qualitative Results

The MLV suspensions containing $CHBr_3$ appeared more translucent and less homogeneous than those without $CHBr_3$. After an equal amount of time centrifuged, the water/lipid pellet boundary was less clear and the time of annealing at 0°C required to produce stable spectra was longer for the $CHBr_3$ samples.

D vs. T

As seen in by comparing Figures 16 and 26, at the lower concentrations (10 and 20 mol%) the low- and wide-angle patterns of the samples both with and without $CHBr_3$ exhibit the same general features in a given phase. At the higher concentration (30mol%), the overlapping of transitions and broad coexistence regions complicate analysis, making phase identification difficult at a given temperature.

In Figure 27, the variation of peak positions at each concentration is shown as a function of temperature. At every concentration the transition profile is affected by the presence of the $CHBr_3$ either by changing the transition width or the transition temperature, or both. In general, the transition widths are broadened and the transition temperature is lowered.

Pin-pointing the transition temperature using x-ray diffraction data at discrete temperatures results in some ambiguity in the value, but the composite data, both low- and wide-angle, from several experiments at 10mol% suggest that the width of the pretransition may

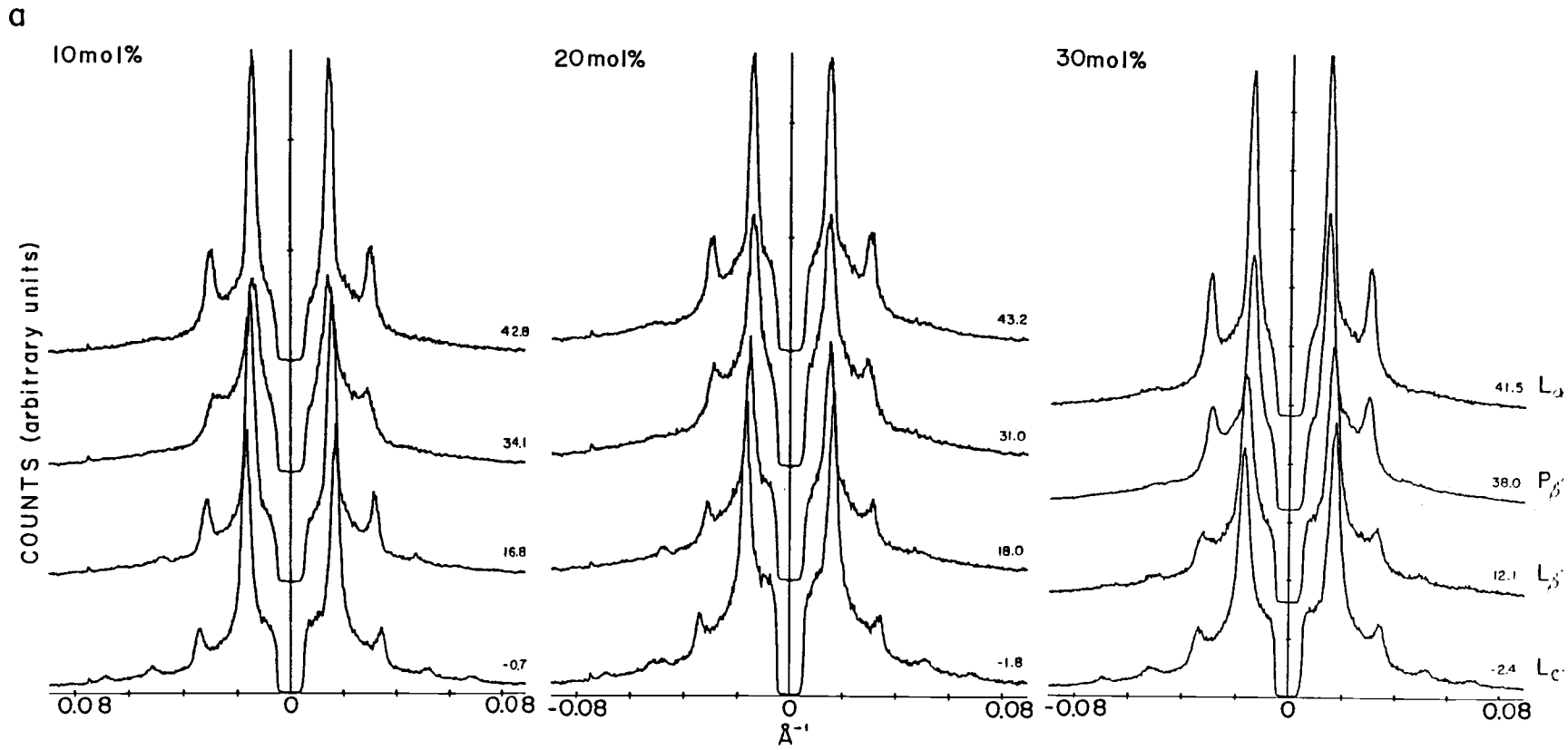

Figure 26: Representative diffraction patterns of each phase from MLVs of DPPC in excess H_2O at 10, 20 and 30mol% bromoform. Temperatures (°C) are indicated to the right of each pattern.
a) low-angle patterns from the $L_{c'}$, $L_{\beta'}$, $P_{\beta'}$ and L_{α} phases

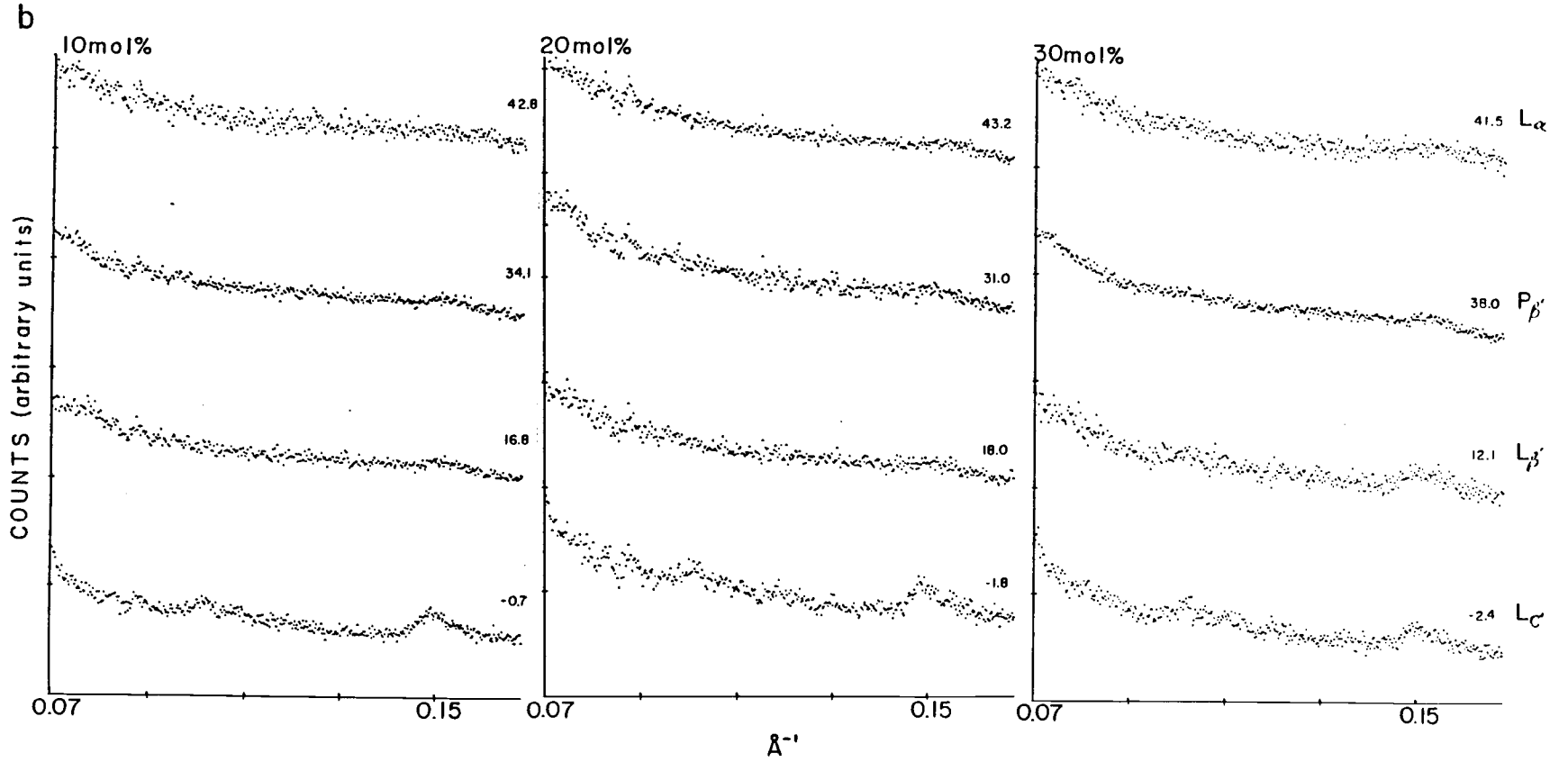

Figure 26 continued: Representative diffraction patterns of each phase from MLVs of DPPC in excess H_2O at 10, 20 and 30mol% bromoform. Temperatures (°C) are indicated to the right of each pattern.
b) intermediate-angle patterns from the $L_{c'}$, $L_{\beta'}$, $P_{\beta'}$ and L_α phases

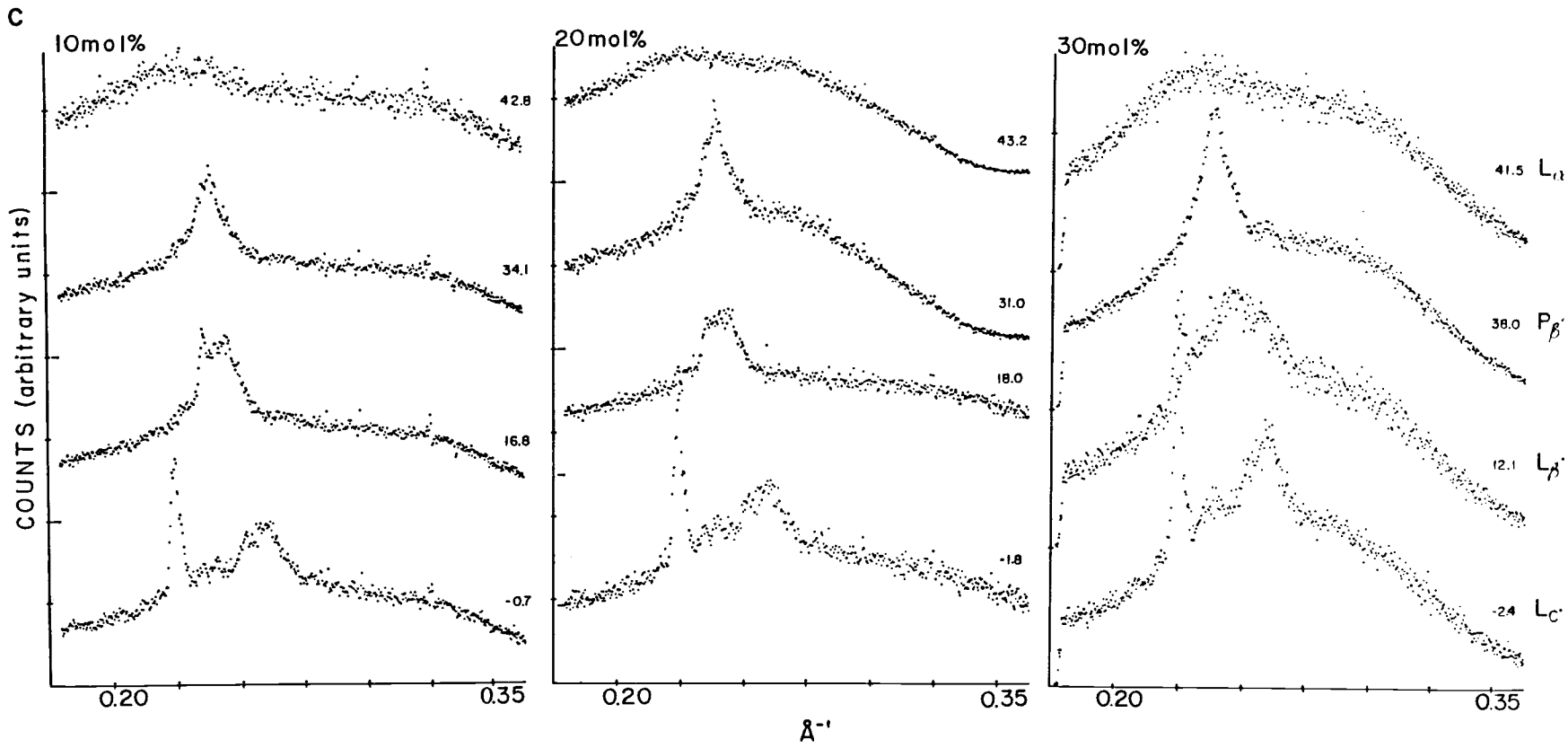

Figure 26 continued: Representative diffraction patterns of each phase from MLVs of DPPC in excess H_2O at 10, 20 and 30mol% bromoform. Temperatures (°C) are indicated to the right of each pattern.
c) wide-angle patterns from the $L_{c'}$, $L_{\beta'}$, $P_{\beta'}$ and L_α phases

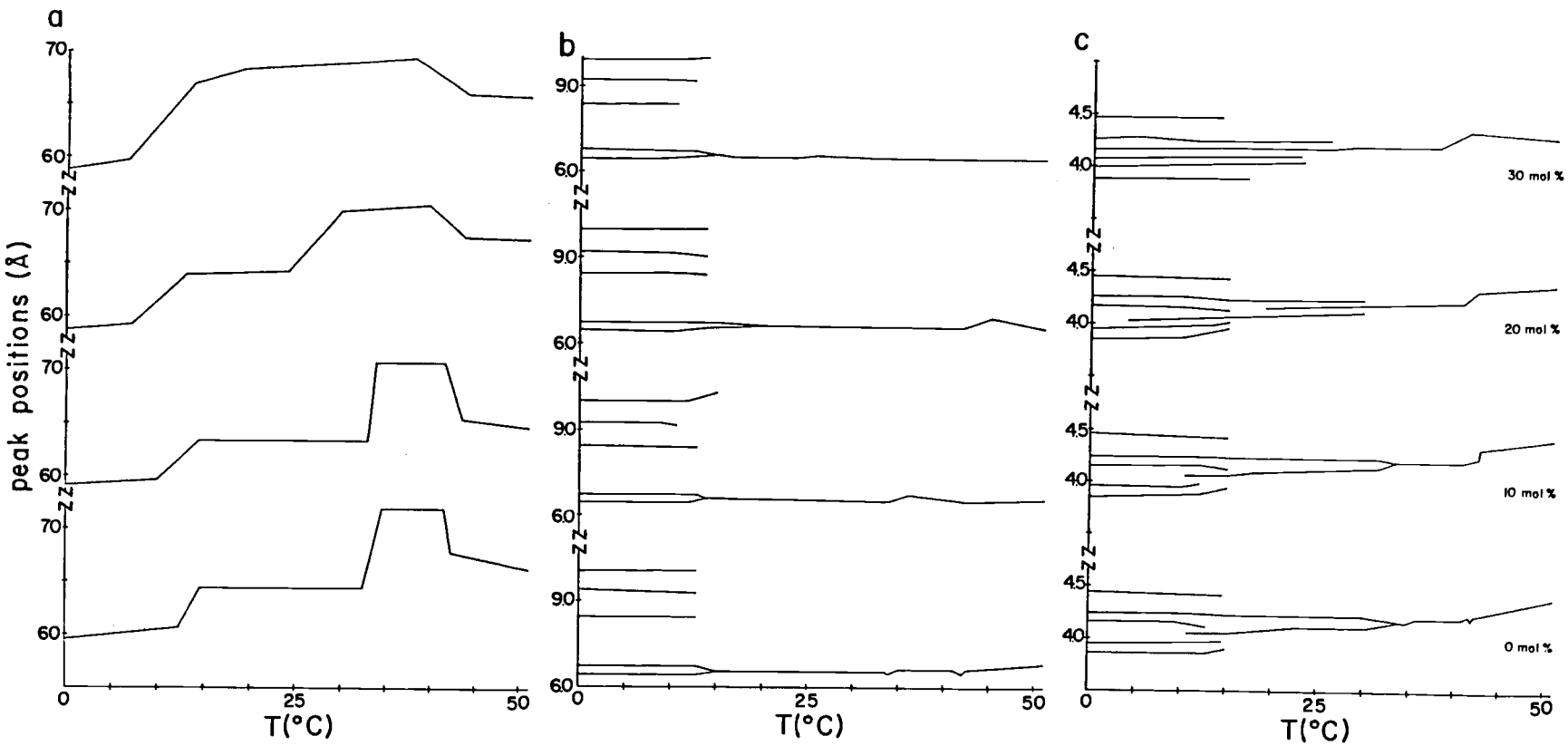

Figure 27: Temperature dependence of reflections from MLVs of DPPC in excess H_2O with 0, 10, 20 and 30mol% bromoform. Variation in a) low-angle, b) intermediate-angle and c) wide-angle spacing at each concentration.

be narrower than that of the pure lipid. The temperature of the main transition may also be ~0.5°C higher than for the pure lipid.

Electron Density Profiles

The electron density profiles shown in Figure 28 were calculated using the relative intensities of the lamellar reflections in each phase, which are listed in Table 10. The intensities I_h were obtained by averaging values from all samples studied at a given concentration.

$L_{c'}$ phase (5 orders)

As the concentration of bromoform increases to 30mol%, peak-to-peak distance of the electron density profile decreases to an apparent minimum of 39.14Å, which is only ~1Å smaller than that of the pure lipid. The shape of the methyl trough becomes somewhat deeper and narrower, suggesting increased order in that region, and the peak-to-trough amplitude is slightly larger, possibly reflecting the increased electron density due to the presence of the bromoform.

$L_{\beta'}$ phase (5 orders)

The profiles for 0, 10 and 20mol% are very similar but again, the peak-to-peak distances are slightly smaller, the shapes of the methyl troughs are somewhat narrower and deeper and the peak-to-trough amplitudes are greater in the bromoform samples. Because of the coexistence of the $L_{c'}$, $L_{\beta'}$ and $P_{\beta'}$ phases and the decrease in the number of lamellar orders from 5 at lower concentrations to 4 at 30mol%, the shape of the profile at this concentration is different from those at lower concentrations.

$P_{\beta'}$ phase (2 orders)

In the rippled phase, the width of the trough, as measured at half the peak-to-trough distance, remains constant up to 20mol%. The peak-to-peak distance at 10mol% decreases from its value at 0mol%, but increases again at 20mol% to a value still below that at 0mol%. At 30mol%, the trough becomes a higher-density plateau with a width 1½ times that at lower concentrations. Although interpretation of electron density profiles based on only two or three orders is not very

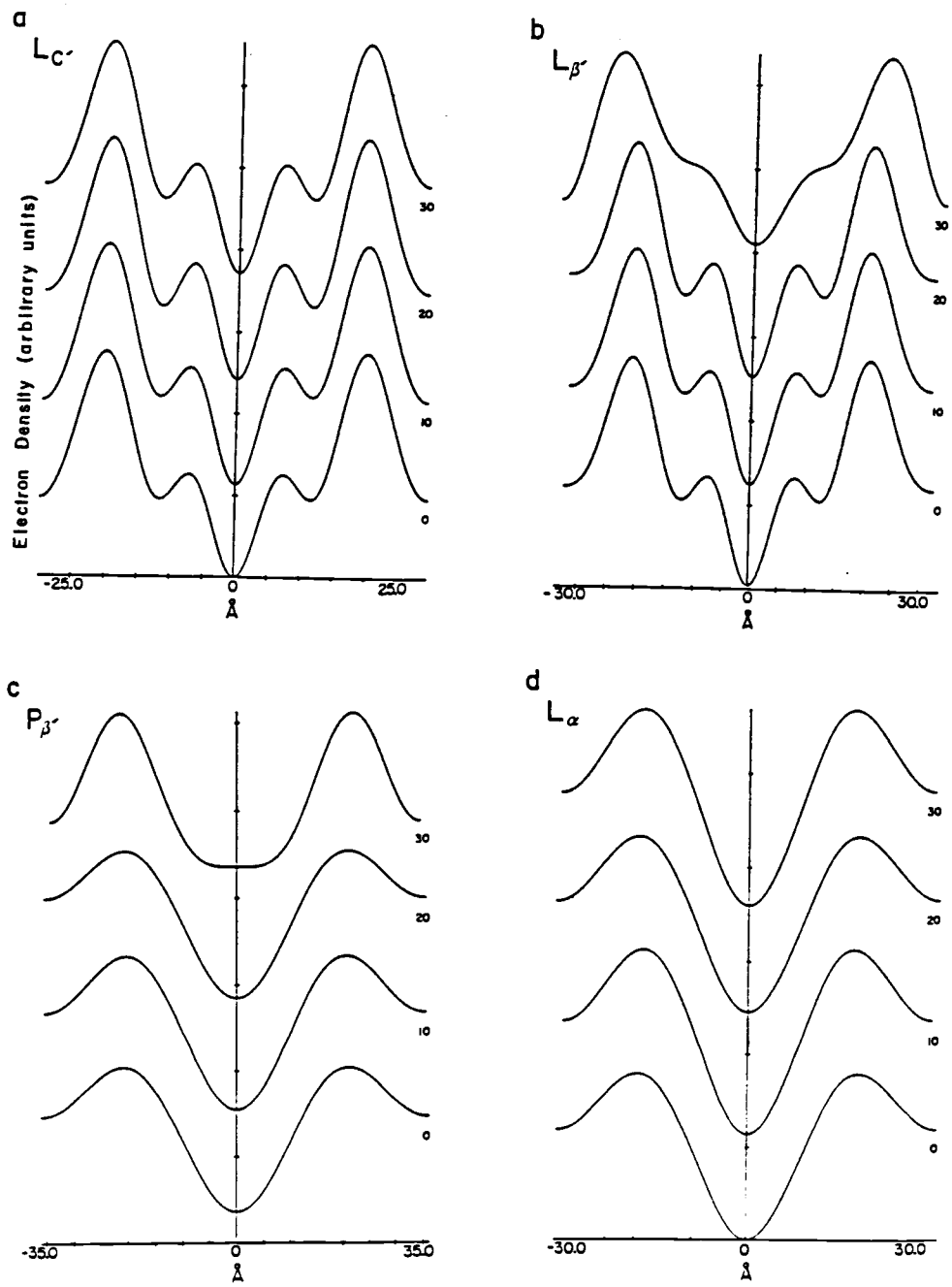

Figure 28: Projected electron density profiles for bilayers of DPPC in excess H_2O with 0, 10, 20 and 30mol% bromoform. Profiles from the a) $L_{c'}$, b) $L_{\beta'}$, c) $P_{\beta'}$, and d) L_{α} phases are shown. Concentrations (mol%) are indicated to the right of the profiles, which are offset for clarity.

TABLE 10

Relative Intensities for DPPC Plus Bromoform

Phase	Conc. $CHBr_3$ (mol%)	Order h	I_h	Relative Intensity $(h^2I_h/I_1)^{1/2}$	Phase	Conc. $CHBr_3$ (mol%)	Order h	I_h	Relative Intensity $(h^2I_h/I_1)^{1/2}$
$L_{c'}$	0	1	12.55	-1.00	$L_{\beta'}$	0	1	12.89	-1.00
T	-0.5°C	2	1.81	+0.76		24.1°C	2	2.61	+0.90
d	59.5Å	3	0.51	-0.60		64.4Å	3	0.43	-0.55
		4	0.33	-0.65			4	0.20	-0.50
		5	0.05	-0.32			5	0.12	-0.48
	10	1	12.20	-1.00		10	1	13.18	-1.00
T	-0.6°C	2	2.03	+0.82		24.6°C	2	2.83	+0.93
d	59.1Å	3	0.48	-0.60		63.3Å	3	0.46	-0.56
		4	0.38	-0.71			4	0.23	-0.53
		5	0.06	-0.35			5	0.11	-0.46
	20	1	11.09	-1.00		20	1	11.21	-1.00
T	-0.5°C	2	1.55	+0.75		20.7°	2	2.13	+0.87
d	58.8Å	3	0.55	-0.67			3	0.44	-0.59
		4	0.33	-0.69			4	0.19	-0.52
		5	0.09	-0.45			5	0.13	-0.54
	30	1	11.19	-1.00		30	1	8.47	-1.00
T	-0.7°C	2	1.44	+0.72		14.0°C	2	1.77	+0.91
d	58.8Å	3	0.46	-0.61		67.0Å	3	0.32	-0.58
		4	0.29	-0.64			4	0.18	-0.58
		5	0.07	-0.40					
$P_{\beta'}$	0	1	9.70	-1.00	L_{α}	0	1	12.28	-1.00
T	35.8°C	2	2.20	+0.95		43.7°C	2	2.73	+0.94
d	71.9Å					67.0Å			
	10	1	9.70	-1.00		10	1	12.10	-1.00
T	35.1°C	2	2.50	+1.02		42.7°C	2	3.43	+1.06
d	70.7Å					65.1Å			
	20	1	10.19	-1.00		20	1	11.19	-1.00
T	35.0°C	2	2.10	+0.91		44.6°C	2	2.91	+1.02
d	69.9Å					67.5Å			
	30	1	9.33	-1.00		30	1	11.55	-1.00
T	27.0°C	2	2.30	+0.99		42.8°C	2	3.95	+1.17
d	68.6Å	3	0.31	-0.55		66.0Å			

reliable, this change in shape may reflect the incursion of the solute into the more ordered regions of the bilayer near the head groups. This is the only phase in which the peak-to-trough distance decreases as a function of bromoform concentration.

L_α phase (2 orders)

In the liquid crystalline phase, the peak-to-peak distance of the profile and the width of the methyl trough change non-monotonically as a function of solute concentration. The peak-to-trough amplitude in the presence of solute is increased over that in its absence, but its concentration dependence is also not monotonic. With only two orders of diffraction, the differences in profiles are not great enough to be significant.

Quantitative Results

Analysis of the parameters for bilayers containing bromoform is hindered by the unavailability of specific volumes for the lipid/solute phase. However, three cases based on three different assumptions about the behavior of the bilayer parameters in the presence of solute can be argued.

If the volume of the lipid in the presence of the solute were the same as in its absence (V_l) and the volume of the solute were just its bulk volume (V_s), the total volume of the lipid phase (V_{ls}) could be calcuted as a simple sum:

$$V_{ls} = V_l + V_s . \qquad (44)$$

This is not necessarily true [135-138], but the analysis based on the assumption, referred to as Case 1, can be carried out and the results regarded as possible values.

A second approach, referred to as Case 2, assumes that the relationship between d_l and d_{pp} is unchanged by the presence of solute in the bilayer so that

$$d_l(\text{DPPC+CHBr}_3) = d_{pp} + [d_l(\text{DPPC}) - d_{pp}(\text{DPPC})]. \qquad (45)$$

This also is not precisely true, since the headgroup areas (and thus conformations) do change as a function of solute concentration, but results are useful for purposes of comparison. This assumption implies

that the length of the untilted molecule changes as a function of solute concentration.

A third assumption that allows calculation of the bilayer parameters, referred to as Case 3, is that the length of the molecule in the absence of tilt ($d_1°$) does not change as a function of solute concentration, so that

$$d_1°(\text{DPPC+CHBr}_3) = d_1°(\text{DPPC}). \qquad (46)$$

In fact, the effective length of the extended molecule may be shortened or lengthened by accomodation of the solute molecules and the effect may vary from phase to phase or concentration to concentration.

Comparison of the parameters obtained from analyses based on these three assumptions with the values obtained in the absence of solute provides some indication of the actual structures in the presence of solute. In some cases, physically unreasonable parameters result and the validity of the assumption can be nullified. Table 11 lists the observed and calculated bilayer parameters for MLVs of DPPC in excess water as a function of bromoform concentration.

Subgel phase $L_{c'}$

Inspection of Table 11 reveals that the concentration dependence of most of the parameters listed is non-monotonic. The lamellar repeat distance d and the peak-to-peak distance d_{pp} decrease to apparent limiting values of 58.8Å and 39.14Å, respectively. This decrease in d partly reflects a decrease in hydration levels, but also alterations in packing parameters, which continue to change after d has stabilized.

Table 11 shows that the hydration level either decreases or remains unchanged as a function of concentration, depending on which of the three cases is examined. The Case 1 assumption implies that the lipid molecule in the presence of 30mol% bromoform is 5% longer than in its absence. Case 2 results in unreasonably and increasingly small volumes (A_1d_1) for the lipid plus solute as the solute concentration increases.

The overall results from the Case 3 evaluation, in which the length of the lipid molecule is unaffected by the presence of solute, seem most reasonable. In this case, the volume increases only slightly

TABLE 11

Observed and calculated bilayer parameters for MLVs of DPPC in excess H2O plus bromoform

Conc. $CHBr_3$ (mol%)	0	10	20	30
$L_{c'}$ phase				
d (Å)	59.5	59.1	58.8	58.8
s_1^{-1} 02	10.0	10.0	9.97	9.93
s_2^{-1} 21	9.39	9.25	9.19	9.23
$s_{1'}^{-1}$ 2′0′	4.44	4.46	4.45	4.47
$s_{2'}^{-1}$ 1′2′	3.86	3.85	3.85	3.88
a_1	21.26	20.87	20.72	20.84
b_1	20.00	20.00	19.94	19.86
a_c	8.88	8.92	8.90	8.94
b_c	8.58	8.54	8.54	8.61
A_1 ($Å^2$)	53.15	52.16	51.64	51.74
A_c ($Å^2$)	19.05	19.04	19.00	19.25
Φ (°)	44.21	43.11	42.62	41.92
V_x ($Å^3$)	1581	1541	1518	1521
Case 1: $V_{1s} = V_1 +$	16	36	62$Å^3$	
V_{1s} ($Å^3$)	1103	1119	1139	1165
d_1° (Å)	57.90	58.77	59.95	60.52
d_1 (Å)	41.51	42.90	44.11	45.03
d_{pp} (Å)	40.07	39.67	39.14	39.14
d_1-d_{pp} (Å)	1.44	3.23	4.97	5.89
d_w (Å)	17.99	16.20	14.69	13.77
n_w (mol/mol)	15.99	14.13	12.69	11.91
wt% H_2O	28.18	25.33	22.87	21.21
Case 2: $d_1 = d_{pp} + 1.44Å$				
d_{pp} (Å)	40.07	39.67	39.14	39.14
d_1 (Å)	41.51	41.11	40.58	40.58
d_1° (Å)	57.90	56.31	55.15	54.54
$V_{1s} = A_1 d_1$ ($Å^2$)	1103	1072	1048	1050
d_w (Å)	17.99	17.99	18.22	18.22
n_w (mol/mol)	15.99	15.69	15.73	15.76
wt% H_2O	28.18	27.36	26.88	26.27

TABLE 11 continued

$L_{c'}$ phase continued

Case 3: $d_1°$(DPPC + $CHBr_3$ = $d_1°$(DPPC) = 57.90Å

d_{pp} (Å)	40.07	39.67	39.14	39.14
d_1 (Å)	41.51	42.27	42.61	43.08
d_1-d_{pp} (Å)	1.44	2.60	3.47	3.94
$V^{1s} = A_1 d_1$ (Å^3)	1103	1102	1100	1114
d_w (Å)	17.99	16.83	16.19	15.72
n_w (mol/mol)	15.99	14.68	13.98	13.60
wt% H_2O	28.18	26.05	24.62	23.51
T_c (°C)	13.5	12.2	10.1	10.2
ΔT_c (°C)	2.3	4.4	5.8	7.0

$L_{\beta'}$ phase

d (Å)	64.4	63.3	64.0	67.0
s^{-1} 02	6.55	6.61	6.59	6.62
$s_1'^{-1}$ 2′0′	4.22	4.23	4.24	4.26
$s_2'^{-1}$ 1′2′	4.11	4.12	4.09	4.11
a_1 10	7.56	7.63	7.61	7.64
b_1 01	13.10	13.22	13.18	13.24
a_c 1′0′	8.44	8.46	8.48	8.52
b_c 0′1′	9.41	9.43	9.34	9.38
A_1 (Å^2)	49.54	50.43	50.15	50.58
A_c (Å^2)	19.86	19.95	19.80	19.98
Φ (°)	36.70	37.70	37.85	37.81
V_x (Å^3)	1595	1596	1605	1694

Case 1: V_{1s} = V_1 + 16 36 62Å^3

V_{1s} (Å^3)	1145	1161	1181	1207
$d_1°$ (Å)	57.65	58.20	59.65	60.41
d_1 (Å)	46.22	46.05	47.10	47.73
d_{pp} (Å)	41.77	41.08	41.38	46.66
d_1-d_{pp} (Å)	4.45	4.97	5.72	1.07
d_w (Å)	18.18	17.25	16.90	19.27
n_w (mol/mol)	15.06	14.55	14.17	16.30
wt% H_2O	26.97	25.88	24.88	26.92

TABLE 11 continued

$L_{\beta'}$ phase continued

Case 2: $d_1 = d_{pp} + 4.45Å$

d_{pp} (Å)	41.77	41.08	41.38	46.66
d_1 (Å)	46.22	45.53	45.83	51.11
$d_1°$ (Å)	57.65	57.54	58.04	64.69
$V_{1s} = A_1 d_1$ (Å^2)	1145	1148	1149	1293
d_w (Å)	18.18	17.77	18.17	15.89
n_w (mol/mol)	15.06	14.99	15.24	13.44
wt% H_2O	26.97	26.46	26.26	23.30

Case 3: $d_1°$(DPPC + $CHBr_3$) = $d_1°$(DPPC) = 57.65Å

d_1 (Å)	46.22	45.61	45.52	45.55
d_{pp} (Å)	41.77	41.08	41.38	46.66
d_1-d_{pp} (Å)	4.45	4.53	4.14	-1.11
$V_{1s} = A_1 d_1$ (Å^3)	1145	1150	1141	1152
d_w (Å)	18.18	17.69	18.48	21.45
n_w (mol/mol)	15.06	14.92	15.50	18.14
wt% H2O	26.97	26.37	26.59	29.08
T_p (°C)	33.5	33.5	27.1	16.3
ΔT_p (°C)	2.1	1.0	5.8	6.7

$P_{\beta'}$ phase

d (Å)	71.9	70.7	69.9	68.6
s^{-1} 02	6.63	6.74	6.69	6.62
s'^{-1} 0′2′	4.20	4.20	4.20	4.20
a_1 10	7.66	7.78	7.72	7.64
b_1 01	13.26	13.48	13.38	13.24
a_c 1′0′	9.70	9.70	9.70	9.70
b_c 0′1′	8.40	8.40	8.40	8.40
A_1 (Å^2)	50.79	52.44	51.65	50.58
A_c (Å^2)	20.37	20.37	20.37	20.37
Φ (°)	36.67	39.02	37.93	36.35
V_x (Å^3)	1808	1854	1805	1735

TABLE 11 continued

$P_{\beta'}$ phase continued

Case 1: $V_{1s} = V_1 +$	16	36	62Å^3
V_{1s} (Å^3)	1166	1182	1202	1228
$d_1°$ (Å)	57.24	58.03	59.01	60.28
d_1 (Å)	45.91	45.09	46.54	48.55
d_{pp} (Å)	42.05	40.87	41.62	43.23
d_1-d_{pp} (Å)	3.87	4.12	4.92	5.32
d_w (Å)	25.29	25.61	23.36	20.05
n_w (mol/mol)	21.48	22.46	20.18	16.96
wt% H_2O	34.50	35.03	32.05	27.71

Case 2: $d_1 = d_{pp}$ + 3.87Å

d_{pp} (Å)	42.05	40.87	41.62	43.23
d_1 (Å)	45.91	44.74	45.49	47.10
$d_1°$ (Å)	57.24	57.59	57.67	58.48
$V_{1s} = A_1 d_1$ (Å^3)	1166	1173	1175	1191
d_w (Å)	25.29	25.96	24.41	21.50
n_w (mol/mol)	21.48	22.76	21.08	18.19
wt% H_2O	34.50	35.33	33.01	29.13

Case 3: $d_1°$(DPPC+$CHBr_3$) = $d_1°$(DPPC) = 57.24Å

d_1 (Å)	45.91	44.47	45.15	46.10
d_{pp} (Å)	42.05	40.87	41.62	43.23
d_1-d_{pp} (Å)	3.87	3.60	3.53	2.87
$V_{1s} = A_1 d_1$ (Å^3)	1166	1166	1166	1166
d_w (Å)	25.29	26.23	24.75	22.50
n_w (mol/mol)	21.48	23.00	21.38	19.03
wt% H2O	34.50	35.57	33.32	30.08
T_m (°C)	41.9	42.5	41.2	40.9
ΔT_m (°C)	0.8	2.0	4.0	6.0

L_α phase

d_1 (Å)	67.0	65.1	67.5	66.0
s_2^{-1} 21	6.87	6.58	6.61	6.76
$s_{1'}^{-1}$ 0′2′	4.33	4.42	4.38	4.45

TABLE 11 continued

L_α phase continued

a_1 10	7.93	7.60	7.63	7.81
b_1 01	13.74	13.16	13.22	13.52
a_c 1′0′	10.00	10.21	10.12	10.28
b_c 0′1′	8.66	8.84	8.76	8.90
A_1 (Å^2)	54.48	49.99	50.45	52.77
A_c (Å^2)	21.65	22.56	22.16	22.87
Φ (°)	37.37	25.50	28.54	29.91
V_x (Å^3)	1825	1627	1703	1741
Case 1: V_{1s} = V_1 +		16	36	62Å^3
V_{1s} (Å^3)	1225	1240	1261	1287
d_1° (Å)	56.58	54.96	56.90	56.27
d_1 (Å)	44.95	49.61	49.99	49.17
d_{pp} (Å)	39.21	37.57	39.07	37.57
d_1-d_{pp} (Å)	5.74	12.04	10.92	11.60
d_w (Å)	22.03	15.49	17.51	16.83
n_w (mol/mol)	20.07	12.95	14.77	14.85
wt% H_2O	32.98	23.71	25.66	25.13
Case 2: d_1 = d_{pp} + 5.74Å				
d_{pp} (Å)	39.21	37.57	39.07	37.57
d_1 (Å)	44.95	43.31	44.81	43.31
d_1° (Å)	56.58	47.98	51.01	49.96
V_{1s} = A_1d_1 (Å^3)	1225	1083	1130	1143
d_w (Å)	22.03	21.79	22.69	22.69
n_w (mol/mol)	20.07	18.22	19.14	20.02
wt% H_2O	32.98	30.42	30.91	31.16
Case 3: d_1°(DPPC+$CHBr_3$) = d_1°(DPPC) = 56.58Å				
d_{pp} (Å)	39.21	37.57	39.07	37.57
d_1 (Å)	44.95	51.07	49.70	49.04
d_1-d_{pp} (Å)	5.74	13.50	10.63	11.47
V_{1s} = A_1d_1 (Å^3)	1225	1276	1254	1294
d_w (Å)	22.03	14.03	17.80	16.96
n_w (mol/mol)	20.07	11.71	15.02	14.97
wt% H_2O	32.98	21.94	26.06	25.28

on solute incorporation, while the area A_l and tilt angle Φ both decrease. These conditions lead to an increase in d_l as concentration increases, which is the opposite trend to that of d_{pp}. The partial unfolding of the head group, which might change the relationship between the two parameters, may be responsible for this apparent contradiction.

When the concentration is raised from 20mol% to 30mol%, the values of d, d_{pp}, A_l and n_w change little, but the sidechain area A_c expands. This lateral expansion may result from a degree of disorder induced by the presence of solute as the free volume in the bilayer becomes saturated. If the lipid volume is assumed to be the same regardless of sidechain area, the larger A_c would effectively reduce the length of $d_l°$ and Case 3 is not strictly applicable at 30mol%. If $d_l° = 57.65Å$, as in the $L_{\beta'}$ phase, $d_l = 42.90Å$, close to the value at 20mol%. V_{ls} is then $1110Å_3$, slightly larger than V_l, supporting the conclusion that the free volume is saturated at this concentration. At the lower concentrations, V_{ls} does equal V_l.

Subtransition T_s

Both the temperature and range of the subtransition are affected by the presence of even 10mol% bromoform. As the concentration of bromoform is increased further, the width of the transition is increased by smaller increments. In other words, the lower the concentration of bromoform, the larger the effect on the transition width.

The midpoint of the transition decreases at low concentrations and levels off when 30mol% bromoform is present. No samples at higher concentrations were studied, so it is not known whether the midpoint will increase or remain about the same as more bromoform is added.

Gel phase $L_{\beta'}$

Analysis of the sidechain parameters for the higher concentrations of bromoform is complicated by the presence of overlapping peaks in the wide angle region. However, the two strongest peaks are still those in the 4.25Å and 4.10Å regions and these have been indexed as the (2′0′) and (1′2′) reflections to derive the parameters listed in Table 11. The presence of the other peak or peaks may indicate alternate packing

modes or may simply be due to residual subgel or insipient ripple-phase reflections.

In the gel phase, the concentration dependence of the effect of the presence of bromoform is again non-monotonic for most parameters. The area per side chain changes <1% over the entire concentration range. The repeat distance d and the hydration level n_w decrease at 10mol%, but increase at 20mol%. At 30mol%, these parameters show substantial increases, but much of the change may be due to the coexistence of the gel and ripple phases. At this concentration, the pure gel phase is never exhibited, coexisting with either the subgel or the ripple phase.

In this phase, the Case 1 assumption can be discounted for the same reason as in the subgel phase. The Case 2 and Case 3 assumptions, however, lead to parameters with similar values which also seem physically reasonable. The Case 2 assumption implies that the headgroup conformation is not affected by the presence of the solute in the bilayer interior, while the Case 3 assumption implies that the dimensions of the lipid are not affected. Since the area per lipid A_l does increase slightly in the bromoform samples, a small change in headgroup conformation is likely and the true values for the bilayer parameters are probably between the Case 2 and Case 3 values. At 30mol%, the Case 2 assumption leads to a physically unreasonable value for $d_l{}^\circ$ (64.69Å). The Case 3 assumption leads to a value of d_{pp} which is larger than d_l, which is also unpalatable. This ambiguity may due to the presence of rippled phase in addition to the gel phase.

At the lower concentrations, the main effect of the presence of bromoform is to increase Φ, A_l and d_l, with n_w remaining more or less unaffected.

Pretransition T_p

The effects of the presence of bromoform on the pretransition profile are also non-monotonic. At 10mol%, the midpoint is unaffected, but the temperature range of the transition is decreased, indicating an increased degree of order. Above 10mol%, the presence of bromoform induces dramatic lowering of the transition midpoint and considerable broadening of the transition width. At 30mol%, as stated above, the

sub- and pretransitions overlap.

Rippled phase $P_{\beta'}$

The response of the rippled bilayer to the presence of bromoform is characterized by a monotonic decrease in the repeat distance as a function of concentration and by a nearly constant volume (2% maximum change) and side chain packing irrespective of solute concentration. The headgroup packing, tilt angle and hydration level adjust slightly to compensate the added solute as the concentration increases. Once again these changes are not monotonic and are far from dramatic.

Again the Case 2 and Case 3 assumptions lead to similar values. Since the lipid conformations are similar in the gel and rippled phases, this might be anticipated from the gel phase analysis. When $d_l°$ is held constant (Case 3), the value for $V_{ls} = A_l d_l$ is also constant and equal to V_l in this phase, implying that the solute molecules are completely absorbed in the free volume. If the value of d_l is calculated as a constant increment over d_{pp} (Case 2), the value of $A_l d_l$ is increased by $25Å^3$ over the pure lipid volume V_l. This is equivalent to ~1/5 the volume of a single molecule of bromoform. Again, the true values for the bilayer parameters may be between the Case 2 and Case 3 values.

Main transition T_m

The main effect of the presence of bromoform on the profile of the main transition is to broaden the range over which it occurs. At 10mol%, the transition midpoint is actually increased over that of the pure lipid, but even at 30mol%, the decrease in the midpoint is only 1°C. On the other hand, the width of the transition is doubled at each increment in solute concentration.

Liquid crystalline phase L_α

In the diffraction patterns of the liquid crystalline phases, the peaks in the intermediate region which result from molecular ordering are very broad, very weak and difficult to identify, even in the best cases. Use of the peak in the $(1/6.6)Å^{-1}$ region to calculate the area per molecule and the width of the lipid bilayer leads to values for d_l

which are much larger than d_{pp}. In fact, while d_{pp} decreases at 30mol%, using either the Case 1 or Case 3 assumption, d_l increases, resulting in a total difference of ~11.5Å per lipid. If the Case 2 assumption is applied to the 10mol% samples, V_{ls} is smaller than V_l by 142Å^3, which is approximately the volume of one whole molecule of bromoform. Although the volume does increase at higher concentrations, it remains well below V_l, even at 30mol% bromoform, making the validity of the Case 2 assumption suspect.

In the liquid crystalline phase, the area per sidechain increases in the presence of bromoform, suggesting that the value of $d_l°$ may actually contract as a result of increased disorder to accomodate the solute molecules. This would also shorten d_l, decreasing the discrepancy with d_{pp} while maintaining a reasonable value for V_{ls} (V_l). However, unless d_l decreases significantly, the difference between d_l and d_{pp} will remain large compared to that in other phases. For instance, at 30mol%, if $V_{ls} = V_l = 1225Å^3$, $dl° = V_{ls}/A_c = 53.56Å$, $d_l = 46.43Å$ and $d_l - d_{pp} = 8.86Å$. It must be concluded, then, that the presence of bromoform in the fluid phase has a significant effect on the headgroup conformation, which is reflected in the reduced headgroup areas, tilt angles and hydration levels.

Summary

The effects of bromoform on bilayers of DPPC were evaluated at 10, 20 and 30mol%, corresponding to solute/lipid mole fractions of 1/9, 1/4 and 3/7, respectively. The following observations were made:

1) In the subgel phase, the presence of bromoform induces changes in the headgroup lattices which result in smaller molecular areas. Slight adjustments of the chain lattices also occur, but the area per chain is maintained at ~19Å^2. The hydration level decreases as a function of bromoform concentration, in accordance with the smaller molecular areas and tilt angles. The bromoform is apparently assimilated into the free volume of the bilayer up to 20mol%. At 30mol%, the lipid portion of the bilayer begins to expand as it absorbs more solute. Since the polar areas are large in this phase, the solute volume can be accomodated in the hydrocarbon region by decreasing the tilt angle of the sidechains without affecting the total hydrocarbon,

and therefore lipid, volume.

2) The presence of bromoform decreases the temperature and increases the width of the subgel transition at all concentrations.

3) Except at 30mol%, the gel phase in the presence of bromoform is similar to that of the pure lipid. At 30mol%, the subgel and pretransition overlap, so the pure planar gel phase is never exhibited. At lower concentrations, the side chain area is the same as in the pure lipid, but the area per molecule is slightly expanded. The hydration level is relatively constant as a function of solute concentration in this phase.

4) At the higher concentrations, the presence of bromoform stabilizes the rippled phase, extending its temperature range from 8.4°C at 0 and 10mol% to 24.6°C at 30mol% $CHBr_3$. The induction of the rippled phase is apparently related to the ratio of the mass of the hydrocarbon region and the mass of the polar region, since neither shorter-chain phosphatidylcholines nor phosphatidylethanolamines exhibit this phase.

5) The area per chain ($20.37Å^2$) is maintained in the rippled phase, regardless of solute concentration, while the area per head group changes non-monotonically as a function of concentration. At the 30mol%, the area is about the same as in the pure lipid, but at the lower concentrations, it is larger. At 10mol% and 20mol%, the volumes of the lipid plus solute are only slightly larger than ($7Å^3$ and $9Å^3$, respectively) or the same as the volume of the pure lipid.

6) The midpoint of the main transition is only slightly affected by the presence of bromoform, but the width of the transition increases from 0.8°C in the pure lipid to 6°C at 30mol%.

7) In contrast to the other phases, the area per chain expands on solute uptake in the fluid phase. The headgroup areas are based on uncertain data, but a decrease as solute concentration increases is indicated. The solute volume is compensated by decreases in the tilt angles and increases in the disorder of the chains, with concomitant adjustments in hydration level.

CONCLUSIONS

The results of the studies presented in this thesis illustrate the complexity of interactions in bilayers of amphiphilic molecules. The structure which the bilayer assumes is determined by subtle interactions among the dimensions, densities and polarities of the hydrocarbon and polar regions and the hydration level, which in turn is partially determined by the amount of water available to interact.

The studies show that a complete analysis of x-ray diffraction patterns from phospholipid dispersions yields more details of the bilayer structures than previously obtained. If data from the low-, wide- and intermediate-angle regions are combined with the bilayer dimensions from the electron density profiles, the bilayer structure can be fully specified in all phases, if the specific volume of the lipid is also known. The parameters obtained include the sidechain and headgroup arrangements and areas, the tilt angle of the sidechains, the bilayer width, the degree of hydration and the temperatures and widths of the phase transitions. If the reflections in the diffraction pattern are assigned correctly, the calculated width of the lipid bilayer can be compared with the width obtained from the corresponding electron density profile and the relationship between them derived. This analysis provides further information concerning the headgroup conformation and assists in validifying the reflection assignments, especially in systems for which the specific volumes are not available.

The analysis was applied to three different systems of fully-hydrated MLVs: pure DPPC, pure isobranched PCs and DPPC/$CHBr_3$ in several concentrations. In the course of the analyses, several ambiguities in the structures of lipid bilayers were resolved. Results are summarized below.

Structure of the unperturbed model bilayers: DPPC

A reevaluation of the phases of pure DPPC in excess water determined that the hydration level in the subgel phase is greater, not less, than that in the gel phase. It also revealed that the subgel and gel phases coexist as the temperature is raised through the subgel transition, rather than transforming gradually as occurs on cooling to

the subgel phase. If the kinetics of hydration at low temperatures are slow compared to that of dehydration, this may explain the long annealing period required to attain the subgel phase. Comparison of the known molecular volume of DPPC with data from the diffraction studies established unambiguously that the side chains tilt substantially in the rippled phase, thus settling a long-standing controversy. In addition, the decreasing order in the side chains was observed in the decreasing length of the fully-extended molecule.

Structures of intrinsically perturbed bilayers: 17iPC and 20iPC

The bilayer structures of two isoacylphosphatidylcholines, one with an even number of carbons in the length of the side chains (17iPC) and one with an odd number (20iPC), were determined and were found to differ significantly from those of the straight-chain analogs. In 17iPC, the presence of the single methyl group at the end of each chain affects the way the polar groups are arranged, resulting in a larger area per head group than in DPPC. Since the hydrocarbon volume of 17iPC is greater than that of DPPC, the larger headgroup area is expected. On the other hand, the area per chain is larger, so the tilt of the side chains and the hydration level are actually lower. In the fluid phase, the polar area, tilt angle and hydration level are all smaller than those of DPPC in the same phase. In the subgel phase of 20iPC, the lipid area, sidechain tilt angle and hydration level are smaller than those of 17iPC. In the gel phase, these parameters are larger. The sidechain packing is also different than that of 17iPC in each phase, probably because of the odd number of carbons in the length of its chains. No structures are available for straight-chain analogs with an odd number of carbons in the chains, so no comparisons can be made in packing modes. For reasons which are unclear, neither branched-chain lipid exhibits a rippled phase.

Structures of extrinsically perturbed bilayers: DPPC plus bromoform

The main effect of the presence of bromoform in bilayers of DPPC is to stabilize the rippled phase and destabilize the planar gel phase. Minor adjustments in the packing modes of the polar and hydrocarbon regions are made in response to the inclusion of the solute. The

volume occupied by the solute molecule in the bilayer interior is somewhat dependent on the phase, but is close to zero in all phases at low concentration.

To compare the results from the data on the intrinsic and extrinsic perturbations, the physical differences in the systems must be considered. In the systems of methyl-branched lipids, the perturbing element is constrained by covalent bonding to be in the midplane of the bilayer. This forces the molecule to pack in a manner that accomodates the increased volume in that region. In contrast, the bromoform molecules are not confined in the bilayer, but are free to move into the hole volumes created by thermal fluctuations. According to the studies of Katz [139], the size of the hole volumes created is $\sim 50 Å^3$, about one-third the volume of a single molecule of bromoform.

In 17iPC, the presence of two additional methyl groups has little effect on the density of the hydrocarbon region of the bilayer. Since the density of a methyl group is lower than that of bulk hydrocarbon, the hydrocarbon volume in this species in the subgel phase is larger than that of DPPC by only $54 Å^3$, which is the equivalent of the volume of one methyl group in unbranched hydrocarbons. The density of the 20iPC is slightly lower than that of 17iPC or DPPC in each phase, probably due to the less efficient chain-packing because of the odd number of carbons in the lengths.

The density of bromoform, on the other hand, is much greater than that of hydrocarbons. Thus an increase in density of the hydrocarbon region of the bilayer is expected when bromoform is taken up by the bilayer.

Discussion

Although several questions concerning the structures of bilayers of DPPC have been answered as a result of the work presented in this thesis, many remain unanswered. Why the isobranched lipids exhibit no rippled phase while the presence of a small, lipophilic solute ($CHBr_3$) stabilizes it is unclear. In the absence of structural data on an unbranched analog of 20iPC, the effect of the presence of the methyl group cannot be separated from the influence of the odd-chain packing mode. A similar study of a straight chain analog with 19 carbons per

chain would render the data on 20iPC more useful for interpreting the effects of the presence of the methyl branches in both branched analogs. The precise relationship between hydration level and other physical parameters of the bilayer is still not completely understood. Studies at different hydrations might elucidate this relationship, if the other parameters were monitored carefully as well.

The results of the studies in this thesis emphasize the necessity of a more systematic approach to the determination of the structural parameters of phospholipid bilayers. A full complement of data from diffraction studies should include low-, intermediate- and wide-angle patterns and electron density profiles. If the volume of the lipid or lipid-solute portion of the bilayer is also available, the diffraction results can be interpreted unambiguously and the bilayer structure described completely. Once the structures are described more fully under a variety of conditions, the physical basis for the bilayer and bilayer-solute interactions leading to the structures may become clearer. When the physical basis for the interactions is understood, this knowledge can be applied to understand the functioning of natural membranes and to design synthetic membranes for such disparate purposes as delivery of pharmaceuticals, selective filtration and microdevices.

REFERENCES

1. Israelachvili, J. N., Marcelja, S. and Horn, R. G. (1980). Physical Principles of Membrane Organization. Quarterly Reviews of Biophysics 13: 121-200.

2. Bittar, E. E. (1980-1984). Membrane Structure and Function, vol. 1-6. John Wiley & Sons, New York.

2. Tanford, C. (1980). The Hydrophobic Effect. Formation of Micelles and Biological Membranes. John Wiley & Sons, New York.

4. Stein, W. D. (1967). The Movement of Molecules across Cell Membranes. Academic Press, New York.

5. Ansell, G. B., Hawthorne, J. N. and Dawson, R. M. C. (1973). Form and Function of Phospholipids, vol. 3. Elsevier, Amsterdam.

6. Fendler, J. H. (1982). Membrane Mimetic Chemistry. John Wiley & Sons, New York.

7. McElhaney, R. N. (1984). The Structure and Function of the Acholeplasma Laidlawii Plasma Membrane. Biochim. Biophys. Acta 779: 1-42.

8. Lee, A.G. (1975). The Functional Properties of Biological Membranes: A Physical-Chemical Approach. Prog. Biophys. Molec. Biol. 29: 3-56.

9. Chapman, D. (1975). Phase Transitions and Fluidity Characteristics of Lipids and Cell Membranes. Quarterly Reviews of Biophysics 8: 185-235.

10. McElhaney, R. N. (1984). The Relationship between Membrane Lipid Fluidity and Phase State and the Ability of Bacteria and Mycoplasmas to Grow and Survive at Various Temperatures, in Membrane Fluidity (Kates, M. and Manson, L. A., eds.). Plenum Publishing Corporation, New York.

11. Aloia, R. C. (1983). Membrane Fluidity in Biology, vols. 1 and 2. Academic Press, New York.

12. Colombetti, G. and Lenci, F. (1984). Membranes and Sensory Transduction. Plenum Press, New York.

13. Poste, G. and Nicolson, G. L. (1982). Membrane Reconstitution. Cell Surface Reviews, vol. 8. North-Holland Publishing Company, Amsterdam.

14. Kates, M. and Manson, L. A. (1984). Membrane Fluidity. Biomembranes, vol. 12. Plenum Press, New York.

15. McElhaney, R. N. (1982). Effects of Membrane Lipids on Transport and Enzymic Activities. Current Topics in Membranes and Transport 17: 317-380.

16. Van Deenen, L. L. M., Houtsmuller, U. M. T., De Haas, G. H. and Mulder, E. (1962). J. Pharm. Pharmacol. 14: 429-433.

17. Hirt, R. and Berchtold, R. (1958). Zur Synthese der Phosphatide. Eine neue Synthese der Lecithine. Pharmaceutica Acta Helvetiae 33: 349-357.

18. Browning, J. and Seelig, J. (1979). Synthesis of Specifically Deuterated Saturated and Unsaturated Phosphatidylserines. Chem. Phys. Lipids 24: 103-118.

19. Patel, K. M., Morrisett, J. D. and Sparrow, J. T. (1979). A Convenient Synthesis of Phosphatidylcholines: Acylation of sn-glycero-3-phosphocholine with Fatty Acid Anhydride and 4-Pyrrolidinopyridine. J. Lipid Res. 20: 674-677.

20. Robles, E. C. and Van Den Berg, D. (1969). Synthesis of Lecithins by Acylation of O-(sn-Glycero-3-phosphoryl)choline with Fatty Acid Anhydrides. Biochim. Biophys. Acta 187: 520-526.

21. Hermetter, A. and Paltauf, F. (1981). A Facile Procedure for the Synthesis of Saturated Phosphatidylcholines. Chem. Phys. Lipids 28: 111-115.

22. Hansen, W. J., Murari, R., Wedmid, Y. and Baumann, W. J. (1982). An Improved Procedure for the Synthesis of Choline Phospholipids via 2-Bromoethyl Dichlorophosphate. Lipids 17: 453-459.

23. Gupta, C., Radhakrishnan, R. and Khorana, H. G. (1977). Glycerophospholipid Synthesis: Improved General Method and New Analogs Containing Photoactivable Groups. Biochem. 74: 4315-4319.

24. Lammers, J. G., Liefkens, Th. J., Bus, J. and van der Meer, J. (1978). Synthesis and Spectroscopic Properties of α- and β-Phosphatidylcholines and Phosphatidylethanolamines. Chem. Phys. Lipids 22: 293-305.

25. Andrews, S. B., Faller, J. W., Barrnett, R. J. and Mizuhira, V. (1978). Organometallic Fatty Acid and Phospholipid Analogs. Synthesis and Incorporation and Detection in Model Membranes and Biomembranes. Biochim. Biophys. Acta 506: 1-17.

26. Radhakrishnan, R., Costello, C. E. and Khorana, H. G. (1982). Sites of Photolytic Intermolecular Cross-Linking between Fatty Acyl Chains in Phospholipids Carrying a Photoactivable Carbene Precursor. J. Am. Chem. Soc. 104: 3990-3997.

27. Endo, T., Inoue, K., Nojima, S., Terashima, S. and Oshima, T. (1982). Synthesis and Physical Properties of Phosphatidylcholines Containing ω-Cyclohexyl Fatty Acyl Chains. Chem. Phys. Lipids 31: 61-74.

28. Barton, P. G. and Gunstone, F. D. (1975). Hydrocarbon Chain Packing and Molecular Motion in Phospholipid Bilayers Formed from Unsaturated Lecithins. J. Biol. Chem. 250: 4470-4476.

29. Bonsen, P.P. M., Burbach-Westerhaus, G. J., de Haas, G. H. and Van Deenen, L. L. M. (1972). Chem. Phys. Lipids 3: 199-220.

30. Shinitzky, M. (1984). Physiology of Membrane Fluidity, vol. 1 and 2. CRC Press, Boca Raton.

31. Gulik-Krzywicki, T. (1975). Structural Studies of the Association between Biological Membrane Components. Biochim. Biophys. Acta 1: 1-28.

32. Reiss-Husson, F. (1967). Structure des Phase Liquide-cristalline de Differents Phospholipides, Monoglycérides, Sphingolipides, Anhydres ou en Présence d'Eau. J. Mol. Biol. 25: 363-382.

33. Charvolin, J. and Tardieu, A. (1978). Lyotropic Liquid Crystals: Structures and Molecular Motions. Solid State Physics, Supplement 14: 209-257.

34. Tardieu, A. and Luzzati, V. (1973). Structure and Polymorphism of the Hydrocarbon Chains of Lipids: A Study of Lecithin-Water Phases. J. Mol. Biol. 75: 711-733.

35. Chapman, D., Williams, R. M. and Ladbrooke, B. D. (1967). Physical Studies of Phospholipids. VI. Thermotropic and Lyotropic Mesomorphism of Some 1,2-Diacylphosphatidyl-cholines. Chem. Phys. Lipids 1: 445-475.

36. Clejan, S., Bittman, R., Deroo, P. W., Isaacson, Y. A. and Rosenthal, A. F. (1979). Biochem. 18: 2118-2125.

37. Chowdry, B. Z., Lipka, G., Hajdu, J. and Sturtevant, J. M. (1984). Phase Transition Properties of 1-Alkyl and 1-Acyl-2-amidophosphatidylcholines and Related Derivatives. Biochem. 23: 2044-2049.

38. Barton, P. G. and Gunstone, F. D. (1975). Hydrocarbon Chain Packing and Molecular Motion in Phospholipid Bilayers Formed from Unsaturated Lecithins. J. Biol. Chem. 250: 4470-4476.

39. Lalanne, J. R., Lemaire, B., Rouch, J., Vaucamps, C. and Proutiere, A. (1980). The Even-Odd Effect in Liquid Crystals: A Collective or Intrinsic Molecular Property. J. Chem. Phys. 73: 1927-1931.

40. Lewis, B. A. and Engelman, D. M. (1983). Lipid Bilayer Thickness Varies Linearly with Acyl Chain Length in Fluid Phosphataidylcholine Vesicles. J. Mol. Biol. **166**: 211-217.

41. Lipka, G., Chowdry, B. Z. and Sturtevant, J. M. (1984). A Comparison of the Phase Transition Properties of 1,2-Diacylphosphatidylcholines and 1,2-Diacylphosphatidyl-ethanolamines in H_2O and D_2O. J. Phys. Chem. **88**: 5401-5406.

42. Cornell, B. A. and Separovic, F. (1983). Membrane Thickness and Acyl Chain Length. Biochim. Biophys. Acta **733**: 189-193.

43. Browning, J. L. and Seelig, J. (1980). Bilayers of Phosphatidylserine: A Deuterium and Phosphorus Nuclear Magnetic Resonance Study. Biochem. 19: 1262-1270.

44. Casal, H. L. and Mantsch, H. H. (1983). The Thermotropic Phase Behavior of N-Methylated Dipalmitoylphosphatidylethanolamines. Biochim. Biophys. Acta **735**: 387-396.

45. Trifonov, A. Z. and Ivanova, M. G. (1980). On the Measurement of Water Penetration into Lipid Multilayers. J. Colloid Inter. Sci. 73: 298-299.

46. Parsegian, V. A. (1983). Dimensions of the "Intermediate" Phase of Dipalmitoylphosphatidylcholine. Biophys. J. **44**: 413-415.

47. Larsson, K. (1977). Folded Bilayers--An Alternative to the Rippled Lamellar Lecithin Structure. Chem. Phys. Lipids **20**: 225-228.

48. Rand, R. P., Chapman, D. and Larsson, K. (1975). Tilted Hydrocarbon Chain of Dipalmitoyl Lecithin Become Perpendicular to the Bilayer before Melting. Biophys. J. **15**: 1117-1124.

49. Silvius, J. R., Read, B. D. and McElhaney, R. N. (1979). Thermotropic Phase Transitions of Phosphatidylcholines with Odd-Numbered n-Acyl Chains. Biochim. Biophys. Acta 555: 175-178.

50. Janiak, M. J., Small, D. M. and Shipley, G. G. (1976). Nature of the Thermal Pretransition of Synthetic Phospholipids: Dymyristoyl- and Dipalmitoyllecithin. Biochemistry **15**: 4574-4580.

51. Worcester, D. L. (1975). Neutron Diffraction Studies of Biological Membranes and Membrane Components. Neutron Scattering for the Analysis of Biological Structures. Brookhaven Symposia in Biology 27: III-37 to III-57.

52. Fontell, K. (1981). Liquid Crystallinity in Lipid-Water Systems. Mol. Cryst. Liq. Cryst. 63: 59-82.

53. Büldt, G. and de Haas, G. H. (1982). Conformational Differences between sn-3-Phospholipids and sn-2-Phospholipids. A Neutron and X-Ray Diffraction Investigation. J. Mol. Biol. **158**: 55-71.

54. Chapman, D., Byrne, P. and Shipley, G. G. (1966). The Physical Properties of Phospholipids I. Solid State and Mesomorphic Properties of Some 2,3-Diacyl-DL-phosphatidylethanolamines. Proc. Roy. Soc. A290: 115-142.

55. Cameron, D. G. and Mantsch, H. H. (1982). Metastability and Polylmorphism in the Gel Phase of 1,2-Dipalmitoyl-3-sn-phosphatidylcholine. A Fourier Transform Infrared Study of the Subtransition. Biophys. J. 38: 175-184.55.

56. Lytz, R. K. (1978). X-Ray Structure Studies of Oriented Phospholipid Multilayers. Ph.D. Thesis. Oregon State University, Corvallis, OR.

57. Borkowski, C. J. and Kopp, M. K. (1968). New Type of Position-Sensitive Detectors of Ionizing Radiation Using Risetime Measurement. The Review of Scientific Instruments 39: 1515-1522.

58. Veress, I. and Montvai, A. (1978). Survey on Multiwire Proportional Chambers. Nucl. Instr. Meth. 156: 73-80.

59. Borkowski, C. J. and Kopp, M. K. (1971). Some Applications and Properties of One- and Two-Dimensional Position-Sensitive Proportional Counters. I.E.E.E.

60. Hough, J. and Drever, R. W. P. (1972). Proportional Counters for the Localization of Ionising Radiation. Nucl. Instr. Meth. 103: 365-372.

61. Izumi, T., Kurihama, T. and Nitta, J. (1984). A New Diffractometer Using a Curved Position-Sensitive Detector and Its Applications to X-Ray Crystallography. J. Appl. Cryst. 17: 470-475.

62. Hendrix, J. (1985). Position Sensitive X-Ray Detectors. Adv. Polym. Sci.67: 59-98.

63. Yoshioka, Y., Hasegawa, K.-i. and Mochiki, K.-i. (1982). Study on X-Ray Stress Analysis Using a New Position-Sensitive Proportional Counter.

64. Gabriel, A. and Dupont, Y. (1972). A Position Sensitive Proportional Detector for X-Ray Crystallography. Rev. Sci. Instr. 43: 1600-1602.

65. Franchy, R. and Ibach, H. (1985). CO on W(100) at 100 K Studied by a High Resolution EELS Spectrometer with Multi-Channel Detector. Surface Science 155: 15-23.

66. Arndt, U. W. (1986). X-ray Position Sensitive Detectors. J. Appl. Cryst. 19: 145-163.

67. Nuffield, E. W. (1966). X-Ray Diffraction Methods. John Wiley & Sons, Inc. New York.

68. Taylor, J. and Parrish, W. (1955). Absorption and Counting-Efficiency Data for X-Ray Detectors. Rev. Sci. Instr. **26**: 367-373.

69. Powder Diffraction File, Sets 27 - 28. (1986). International Center for Diffraction Data. Swarthmore, PA.

70. Larrson, K. and von Sydow, E. (1966). The Crystal Structure of the B-Form of Fatty Acids. Acta Chem. Scand. **20**: 1203-1207.

71. Malta, V., Celotti, G., Zannetti, R., and Martelli, A. F. (1971). Crystal Structure of the C Form of Stearic Acid. J. Chem. Soc. (B): 548-553.

72. Sherwood, D. (1976). Crystals, X-Rays and Proteins. John Wiley & Sons, New York.

73. Azaroff, L. V. (1968). Elements of X-Ray Crystallography. McGraw-Hill, New York.

74. Kakudo, M., Kasai, N. (1972). X-Ray Diffraction by Polymers. Kodansha Ltd., Tokyo, and Elsevier Publishing Company, Amsterdam and New York.

75. Guinier, A. (1963). X-Ray Diffraction in Crystals, Imperfect Crystals and Amorphous Bodies. (Trans. P. Lorrain and D. S.-M. Lorrain). W. H. Freeman and Company, San Francisco.

76. Hukins, D. W. L. (1981). X-Ray Diffraction by Ordered and Disordered Systems. Pergamon Press, Oxford.

77. Franks, N. P., Lieb, Y. K. (1981). Low-Angle X-Ray Diffraction in Membrane Spectroscopy (ed. E. Grell), pp 437-487. Springer-Verlag, Berlin.

78. Albon, N. (1985). Transitions and Molecular Packing in Highly Purified 1,2-Dipalmitoylphosphatidylcholine-Water Phases. 3. Structures of Phases with High Water Content. J. Phys. Chem. **89**: 3147-3151.

79. Hui, S. W. (1976). The Tilting of the Hydrocarbon Chains in a Single Bilayer of Phospholipid. Chem. Phys. Lipids **16**: 9-18.

80. Stamatoff, J. B., Graddick, W. F., Powers, L., Moncton, D. E. (1979). Direct Observation of the Hydrocarbon Chain Tilt Angle in Phospholipid Bilayers. Biophys. J. **25**: 253-261.

81. Wilkinson, D. A., McIntosh, T. J. (1986). A Subtransition in a Phospholipid with a Net Charge, Dipalmitoylphosphatidylglycerol. Biochem. **25**: 295-298.

82. Ruocco, M. J. and Shipley, G. G. (1982). Characterization of the Sub-Transition of Hydrated Dipalmitoylphosphatidylcholine Bilayers. X-Ray Diffraction Study. Biochim. Biophys. Acta **684**:

59-66.

83. Ruocco, M. J. and Shipley, G. G. (1982). Characterization of Hydrated Dipalmitoylphosphatidylcholine Bilayers. Kinetic, Hydration and Structural Study. Biochim. Biophys. Acta **691**: 309-320.

84. Chen, S. C., Sturtevant, J. M. and Gaffney, B. J. (1980). Scanning Calorimetric Evidence for a Third Phase Transition in Phosphatidylcholine Bilayers. Proc. Natl. Acad. Sci. USA **77**: 5060-5063.

85. Füldner, H. H. (1981). Characterization of a Third Phase Transition in Multilamellar Dipalmitoyllecithin Liposomes. Biochemistry **20**: 5707-5710.

86. Stümpel, J., Eibl, H. and Nicksch, A. (1983). X-Ray Analysis and Calorimetry on Phosphatidylcholine Model Membranes. Biochim. Biophys. Acta **727**: 246-254.

87. Nagle, J. F., Wilkinson, D. A. (1978). Lecithin Bilayers. Density Measurements and Molecular Interactions. Biophys. J. **23**: 159-175.

88. Nagle, J. F., Wilkinson, D. A. (1982). Dilatometric Studies of the Subtransition in Dipalmitoylphosphatidylcholine. Biochem. **21**: 3817-3821.

89. Church, S. E., Griffiths, D. J., Lewis, R. N. H. A., McElhaney, R. N., Wickman, H. H. (1986). X-Ray Structure Studies of Thermotropic Phases in Isoacylphosphatidylcholine Multibilayers. Biophys. J. **49**: 597-605.

90. Büldt, G., Gally, H. U., Seelig, A., Seelig, J. (1978). Neutron Diffraction Studies on Selectively Deuterated Phospholiid Bilayers. Nature **271**: 182-184.

91. Hitchcock, P. B., Mason, R., Thomas, K. M., Shipley, G. G. (1974). Structural Chemistry of 1,2 Dilauroyl-DL-phosphatidylethanolamine: Molecular Conformation and Intermolecular Packing of Phospholipids. Proc. Nat. Acad. Sci. USA 71: 3036-3040.

92. Casal, H. L., Mantsch, H. H., Cameron, D. G., Gaber, B. P. (1984). On the Subtransitions of Deuterated Derivatives of 1,2-Dipalmitoyl-sn-glycero-3-phosphocholine. Chem. Phys. Lipids **33**: 109-112.

93. Finegold, L., Singer, M. A. (1984). Phosphatidylcholine Bilayers: Subtransitions in Pure and in Mixed Lipids. Chem. Phys. Lipids **35**: 291-297.

94. Büldt, G., Wohlgemuth, R. (1981). The Headgroup Conformation of Phospholipids in Membranes. J. Membrane Biol. 58: 81-100.

95. Janiak, M. J., Small, D. M., Shipley, G. G. (1979). Temperature and Compositional Dependence of the Structure of Hydrated Dimyristoyl Lecithin. J. Biol. Chem. 254: 6068-6078.

96. Inoko, Y., Mitsui, T. (1978). Structural Parameters of Dipalmitoyl Phosphatidylcholine Lamellar Phases and Bilayer Phase Transitions. J. Phys. Soc. Jpn. 44: 1918-1924.

97. Stamatoff et al. Biophys. J. 1981.

98. Alecio, M. R., Miller, A., Watts, A. (1985). Diffraction of X-Rays by Rippled Phosphatidylcholine Bilayers. Biochim. Biophys. Acta 815: 139-142.

99. Stamatoff, J., Feuer, B., Guggenheim, H. J., Tellez, G., Yamane, T. (1982). Amplitude of Rippling in the P_{β} Phase of Dipalmitoylphosphatidylcholine Bilayers. Biophys. J. 38: 217-226.

100. Gaber, B. P., Yager, P., Peticolas, W. L. (1978). Interpretation of Biomembrane Structure by Raman Difference Spectroscopy. Nature of the Endothermic Transitions in Phosphatidylcholines. Biophys. J. 21: 161-176.

101. Brady, G. W., Fein, D. B. (1977). An Analysis of the X-Ray Interchain Peak Profiles in Dipalmitoylglycerophosphocholine. Biochim. Biophys. Acta 464: 249-259.

102. Parsegian, V. A. (1983). Dimensions of the "Intermediate" Phase of Dipalmitoylphosphatidylcholine. Biophys J. 44: 413-415.

103. Lvov, J. M., Mogilevskij, L. J., Fejgin, L. A., Györgyi, S., Ronto, Gy., Thompson, K. K., Sugár, I. P. (1986). Structural Parameters of Phosphatidylcholine Bilayer Membranes. Mol. Cryst. Liq. Cryst. 133: 65-73.

104. Gottlieb, M. H., Eanes, E. D. (1974). Coexistence of Rigid Crystalline Phases in Lecithin-Water Mixtures. Biophys. J. 14: 335-341.

105. Gally, H.-U., Niederberger, W., Seelig, J. (1975). Conformation and Motion of the Choline Head Group in Bilayers of Dipalmitoyl-3-sn-phosphatidylcholine. Biochem. 14: 3647-3652.

106. Nagle, J. F., Wiener, M. C. (19xx). Structure of Fully Hydrated Bilayer Dispersions, unpublished.

107. Lytz, R. K., Reinert, J. C., Church, S. E. and Wickman, H. H. (1984). Structural Properties of a Monobrominated Analog of 1,2-Dipalmitoyl-sn-glycero-3-phosphorylcholine. Chem. Phys. Lipids 35: 63-76.

108. Mantsch, H. H., Madec, C., Lewis, R. N. A. H. and McElhaney, R. N. (1985). Thermotropic Phase Behavior of Model Membranes Composed of Phosphatidylcholines Containing Iso-Branched Fatty Acids. 2. Infrared and ^{31}P NMR Spectroscopic Studies. Biochem. **24**: 2440-2446.

109. Rilfors, L. (1985). Difference in Packing Properties between Iso and Anteiso Methyl-Branched Fatty Acids as Revealed by Incorporation into the Membrane Lipids of Acholeplasma Laidlawaii Strain A. Biochim. Biophys. Acta **813**: 151-160.

110. Sturtevant, J. M., Ho, C., Reimann, A. (1979). Thermotropic Behavior of Some Fluorodimyristoylphosphatidylcholines. Proc. Natl. Acad. Sci. USA **76**: 2239-2243.

111. Lewis, R. N. A. H. and McElhaney, R. N. (1985). Thermotropic Phase Behavior of Model Membranes Composed of Phosphatidylcholines Containing Iso-Branched Fatty Acids. 1. Differential Scanning Calorimetric Studies. Biochem. **24**: 2431-2439.

112. Darland, G. and Brock, T. D. (1971). J. Gen. Microbiol. **67**: 9-15.

113. Christie, W. W. (1969). in Topics in Lipid Chemistry, vol 1. (Gunstone, F. D.). p.1.

114. Kaneda, T. (1977). Fatty Acids of the Genus Bacillus: an Example of Branched-Chain Preference. Bateriol. Reviews **41**: 391-418.

115. De Rosa, M., De Rosa, S., Gambacorta, A., Minale, L. and Bu'lock, J. D. (1977). Phytochem. **16**: 1961-1965.

116. Barton, A. F. M. (1983). CRC Handbook of Solubility Parameters and Other Cohesion Parameters. CRC Press, Boca Raton.

117. Morrison, R. T., Boyd, R. N. (1976). Organic Chemistry. Allyn and Bacon, Inc., Boston.

118. Abrahamsson, S. (1959). Solid State Behavior of Long Branched-Chain Fatty Acids. Arkiv fÖr Kemi **14**: 65-83.

119. Yang, C. P., Wiener, M. C., Lewis, R. N. A. H., McElhaney, R. N., Nagle, J. F. (1986). Dilatometric Studies of Isobranched Phosphatidylcholines. Biochhim. Biophys. Acta **863**: 33-44.

120. Wickman, H. H. unpublished results.

121. Duncum, B. M. (1947). The Development of Inhalation Anaesthesia with Special Reference to the Years 1846-1900. Oxford University Press, New York.

122. Vickers, M. D., Wood-Smith, F. G., and Stewart, H. C. (1979). Drugs in Anaesthetic Practice. Butterworths, Boston.

123. Rook, J. J. (1974). Formation of Haloforms during Chlorination of Natural Waters. Water Treat. Exam. 23: 234-243.

124. Bellar, T. A., Lichtenberg, J. J. and Kroner, R. C. (1974). The Occurrence of Organohalides in Chlorinated Drinking Water. J. Am. Water Works Assoc. **66**: 703-706.

125. Bunn, W. W., Haas, B. B., Deane, E. R., and Kleopfer, R. C. (1975). Formation of Trihalomethanes by Chlorination of Surface Water. Env. Letters **10**: 205-213.

126. Cantor, K. P. and McCabe, L.J. (1978). The Epidemiologic Approach to the Evaluation of Chemicals in Drinking Water. Proceedings of the Annual American Water Works Conference, Atlantic City, New Jersey.

127. Lunde, G. J. (1972). J. Am. Oil Chem. Soc. **49**: 44-48.

128. Machulla, H.-J., Stöcklin, G., Kupfernagel, Ch., Freundlieb, Ch., Höck, A. Vyska, K. and Feinendegen, L. E. (1978). Comparative Evaluation of Fatty Acids Labeled with C-11, Cl-34m, Br-77, and I-123 for Metabolic Studies of the Myocardium: Concise Communication. J. Nucl. Med. **19**: 298-302.

129. Hill, M. (1974). The Effect of Anaesthetic-Like Molecules on the Phase Transition in Smectic Mesophases of Dipalmitoyllecithin. I. The Normal Alcohols to C = 9 and Three Inhalation Anaesthetics. Biochim. Biophys. Acta **356**: 117-124.

130. Kamaya, H., Kaneshina, S., Ueda, I. (1981). Partition Equilibrium of Inhalation Anesthetics and Alcohols between Water and Membranes of Phospholipids with Varying Acyl Chain-Lengths. Biochim. Biophys. Acta **646**: 135-142.

131. Simon, S. A., McDaniel, R. V., McIntosh, T. J. (1982). Interaction of Benzene with Micelles and Bilayers. J. Phys. Chem. **86**: 1449-1456.

132. Inoue, T., Kamaya, H., Ueda, I. (1985). Stopped-Flow Study of Anesthetic Effect on Water-Transport Kinetics through Phospholipid Membranes. Interfacial versus Lipid Core Ligands. Biochim. Biophys. Acta **812**: 393-401.

133. Leo, A. (1983) in Handbook of Environmental Data on Organic Chemicals. Van Nostrand Reinhold Company, New York.

134. Verschueren, K. (1983). Handbook of Environmental Data on Organic Chemicals. Van Nostrand Reinhold Company, New York.

135. King, G. I., Jacobs, R. E., White, S. H. (1985). Hexane Dissolved in Dioleollecithin Bilayers Has a Partial Molar Volume of Approximately Zero. Biochem. **24**: 4637-4645.

136. Kita, Y., Bennett, L. J., Miller, K. W. (1981). The Partial Molar Volumes of Anesthetics in Lipid Bilayers. Biochim. Biophys. Acta 647: 130-139.

137. McDaniel, R. V., Simon, S. A., McIntosh, T. J., Borobyagin, V. (1982). Interaction of Benzene with Bilayers. Thermal and Structural Studies. Biochem. 21: 4116-4126.

138. Simon, S. A., Stone, W. L., Bennett, P. B. (1979). Can Regular Solution Theory Be Applied to Lipid Bilayers? Biochim. Biophys. Acta 550: 38-47.

139. Katz, Y. (1986). Physical Characteristics of Membranes from Solubility Measurements of Noble Gases. J. Phys. Chem. 90: 190-195.